ABSTRACT

Title of Document: MORPHOLOGIC INSTABILITY OF GRAPHENE AND ITS POTENTIAL APPLICATIONS

Zhao Zhang, Doctor of Philosophy, 2011

Directed By: Assistant Professor Teng Li, Department of Mechanical Engineering

Graphene is a monolayer of graphite. The surge of interest in graphene, as epitomized by the Nobel Prize in Physics in 2010, is largely attributed to its exceptional properties. Ultra thin, mechanically tough, electrically conductive, and transparent graphene films promise to enable a wealth of possible applications ranging from thin-film solar cells, flexible displays, to biochemical sensing arrays. However, significant gaps remain to realize these potential applications, largely due to the difficulty of precisely controlling graphene properties. Graphene is intrinsically non-flat and tends to be randomly corrugated. The random graphene morphology can lead to unstable performance of graphene devices as the corrugating physics of graphene is closely tied to its electronic properties. Future success of graphene-based applications hinges upon precise control of the graphene morphology, a significant challenge largely unexplored so far. This dissertation aims to explore viable pathways to tailoring

graphene morphology and leverage possible morphologic instability of graphene for novel nano-device applications.

Inspired by recent experiments, we propose and benchmark a strategy to precisely control the graphene morphology via extrinsic regulation (e.g., substrate surface features, patterned nanowires and nanoparticles). A general energetic framework is delineated to quantitatively determine the extrinsically regulated graphene morphology through energy minimization. Such a framework is benchmarked by determining the graphene morphology regulated by various types and dimensions of nanoscale extrinsic scafffolds, including two dimensional herringbone and checkerboard corrugations on substrate surfaces and one dimensional substrate surface grooves and patterned nanowires. The results reveal a snap-through instability of the graphene morphology, that is, depending on interfacial bonding energy and substrate surface roughness, the graphene morphology exhibits a sharp transition between two distinct states: (1) closely conforming to the substrate surface and (2) remaining nearly flat on the substrate surface. This snap-through instability of graphene holds potential to enable graphene-based functional nano-devices (e.g., ultrasensitive nano-switches).

Another type of morphologic instability of graphene is the spontaneous scrolling of graphene into a carbon nanoscroll (CNS). The spiral multilayer nanostructure of CNSs is topologically open and thus distinct from that of carbon nanotubes (CNTs). The unique topological structure of CNSs can enable an array of novel applications, e.g., hydrogen storage, water channels and ultrafast nano-oscillators. However, the realization of CNS-based applications is hindered by the lack of reliable approach to

fabricating high quality CNSs. We propose a simple physical approach to fabricating CNSs via CNT-initiated scrolling of graphene on a substrate. The successful formation of a CNS depends on the CNT diameter, the carbon–carbon interaction strength and the graphene-substrate interaction strength. We further demonstrate that the resulting CNS/CNT nanostructure can be used as an ultrafast axial nano-oscillator that operates at 10s GHz. Such CNS-based nano-oscillators can be excited and driven by an external AC electric field, further illustrating their potential to enable nano-scale energy transduction, harnessing and storage.

MORPHOLOGIC INSTABILITY OF GRAPHENE AND ITS POTENTIAL APPLICATIONS

By

Zhao Zhang

Dissertation submitted to the Faculty of the Graduate School of the
University of Maryland, College Park, in partial fulfillment
of the requirements for the degree of
Doctor of Philosophy
2011

Advisory Committee:
Assistant Professor Teng Li, Chair
Professor Hugh Bruck
Professor Abhijit Dasgupta
Professor Gottlieb Oehrlein, Dean's Representative
Assistant Professor Santiago Solares

Dedicated to my parents.

Acknowledgements

I would first like to express my sincere thanks to my advisor, Prof. Teng Li. My dissertation could not have been made possible without his support, guidance and encouragement. I have learned so much from him over last four years, which has not been limited to conducting this research. His knowledge in mechanics and materials broadened my vision far beyond this dissertation; his inspiration constantly enlightened me to explore new interesting problems; his enthusiasm for research motivated me to decide to pursue my future career in academia. It is lucky for me to have Prof. Teng Li as my Ph.D. advisor and I expect to benefit from him for my whole career.

I am also indebted to all my dissertation committee members, Prof. Aris Christou, Prof. Abhijit Dasgupta, Prof. Gottlieb Oehrlein, Prof. Hugh Bruck and Prof. Santiago Solares. Their insightful suggestions and comments are invaluable for me to complete and improve this dissertation. I would like to thank Prof. Dasgupta for writing the recommendation letter for me to the Future Faculty Program. I also want to express my gratitude to Prof. Balachandran and Prof. Bruck for their support in my application for the *Michael J. Pelczar Award* and the *Dean's Doctoral Research Award*. I am appreciative of Prof. Solares who is always willing to share his professional experience and opinions of academia with me.

I am thankful to all the professors whose courses I took during the past four years. Especially, I would like to acknowledge Prof. Jeffery Klauda for the course

Molecular Modeling Methods which helped me step into this field and publish my first molecular dynamics paper.

I owe great thanks to Prof. Sulin Zhang and Xu Huang at Penn State University for their unreserved help in my learning molecular mechanics code. I am grateful to my group members Zheng Jia, Shuze Zhu, Andy Fox, and so on, for the discussion on numerous research problems and the wonderful time we have shared in and out the office. I also sincerely thank all my friends, whose encouragement and help were always there when I was in need.

My deepest gratitude and love go to my parents for all they have given to me.

Table of Contents

List of Tables

List of Figures

Chapter 1: Introduction and Background

Graphene is a monolayer of carbon atoms densely packed into a honeycomb lattice. As a two-dimensional (2D) crystal of carbon, graphene can be wrapped up into fullerenes (0D), rolled into nanotubes (1D) or stacked into graphite (3D) (Figure 1.1) [1]. Therefore, it can be regarded as the fundamental building block of all other members in the carbon family.

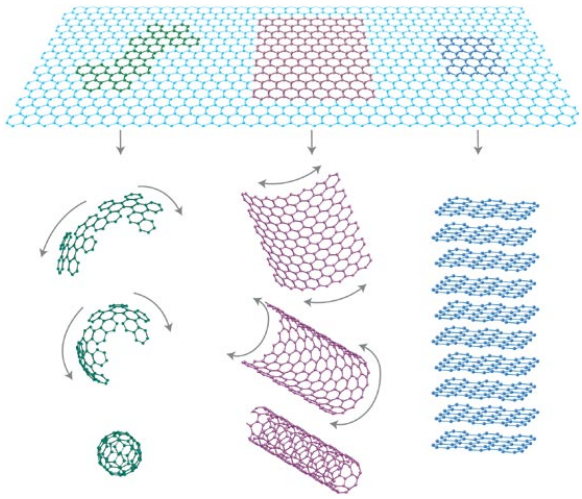

Figure 1.1. Graphene is the building block of all the carbon allotropes [1].

Perfect two-dimensional crystals were once presumed not to be thermodynamically stable. The argument is that when the thin film becomes only a few atomic layers thick, thermal fluctuations will destroy the long-range order of atoms, resulting in melting of the thin film at any finite temperature [2]. Although the word “graphene” has been invented to call one-layer atomic thick carbon atoms for a long time, it has been long believed that graphene could not exist in the free state because it would melt or form soot, fullerenes and nanotubes under ambient conditions [1]. The atomic monolayer was known only as an integral part of larger 3D structures.

This common misconception was clarified in 2004 by the isolated graphene flake first observed in experiment [3]. Via mechanical exfoliation, scientists at the University of Manchester obtained planar graphene on silicon substrate by using scotch tape to repeatedly peel off thin layers from bulk high-quality graphite. Since graphite is just many graphene sheets stacked together by weak van der Waals force, the mechanical exfoliation can easily break the bonds between graphene layers and leave graphite flakes with different thickness on the tape. These flakes were then transferred on to a silicon substrate covered by a thin layer of silicon dioxide on which single-layer or few-layer graphene can be identified by an optical microscope. The further measurements show that the single-layer graphene sheets are continuous and exhibit high crystal quality. Later on, the existence of graphene was confirmed by other groups [4] and free-standing graphene was also successfully fabricated [2]. The discovery of graphene in 2004 sparked great research interests in graphene and opened up a new era in materials science, physics and engineering, which is epitomized by the 2010 Nobel Prize in Physics to Professors Andre Geim and Konstantin Novoselov from the University of Manchester “for groundbreaking experiments regarding the two-dimensional material graphene”[5].

Although the mechanical exploration is the most straightforward method to fabricate graphene, it suffers from the limited graphene size and low output. Therefore, graphene once was the most expensive material in the world [6]. To achieve massive production of graphene, various fabrication techniques of graphene have been developed, such as chemical vapor deposition on various metal substrate [7-10], graphite oxide reduction [11] and epitaxial growth on silicon carbide substrate [12].

Now it becomes possible to fabricate graphene with the size up to several square feet. The large scale and massive production of graphene further enable its potential application in future electronic devices [9, 13].

1.1. Electronic and Mechanical Properties of Graphene

Graphene has attracted much research interests because of its extraordinary electronic and mechanical properties. Some properties of graphene result from its hexagonal crystal lattice, which are shared with carbon nanotubes, while many of them are attributed to the unique nature of graphene's 2D planar structure.

Band structure

Intrinsic graphene is a semi-metal or zero-gap semiconductor[3]. But the band structure of graphene is highly tunable. For example, the band gap of graphene nanoribbons is dependent on the chirality and width of the ribbons. Experiments have demonstrated that 200 meV energy gap can be achieved by narrowing graphene nanoribbons to a width of 15 nm [14]. In bilayer graphene, the band gap up to 250 meV can be continuously tunable by the voltage of the two gates [15]. First-principle calculations predicted a band-gap opening of ~300 meV for graphene under 1% uniaxial tensile strain [16].

Dirac fermions

Due to graphene's honey comb crystal lattice, the linear dispersion relation for electrons and holes close to the Fermi level leads to zero effective mass for electrons and holes [1]. They behave like relativistic particles which should be described by the

Dirac equation but not Schrödinger equation. Hence, the electrons and holes are called Dirac fermions [17]. These charge carriers in graphene mimic relativistic particles with zero rest mass and have an effective “speed of light”.

Electronic mobility

Graphene has remarkably high electron mobility at room temperature, with reported values in excess of 15,000 $cm^2V^{-1}s^{-1}$, 100 times larger than silicon [18].

Electronic conductivity

Graphene is the lowest resistivity substance known at room temperature. Its corresponding resistivity is 10^{-6} Ω·cm, less than that of silver [19].

Quantum Hall Effect

The quantum Hall Effect is that the Hall conductivity is an integer multiples of a basic quantity. This effect in graphene can be experimentally measured at room temperature [4]. However, in graphene the observed quantization condition is described by half-integer rather than integer values.

Transparency

Graphene only absorbs 2.3 % of white light and thus is almost transparent unless on substrates consisting of a silicon wafer with a 300 nm thick silicon dioxide layer [20, 21]. This partially explains that people have been making graphene by drawing lines with pencils for more than one thousand years but were not aware of it until 2004.

Negative coefficient of thermal expansion

While most materials expand when the temperature increases, recent experiments show that graphene shrinks when heated up. The coefficient of thermal expansion (CTE) of graphene is ~ -7×10^{-6} K^{-1} at 300K according to the experiment measurement [22].

Mechanical properties

Graphene is the strongest materials ever measured. Graphene has the young's modulus of ~1 TPa and the strength of 130 GPa, which is 200 times larger than that of steel [23]. Graphene is also very ductile. The fracture strain of graphene measured in experiments is up to 25% [23], and atomic simulations show that the nominal strain to fracture graphene is considerably lower for the uniaxial loading along armchair direction than along zigzag direction [24].

1.2. Potential Applications of Graphene

The extraordinary electronic and mechanical properties of graphene have inspired an array of tantalizing potential applications. Most applications are based on the following fundamental graphene electronic components:

Integrated circuit interconnects

Due to their high electrical and thermal conductivity, as well as low noise, metallic graphene nanoribbons (GNRs) are attractive candidates to replace copper for the next generation of integrated circuit interconnects [25]. Nowadays, the enhancement of integrated circuit performance mainly results from narrowing the width of copper nanowires. The resistivity of these nanowires, however, will increase as the width of

nanowires decreases and finally will stop the performance increase in the near future when the feature sizes drop to approximately 20 nanometers. As for metallic GNRs, even the width is down to several nanometers, it is still predicted to be good conductor. Recent experiments have already shown that conductivity performance of 20 nanometer wide GNRs is comparable to that of even the most optimistic projections for copper interconnects at that scale [25].

Field-effect transistors

The resistivity of graphene is a function of the perpendicular external electric field, i.e. gate voltage [3]. In addition, the electronic properties of GNRs can be controlled by their width and directionality, which makes it possible to built GNRs-based Field Effect Transistors (GNR-FETs) [14, 26, 27]. Because all the carbon atoms of graphene are on the perfect lattice points, it is easier to form smooth interfaces between GNRs with different width and directionality without introducing extra resistance at the junctions [28, 29]. In 2008, a research group successfully fabricated the smallest transistor so far, one atom thick, 10 atoms wide [30]. Graphene based nano electrical devices, i.e. GNR-FETs and GNR interconnects, could potentially overcome the bottleneck of the performance increase of current integrated circuits. For example, the electronic properties of silicon become unstable when its feature size is below 10 nm, which poses significant challenge to the ever-miniaturizing functional components in electronic devices. By contrast, graphene is stable down to a single benzene ring, which makes it a potential candidate material to replace silicon in future electronic technology.

Transparent and flexible conducting electrodes

Because graphene is conductive and transparent, it is a perfect candidate for transparent conducting electrodes in touch-screens [13], liquid crystal displays [31], organic photovoltaic cells [32, 33], and organic light-emitting diodes [34]. Compared with indium tin oxide (ITO), a wildly used material for current transparent conducting electrodes, graphene is much stronger and more ductile [23]. Thus graphene electrodes hold great potentials to be used in flexible and invisible electronics.

Other potential applications of graphene include nano-composite materials [35], biochemical sensor arrays [36], supercapacitors [37] and hydrogen storage [38]. Because of the short period of time after graphene's discovery, many exciting potential applications are still being explored.

1.3. Morphology of Graphene

1.3.1. Intrinsic morphology of graphene

Apparently, the existence of free-standing graphene contradicts the theoretical prediction that perfect two-dimensional crystals cannot exist in the free state due to its thermal instability. This contradiction can be explained by later studies on intrinsic morphology of graphene. Both experiments and simulations show that the free-standing graphene is not perfectly flat but has intrinsic ripples [2, 39], as shown in Figure 1.2. The surface normal of graphene sheet varies by several degrees and the out-of-plane deformations are about 1 nm. Simulations show that the average feature size of ripples is around 80 Å (Figure 1.2) [39], while experimental measurements

indicate that the feature size is 50–100 Å [2]. The corrugations are proved to be intrinsic because it is these ripples that make the 2D crystal lattice stable. Meanwhile, the 3D surface features in graphene are responsible for the electrical behaviors of graphene [22]. Given the existence of out-of-plane ripples, it becomes debatable that if graphene is truly a 2D structure. But graphene is still widely considered as 2D crystal since the amplitude of the ripples is much smaller than the graphene size.

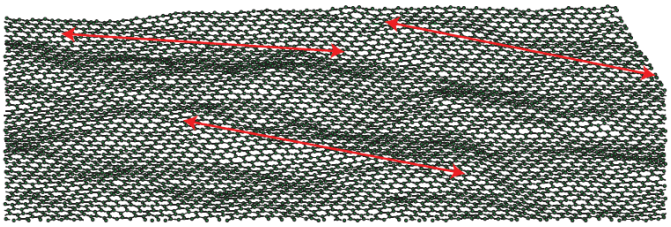

Figure 1.2. The intrinsic ripples in graphene. The red arrows represent the feature size of ripples, which is ~80 Å long [39].

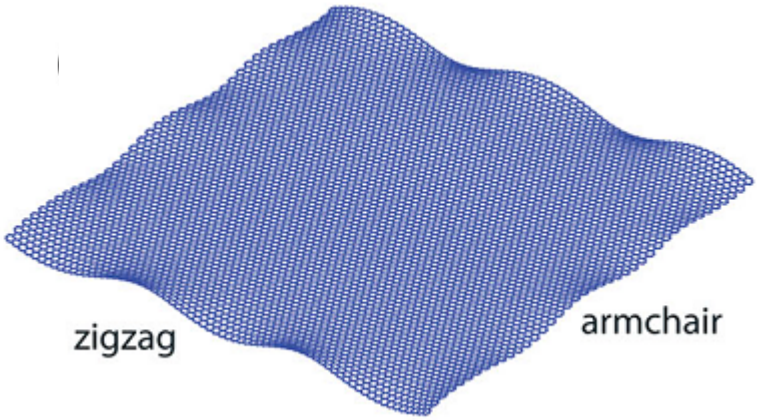

Figure 1.3. A warped graphene sheet obtained by relaxing edge stresses in atomic simulation [40].

The unsaturated carbon atoms along graphene edges lead to compressive edge stresses and high edge energy. Such compression stresses can buckle the graphene

locally and cause small wrinkles along the edges of graphene sheets. Both of the atomic simulation and finite element analysis were carried out to predict the shape of the edge wrinkles (Figure 1.3) [40, 41]. It is demonstrated that while the edge stress induced wrinkles are mainly localized at the boundaries of large size graphene sheets, such wrinkles can lead to twisting and scrolling of graphene nanoribbons [42].

1.3.2. Extrinsic morphology of graphene

Recent studies reveal that, the *extrinsic* morphology of graphene on substrate surfaces or nanoscale scaffolds is *regulated*, distinct from the *random intrinsic* morphology of freestanding graphene. Several types of extrinsic morphology of graphene have been reported, which are briefly summarized in the following.

1. Corrugations in graphene induced by rough substrate surfaces

When fabricated on a substrate (e.g., SiO_2) via mechanical exfoliation or transfer printing, graphene also corrugates, which is often attributed to graphene's intrinsic corrugations. However, recent experiments revealed that such random corrugations could be introduced by unwanted photoresist residue under the graphene if lithographic process is used [43]. After careful removal of the resist residue, atomic-resolution images of the graphene on SiO_2 showed that the graphene corrugations result from its partial conformation to the SiO_2 substrate. High-resolution scanning tunneling microscopy further indicated that the morphology of SiO_2-supported graphene closely matches that of the SiO_2 over the entire range of length scales with nearly 99% fidelity [44]. It has been further confirmed that graphene and few-layer graphene also partially follow the surface morphology of various substrates (e.g.,

GaAs, InGaAs and SiO_2) [45-48]. These experimental evidences strongly suggest that the regulated extrinsic corrugations in substrate-supported graphene are essentially distinct from the random intrinsic corrugations in freestanding graphene. Furthermore, the substrate regulation on graphene morphology has been shown to be strong enough to prevail over the intrinsic random corrugations in graphene. For example, on an atomically-flat mica substrate, the intrinsic corrugations in graphene can be smoothed, leading to an ultra-flat extrinsic morphology of the graphene [49].

2. Corrugations in graphene induced by crystal lattice mismatch

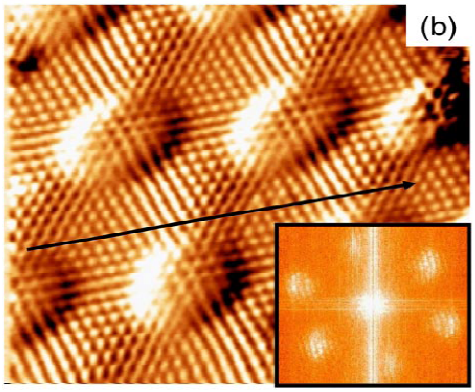

Figure 1.4. Epitaxial grown graphene on Ru(0001). The inset reproduces the Fourier transform of the image showing the (11×11) periodicity of the rippled graphene layer [50].

Graphene monolayers can be grown epitaxially on certain metal substrates (e.g., single-crystal ruthenium (0001)) under ultrahigh vacuum conditions [50]. Graphene covers the substrate surface completely over several microns and is periodically rippled. The periodical ripples come from the coincidence of difference lattice parameters of graphene and substrate: 11 carbon honeycombs (0.246 nm) adjust almost exactly with 10 Ru-Ru interatomic distances (0.27nm), as shown in Figure 1.4

[50]. This kind of periodicity is also observed in graphene on Pt(111), Ir(111) and Rh(111) [51, 52]. Therefore, this type of ripples in graphene can be controlled by selecting substrate materials with different lattice parameters.

3. Ripples in graphene induced by thermal mismatch

Graphene possesses negative coefficient of thermal expansion (CTE) which has been used to generate large scale ripples in graphene on polymer substrate. In the study of Reference [53], graphene was deposited on top of the polymer substrate with glass transition temperature of ~105 °C by mechanical exfoliation. The sample was annealed at 170 °C to allow polymer flow around to release stored strain energy. Then the sample was quickly cooled to room temperature. During the cooling, polymer contracted but graphene expanded. Therefore, graphene buckles with amplitude of nanometer scale.

The researches at UC Riverside reported the first directly control of ripple orientation, wavelength and amplitude in graphene sheets using thermal manipulation [22]. Single-layer and multi-layer graphene were suspended across pre-defined trenches on Si/SiO_2 substrates. Most graphene sheets were found to spontaneously form nearly periodic ripples whose crests are perpendicular to the edges of the trench. When graphene membranes were annealed up to 700 K, the ripples disappear due to the thermal mismatch. After cooling down, the ripples re-appeared and their morphology changed: amplitudes became larger and wavelength became longer. They proposed that annealing temperature and trench shape could be used to control the ripple texturing in graphene.

1.4. Introduction to Carbon Nanoscrolls

A carbon nanoscroll (CNS) is formed by rolling up a graphene sheet into a spiral multilayer structure (Figure 1.5) [54, 55]. It seems very similar to multiwall carbon nanotube (CNT), but they are distinctly different. The core size of a CNS can vary significantly by relative sliding between adjacent layers [56, 57]. In other words, a CNS is topologically open. By contrast, a multiwall CNT consists of several coaxial carbon cylinders and its core size can only be changed slightly by stretching the carbon-carbon (C-C) bonds. Therefore, a multiwall CNT is topologically closed.

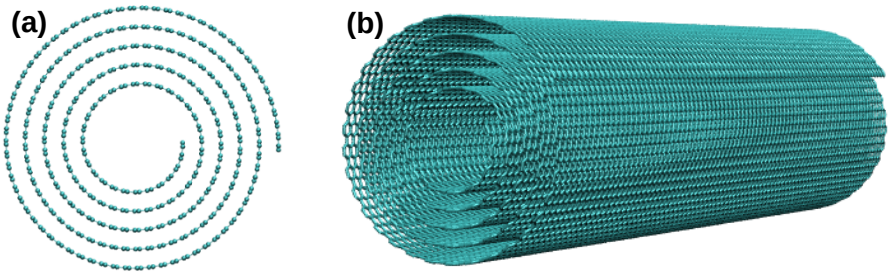

Figure 1.5. The structure of CNS. (a) End view; (b) Side view.

The open and highly tunable structure of CNSs, combining with the exceptional mechanical and electronic properties inherited from the basal graphene, has inspired potential applications of CNSs. For example, CNSs can be used as hydrogen storage medium [58, 59]. The high capacity for hydrogen storage in multiwall CNTs has already been demonstrated. But CNSs can rapid uptake and release of hydrogen because the exposed open edge of CNSs serves as a fast entry path for hydrogen molecules. Moreover, since CNSs can oscillate radially through the interlayer relative sliding, they could be used as nano-oscillators or nanoactuators in nano electrical-mechanical systems (NEMS) [60]. The radial oscillating frequency of CNSs is up to

gigahertz. Another application of CNSs is water and ion channels [61]. By controlling the inner diameter of CNSs, the flow rate of water through the core of CNSs can be adjusted over a broad range.

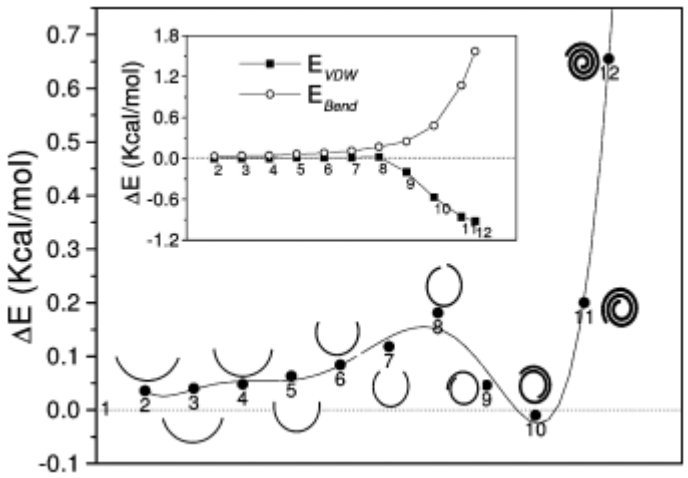

Figure 1.6. Change in total energy during the scrolling of graphene to make a CNS. The strain energy (E_{Bend}) and van der Waals energies (E_{vdW}) are shown in the inset graph [56].

The energetics of graphene scrolling into CNS and the stability of CNSs have been investigated previously [56]. Figure 1.6 plots the total energy variation during the scrolling of graphene. The total energy consists of two parts, strain energy and interaction energy (van der Waals energy). Before the formation of an overlap between two edges of graphene, the curling up of graphene leads to the increase of the strain energy (configuration 1-8 in Figure 1.6) but the interaction energy is always 0. So the total energy increases during the initial curling up process. Once a critical overlap is achieved, the interaction energy drives the further scrolling of graphene to decrease the total energy and thus the formation of CNS automatically occurs (configuration 8-10 in Figure 1.6). The resulting CNS may have lower energy than the planar graphene. In other words, the CNS is more stable.

Figure 1.6 implies that, in order to initiate the spontaneous scrolling of graphene, external energy assistance is required to overcome an energy barrier and then a critical overlap between graphene layers can be achieved. Experiments and simulations suggest that the energy assistance could come from sonication [55], fluctuation of isopropyl alcohol (IPA) solution [62] or water nanodroplets [63]. The experimental discovery of CNSs was achieved via a chemical approach, in which graphite is first intercalated using alkali metals, and the resulting exfoliated graphite sheets can curl into scrolls upon sonication [55]. Recent experiments show that a SiO_2-supported graphene monolayer immersed in isopropyl alcohol (IPA) solution can spontaneously roll up to form a CNS [62]. Molecular dynamics simulations show that a long and narrow freestanding carbon nanoribbon can spontaneously form a short CNS driven by low temperature (100 K) thermal fluctuation [64]. Recent simulations demonstrate that water nanodroplets could activate the folding of freestanding graphene to form different carbon nanostructures, including CNSs, depending on the size of both graphene and nanodroplets [63].

1.5. Motivation and Research Objectives

As mentioned above, graphene is intrinsically non-flat and tends to be corrugated due to the instability of two-dimensional crystals [39]. Since the corrugating morphology of atomically-thin graphene is strongly tied to its electronics properties [65, 66], the random intrinsic ripples and corrugations lead to unpredictable graphene properties, which are fatal for nanoelectronic devices for which precise (digital) control is the

key. Therefore, controlling the graphene morphology over large areas is crucial in enabling future graphene-based applications.

Recent studies reveal that, the *extrinsic* morphology of graphene on substrate surfaces or nanoscale scaffolds is *regulated*, distinct from the *random intrinsic* morphology of freestanding graphene [43, 45, 47, 48, 67]. These studies on the extrinsic morphology of graphene illuminate new pathways toward fine tuning the corrugating physics, and thus the properties of graphene via external regulation. So far, the available experimental evidence on the morphology of substrate-supported graphene is suggestive, but preliminary: the quantitative relationship between the graphene morphology and the substrate surface roughness has not been studied; the effect of graphene–substrate interaction on the graphene morphology remains elusive.

Motivated by the fertile and largely unexplored opportunities of extrinsic morphology of graphene, ***the first research objective of this doctoral dissertation is to explore an effective strategy to achieve precise extrinsic regulation of the graphene morphology beyond its intrinsic randomness***. Specific research objectives in this regard include:

- To investigate the graphene morphology regulated by patterned surfaces of rigid substrates;
- To investigate the graphene morphology regulated by low dimensional nanoscaffolds (e.g., patterned nanowires) at the graphene-substrate interface;
- To investigate the graphene morphology regulated by patterned surfaces of compliant substrates.

Particular focus will be placed on understanding the potential morphologic instability of the graphene under extrinsic regulation. At such an instability, the morphology of the graphene switches sharply between two distinct states, which can lead to significant change of the electronic properties of graphene and thus can be potentially leveraged to enable functional device components.

The spontaneous scrolling of graphene into a carbon nanoscroll (CNS) represents another type of morphologic instability of graphene of scientific and technological interests. The unique topology of CNSs leads to their distinct structural, dynamical and electronic properties [56, 57, 60, 62] and thus has inspired an array of exciting potential applications, such as hydrogen storage medium [58, 59], ultrafast oscillators and actuators [60], and water/ion channels [61]. Enthusiasm for CNS-based applications aside, there are still significant challenges to their realization, largely due to lack of mature approach to fabricating high quality CNSs. The existing fabrication methods are all chemical approaches, thus suffer from the possible contamination of chemical residue, and also the difficulty in controlling the rolling initiation and rolling direction [55, 62].

Aiming to address the abovementioned unsolved issues on CNSs, ***the second research objective of this doctoral dissertation is to explore a feasible physical approach to fabricating high quality CNSs and to investigate the potential application of the resulting CNS-based nanostructures as ultra-fast nano-oscillators.*** Specific research objectives include:

- To explore an all dry physical approach of CNT-initiated formation of CNS and to investigate the parameters that govern the CNS formation process;
- To investigate the ultra-fast oscillation behaviors of the CNS/CNT nanostructure and to explore possible mechanisms to enhance oscillation performance.

1.6. Dissertation Layout

To address the research objectives outlined above, the rest of the dissertation is organized as follows.

In Chapter 2, we delineate a theoretical framework to determine the substrate-regulated graphene morphology through energy minimization. We then apply such a framework to quantitatively study the graphene morphology on substrates with surface features (e.g. surface grooves, checkerboard or herringbone wrinkles). These substrate surface features can be fabricated via approaches combining lithography and strain engineering [68-71]. The results show that the morphology of graphene exhibits a snap-through instability in certain cases.

The size of abovementioned substrate surface features is on the order of ten nanometers, much larger than the C-C bond length in graphene. The significant progresses in fabricating nanowires with diameters of down to 1 nm patterned on substrate surface [72-74] offer new platforms to regulate graphene morphology with a resolution approaching the atomic feature size of graphene. In Chapter 3, to further explore the abundant opportunities of fine tuning graphene morphology via surface/interface regulation, we extend the energetic framework to study the graphene

morphology regulated by nanowires patterned on a substrate surface. The morphologic instability is also evident in the results, which is similar to that of graphene morphology regulated by the underlying substrate surface with engineered nanoscale patterns.

The abovementioned framework is mainly based on two assumptions. First, the substrate is assumed to be rigid and thus does not deform when interacting with the graphene. Second, only mono-layer graphene is considered. The two assumptions limit the general applicability of these models. To overcome the limitations of existing models, in Chapter 4 we explicitly determine the morphology of few-layer graphene regulated by the patterned surface of a compliant substrate. The effects of substrate stiffness, graphene-substrate adhesion and number of graphene layers on the regulated graphene morphology are revealed.

In Chapter 5, we demonstrate an all-dry physical approach to fabricating CNSs, in which the rolling of a substrate-supported graphene monolayer is initiated by a CNT. The resulting nanostructure is a CNT housed inside the CNS. It is shown that the successful formation of a CNS depends on the CNT diameter, the carbon–carbon interaction strength and the graphene-substrate interaction strength. To further explore the potential application of such resulting CNS/CNT nanostructure, we demonstrate a type of CNS-based nano-oscillators. We find that the CNT inside the CNS can oscillate along axial direction at a natural frequency of 10s GHz. We further demonstrate that the oscillation can be excited and driven by an external AC electric field, a feature that can potentially enable energy transduction, harnessing and storage at nanoscale.

In Chapter 6, the major findings and contributions of the dissertation are summarized and discussed, followed by an outlook of future work.

Chapter 2: Graphene Morphology Regulated by a Patterned Substrate Surface

In this Chapter, we thoroughly study the graphene morphology regulated by substrates with different surface features. Inspired by some experimental observations (Section 2.1), a general theoretical framework is delineated to determine the substrate-regulated graphene morphology (Section 2.2). Based on this framework, a computational model is developed to numerically solve the graphene morphology through energy minimization (Section 2.3). Such framework and numerical model are then applied to study the graphene morphology on a substrate with 1D periodic surface grooves (Section 2.4), 2D checkerboard or herringbone wrinkles (Section 2.5). Depending on the substrate surface roughness and the graphene-substrate interfacial bonding energy, the equilibrium morphology of graphene ranges from 1) closely conforming to the substrate, to 2) remaining flat on the substrate. Interestingly, in certain cases, the graphene morphology snaps between the above two limiting states. The snap-through instability can be explained by the double-well shape of the total energy profile. The simulation models and results are discussed in Section 2.6 and summarized in Section 2.7.

2.1. Experimental Observations

Free-standing graphene is intrinsically rippled due to the thermal fluctuation in 2D crystals [39]. Recent experiments show that after deposited or transfer printed onto a rough substrate surface, graphene will be corrugated by the interaction energy (e.g.,

van der Waals energy) between graphene and the underlying non-flat substrate surface [43, 45, 47, 48, 67, 75]. The corrugations in resulting graphene are extrinsic, rather than the intrinsic ripples in free standing graphene. Using scanning tunneling microscopy (STM), the morphology of single layer graphene on the SiO_2 surface was examined under ultrahigh vacuum conditions (Figure 2.1) [45]. The non-periodic fluctuation in graphene height was clearly observed and attributed to graphene film following (at least partially) the features of the underlying SiO_2 surface.

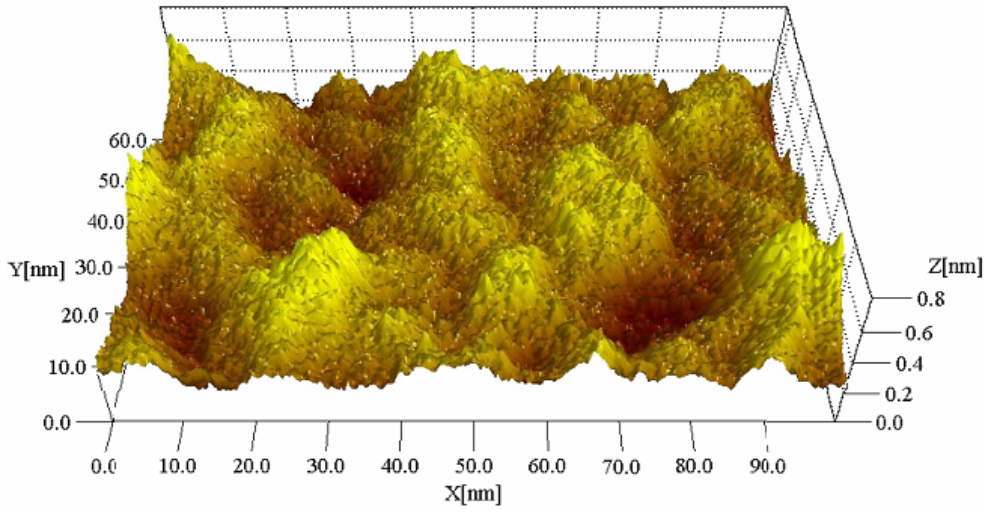

Figure 2.1. Stereographic plot of a large-scale (100×62 nm) STM image of a single-layer graphene film on the SiO_2 surface [45].

In another study, via a combined-SEM/AFM/STM technique, the atomic structure and nanoscale morphology of monolayer graphene sheets on SiO_2 substrate were examined [43]. The atomic-resolution images of the graphene in real space revealed that the graphene partially conforms to the underlying SiO_2 substrate. The histograms of the heights over graphene and SiO_2 indicated that the graphene surface is about 60% smoother than the SiO_2 surface.

The graphene morphology partially following the substrate surface corrugations was more clearly proven by the AFM studies on graphene and few-layer graphene supported by various semiconducting substrates [67]. It was found that graphene sheets strongly follow the texture of the sustaining substrates independent on doping, polarity, or roughness. Figure 2.2 shows the surface height scan lines of a 14 nm thick graphite flake on InGaAs substrate, presenting a quite accurate and detailed copy of the underlying substrate texture even for such a large number of graphene layers.

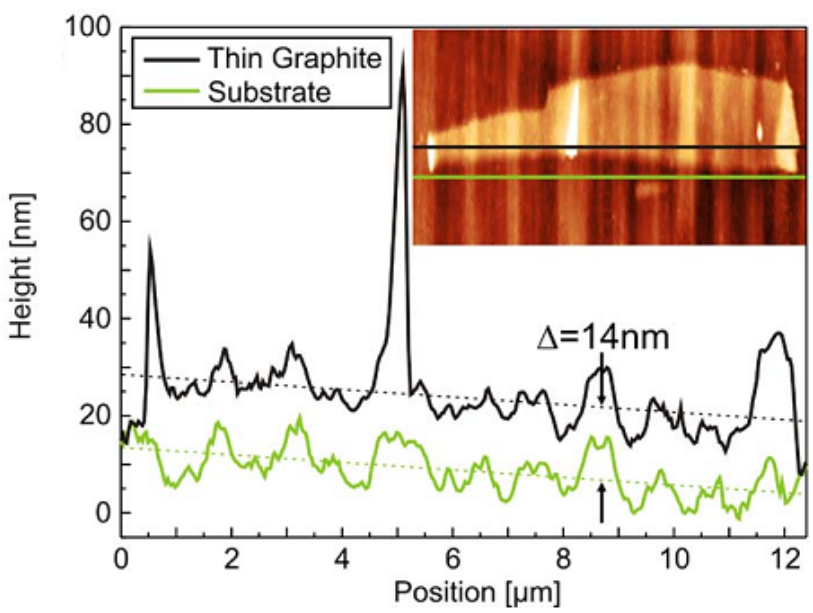

Figure 2.2. Linecuts on the AFM image of a 14 nm thin graphene flake and its $In_{0.75}Ga_{0.25}As$ substrate. The inset shows this flake and positions of the lines [67].

The extrinsic substrate regulation on the graphene morphology is shown to be strong enough to prevail over the intrinsic random corrugations in graphene. A recent work compared the graphene morphology on a SiO_2 substrate (Figure 2.3a) with that on an atomically flat mica surfaces (Figure 2.3b) [76]. The results showed that graphene on mica is much smoother than on SiO_2, approaching to the limit of atomic flatness.

Therefore, it is evident that intrinsic ripples in graphene can be strongly suppressed by interfacial van der Waals interactions.

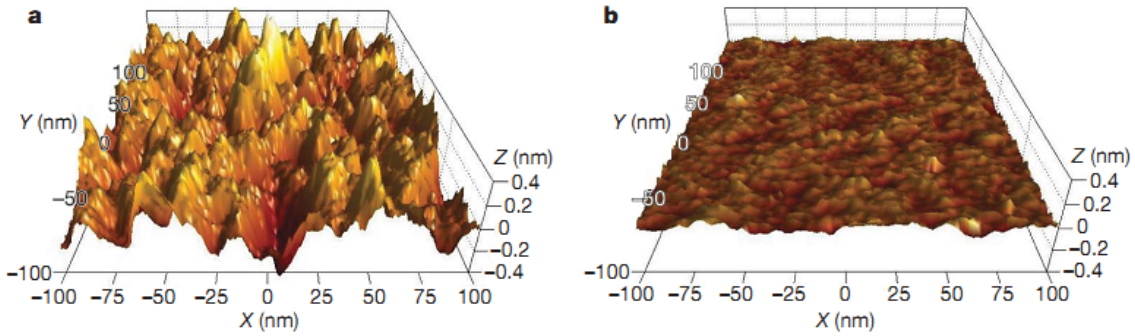

Figure 2.3. Three-dimensional representations of the AFM topographic data for graphene on SiO_2 (a) and on mica (b) [76].

Inspired by these experimental oberservations, we envision a promising strategy to regulate the graphene morphology via substrate surface engineered into desired pattern. The interaction between graphene and the substrate surface could suppress intrinsic ripples and tailor graphene conforming to the substrate surface pattern. However, because of the bending rigidity of graphene, graphene will only partially follow the substrate fluctuations, as observed in experiments. To achieve the substrate-regulated graphene morphology, the quantitative relationship between the graphene morphology and the substrate surface roughness has to be studied.

2.2. Energetic Framework

The equilibrium graphene morphology regulated by the underlying substrate is governed by the interplay among three types of free energies: (1) graphene-substrate interaction energy, (2) graphene strain energy and (3) substrate strain energy.

1) The interaction between mechanically-exfoliated graphene and its underlying substrate is usually weak and can be characterized by van der Waals forces. For graphene epitaxially grown from a substrate, the graphene-substrate interaction energy results from their chemical bonding. In practice, weak physical bonding (e.g., van der Waals forces) and strong chemical bonding may co-exist in the graphene-on-substrate structure. The contributions of the chemical bonding to the interaction energy is additive to that of the van de Waals bonding.
2) As the graphene partially conforms to the substrate surface morphology, the graphene strain energy increases, resulting from the out-of-plane bending as well as the in-plane stretching. Furthermore, the graphene out-of-plane deformation defines its resulting morphology.
3) The substrate strain energy depends on the substrate stiffness and the external mechanical loads. Graphene has been fabricated mostly on rigid substrates (e.g., SiO_2). Without external mechanical loads, the interaction between the ultra-thin graphene and the rather thick substrate results in negligible strain energy in the substrate. If the graphene, however, is transferred onto a flexible substrate (e.g., polymers or elastomers) [9, 77, 78], and the resulting structure is subject to large deformation, the strain energy of the substrate can become comparable to that of the graphene and the graphene-substrate interaction energy, and thus needs to be considered to determine the equilibrium graphene morphology.

In this Chapter, we assume weak interaction energy and rigid substrates, the most common situation in experiments. The graphene partially conforming to an underlying substrate can then be understood as follows. As the graphene corrugates to

follow the substrate surface morphology, the graphene strain energy increases due to the intrinsic bending rigidity of graphene; on the other hand, by partially conforming to the substrate, the graphene-substrate interaction energy decreases due to the nature of van der Waals interaction. The total free energy of the system (denoted by the sum of the graphene strain energy and the graphene-substrate interaction energy) minimizes, from which the equilibrium graphene morphology on the substrate can be determined (Figure 2.4).

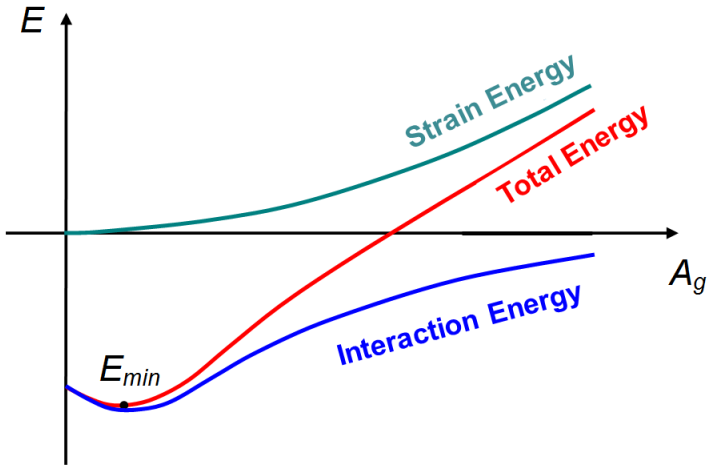

Figure 2.4. Schematics of the energetics of the substrate regulation on graphene morphology. The strain energy and the graphene-substrate interaction energy are plotted as functions of the graphene corrugation amplitude A_g. The total free energy minimizes at an equilibrium value of A_g. A similar energy profile holds for the total energy as a function of h (not shown).

2.3. Computational Model

The periodic substrate surface features can be either 1-dimensional (sinusoidal grooves) or 2-dimensional (checkerboard or herringbone wrinkles). A blanket graphene monolayer mechanically exfoliated on such a substrate partially conforms to

the substrate surface, thus assumes a corrugated morphology similar to the substrate surface grooves but with a smaller amplitude. If the features lie in *x*-*y* plane, the graphene morphology and the substrate surface can be described by $w_g(x,y)$and $w_s(x,y)$, respectively.

2.3.1. Graphene-substrate interaction energy

The graphene-substrate interaction energy is given by summing up all interaction energies due to van der Waals force between the carbon atoms in the graphene and the substrate atoms. The van der Waals force between a graphene–substrate atomic pair of distance r can be characterized by a Lennard–Jones pair potential,

$$V_{LJ}(r) = 4\varepsilon\left(\frac{\sigma^{12}}{r^{12}} - \frac{\sigma^{6}}{r^{6}}\right), \tag{2.1}$$

where $\sqrt[6]{2}\sigma$ is the equilibrium distance of a graphene-substrate atomic pair and ε is the bonding energy at the equilibrium distance. The number of atoms over an area dS on the graphene and a volume dV_s in the substrate are $\rho_c dS$ and $\rho_s dV_s$, respectively, where ρ_c is the homogenized carbon atom area density of graphene that is related to the equilibrium carbon-carbon bond length l by $\rho_c = 4/\left(3\sqrt{3}l^2\right)$, and ρ_s is the molecular density of substrate that can be derived from the molecular mass and mass density of substrate. It has been shown that the homogenized description of the discrete carbon atoms in graphene can capture the feature of the graphene-substrate interface [79, 80].

The interaction energy E_{int} between a graphene of area S and a substrate of volume V_s can be given by

$$E_{int} = \int_S \int_{V_s} V(r)\rho_s dV_s \rho_c dS \,, \tag{2.2}$$

Next, we take the morphology of graphene regulated by sinusoidal substrate surface as an example to show the detailed formulation of E_{int}. The sinusoidal corrugations of the substrate surface and the corrugations of the graphene regulated by such a substrate surface (Figure 2.5a) are described by

$$\begin{aligned} w_g(x) &= A_g \cos\left(\frac{2\pi}{\lambda}\right) \\ w_s(x) &= A_s \cos\left(\frac{2\pi}{\lambda}\right) - h, \end{aligned} \tag{2.3}$$

where λ is the groove wavelength, h is the distance between the middle planes of the graphene and the substrate surface, A_g and A_s are the amplitudes of the graphene corrugation and the substrate surface grooves, respectively (Figure 2.5b). Given the symmetry and periodicity of the structure in Figure 2.5, we only need to consider a graphene segment of a half sinusoidal period (e.g., $0 < x < \lambda/2$) and the underlying substrate.

The distance between a point $(x_g, 0, w_g)$ on the graphene and a point (x_s, y_s, z_s) in the substrate is

$$r = \sqrt{\left(x_g - x_s\right)^2 + y_s^2 + \left(w_g - z_s\right)^2}, \tag{2.4}$$

where $w_g(x) = A_g \cos\left(\frac{2\pi}{\lambda}\right)$ and $z_s \leq A_s \cos\left(\frac{2\pi}{\lambda}\right) - h$.

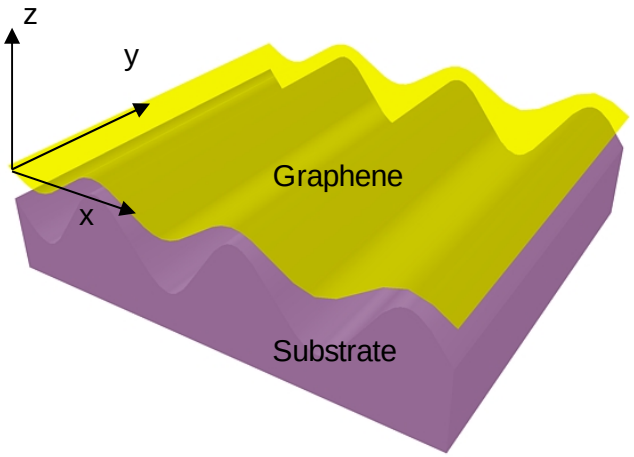

(a)

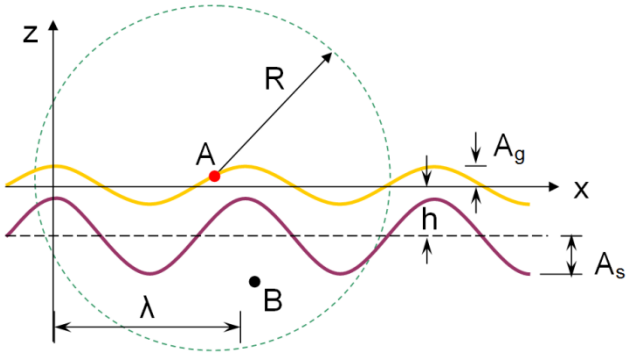

(b)

Figure 2.5. (a) Schematics of a blanket graphene partially conforming to a substrate with sinusoidal surface grooves. (b) The view of the graphene and the substrate surface. Point *A* denotes a carbon atom in the graphene, and point *B* denotes a substrate location within a distance of *R* from point *A*.

The graphene-substrate interaction energy per unit area over a half period of graphene is given by

$$E_{int} = \frac{1}{\lambda/2}\int_0^{\lambda/2} \rho_c dx_g \int_{V_s} V(r)\rho_s dV_s$$
$$= \frac{\rho_c \rho_s}{\lambda/2}\int_0^{\lambda/2} dx_g \int_{-\infty}^{\infty} dx_s \int_{-\infty}^{\infty} dy_s \int_{-\infty}^{A_s \cos\left(\frac{2\pi}{\lambda}\right)-h} V(r) dz_s, \quad (2.5)$$

where $V(r)$ is given by plugging Equation (2.4) into Equation (2.1). Since it will be vey complicated to analytically calculate this multiple integrals, the interaction energy defined in Equation (2.2) is then computed using a Monte Carlo numerical strategy as described below. Since the van der Waals force rapidly decays as the distance of an atom pair increases from its equilibrium value, the interaction energy between a carbon atom in the graphene and the underlying substrate can be estimated by the van de Waals interactions of this carbon atom with its adjacent portion of the substrate (e.g., within a cut-off distance from this carbon atom). If the cut-off distance is large enough, such an estimate of interaction energy converges to the theoretical value of E_{int}. Therefore, for a given carbon atom in the graphene, only the substrate portion within a distance of R to this carbon atom are taken into account in computing the graphene-substrate interaction energy (Figure 2.5b).

For the *i*th graphene carbon atom, *n* random locations are generated in the substrate portion within the cut-off distance R from this carbon atom. The interaction energy between this carbon atom and the substrate is estimated by

$$E_i = (\rho_s V_s/n) \sum_{j=1}^{n} V_{LJ}(r_{ij}), \tag{2.6}$$

where r_{ij} is the distance between the *i*th graphene carbon atom and the *j*th random substrate location.

Equation (2.6) is evaluated at m equally spaced locations over the graphene of area S. The graphene–substrate interaction energy over this area can then be estimated by

$$E_{int} = (\rho_c S/m) \sum_{i=1}^{m} E_i, \tag{2.7}$$

As *n*, *R* and *m* become larger, the values of Equation (2.7) converge to the theoretical value of Equation (2.5). For example, in the simulations of graphene on sinusoidal substrate surface, R = 3 nm, n = 10^6 and m = 100 lead to less than one percent variation of the estimated values of E_{int}.

2.3.2. Graphene strain energy

The strain energy in the graphene–substrate system results from the corrugating deformation of the graphene and the interaction-induced deformation of the substrate. When an ultrathin monolayer graphene partially conforms to a rigid substrate (e.g., SiO_2), the substrate deformation due to the weak graphene–substrate interaction is expected to be negligible. As the graphene spontaneously follows the surface morphology of the substrate under weak interaction (imagine a fabric conforms to a corrugated surface) and is not subject to any mechanical constraints (e.g., pinning [81]), the strain energy in the graphene mainly results from out-of-plane bending of

the graphene, while the contribution from in-plane stretching of the graphene to the strain energy is also expected to be negligible. Denoting the out-of-plane displacement of the graphene by $w_g(x, y)$, the strain energy E_g of the graphene over its area S can be given by

$$E_g = \int_S \frac{D}{2}\left[\left(\frac{\partial^2 w_g}{\partial x^2} + \frac{\partial^2 w_g}{\partial y^2}\right)^2 - 2(1-\nu)\left(\frac{\partial^2 w_g}{\partial x^2}\frac{\partial^2 w_g}{\partial y^2} - \left(\frac{\partial^2 w_g}{\partial x \partial y}\right)^2\right)\right] dS, \tag{2.8}$$

where D and ν are the bending rigidity and the Poisson's ratio of graphene, respectively.

The equilibrium morphology of the graphene on the substrate can then be determined by minimizing the total free energy $E_{int} + E_g$. For a given substrate surface morphology (i.e., λ and A_s), the graphene bending energy E_g is a function of the amplitude of graphene corrugation A_g, and monotonically increases as A_g increases (Figure 2.4). On the other hand, the graphene-substrate interaction energy E_{int} is a function of A_g and h. Due to the nature of van der Waals interaction, E_{int} minimizes at finite values of A_g and h (Figure 2.4). As a result, there exists a minimum value of $E_g + E_{int}$ where A_g and h define the equilibrium morphology of the graphene on the substrate (Figure 2.4). In simulations, the equilibrium values of A_g and h are obtained numerically by minimizing the sum of E_{int} (from Equation (2.7)) and E_g (from Equation (2.8)).

2.4. Graphene Morphology on a Substrate with Sinusoidal Surface Grooves

For a substrate with sinusoidal surface grooves, the graphene morphology and the substrate surface are described by Equation (2.3). By substituting Equation (2.3) into Equation (2.8), the graphene bending energy per unit area over such a half period is given by

$$E_g = \frac{1}{\lambda/2}\int_0^{\lambda/2} \frac{D}{2}\left(\frac{\partial^2 w_g}{\partial x^2}\right)^2 dx = \frac{4\pi^4 D A_g^2}{\lambda^4} \tag{2.9}$$

We will next describe the simulation results using the following dimensionless groups: A_g/A_s, h/σ, λ/A_s, D/ε, and $\left(E_g + E_{int}\right)A_s/D$. In all simulations in this section, we take $D = 1.41\,eV$, $\rho_c = 3.82 \times 10^{19} m^{-2}$, $\rho_s = 6.61 \times 10^{28} m^{-3}$, $\sigma = 0.38\,nm$ and $A_s = 0.5\,nm$. These values are representative of a graphene-on-SiO_2 material system [82-85]. Various values of D/ε (i.e., 25~2000) and λ/A_s (i.e., 1~30) are used to study the effects of interfacial bonding energy and substrate surface roughness. Also, we use R = 3nm, n = 10^6 and m = 100 in this Section. The simulations were conducted by running a parallel computer code through a multi-node high performance computing cluster.

Figures 2.6a and 2.6b show the normalized equilibrium amplitude of the graphene corrugation A_g/A_s and the normalized equilibrium graphene-substrate distance h/σ as a function of D/ε for various λ/A_s, respectively. For a given substrate surface roughness (i.e., λ/A_s), if the graphene-substrate interfacial bonding energy is strong

(i.e., small D/ε), A_g tends to A_s, while h becomes comparable to σ. In other words, the graphene closely follows the substrate surface morphology, and the equilibrium distance between the graphene and the substrate is comparable to the equilibrium

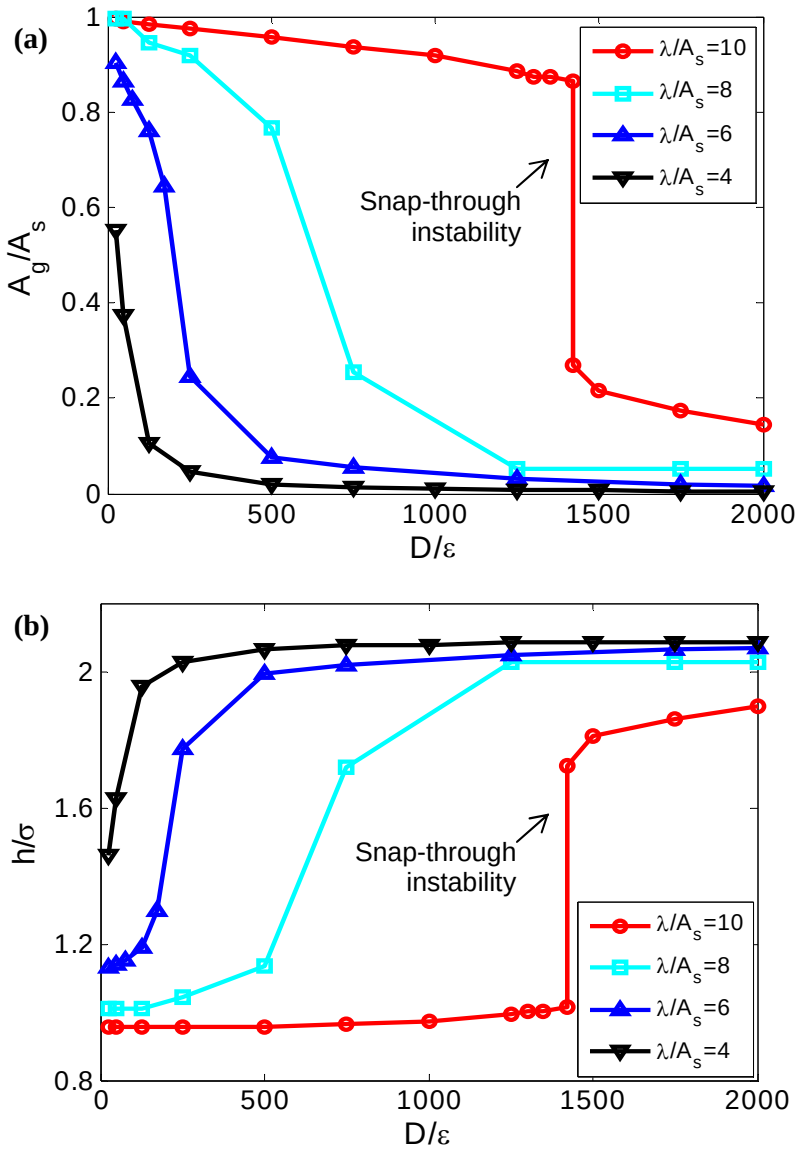

Figure 2.6. (a) A_g/A_s and (b) h/σ as functions of D/ε for various λ/A_s, respectively. For $\lambda/A_s = 10$ and $D/\varepsilon = 1420$, the equilibrium graphene morphology snaps between two distinct states: 1) closely conforming to the substrate surface and 2) nearly remaining flat on the substrate.

atomic distance defined in the Lennard-Jones potential. By contrast, if the graphene-substrate interfacial bonding is weak (i.e., large D/ε), A_g approaches zero, while h tends to 2.1σ. That is, the graphene is nearly flat and does not conform to the substrate surface. For a given interfacial bonding energy (i.e., D/ε), A_g increases and h decreases, as λ/A_s increases.

Worth noting in Figure 2.6a is that: for certain range of λ/A_s (e.g., λ/A_s = 4 or 10), there is a sharp transition in the equilibrium amplitude of the graphene corrugation as the interfacial bonding energy varies. Particularly, for λ/A_s = 10, A_g/A_s drops from 0.86 to 0.27, when D/ε = 1420 (Figure 2.6a). In other words, the graphene morphology snaps between two distinct states: closely conforming to the substrate surface and nearly remaining flat on the substrate surface, when the interfacial bonding energy reaches a threshold value. Such a snap-through instability of the graphene morphology on the substrate is also evident in Figure 2.6b.

Figure 2.7 provides the energetic understanding of the above snap-through instability. For λ/A_s = 10, when the interfacial bonding energy is low (e.g., D/ε = 1250), $\left(E_g + E_{int}\right)$ minimizes at A_g/A_s = 0.19. As D/ε increases, $\left(E_g + E_{int}\right)$ vs. A_g/A_s curve assumes a double-well shape. At a threshold value of D/ε = 1420, $\left(E_g + E_{int}\right)$ minimizes at both A_g/A_s = 0.86 and 0.27, corresponding to the two distinct states of the graphene morphology, respectively. For D/ε higher than the threshold value, the minimum of $\left(E_g + E_{int}\right)$ occurs at a larger A_g/A_s.

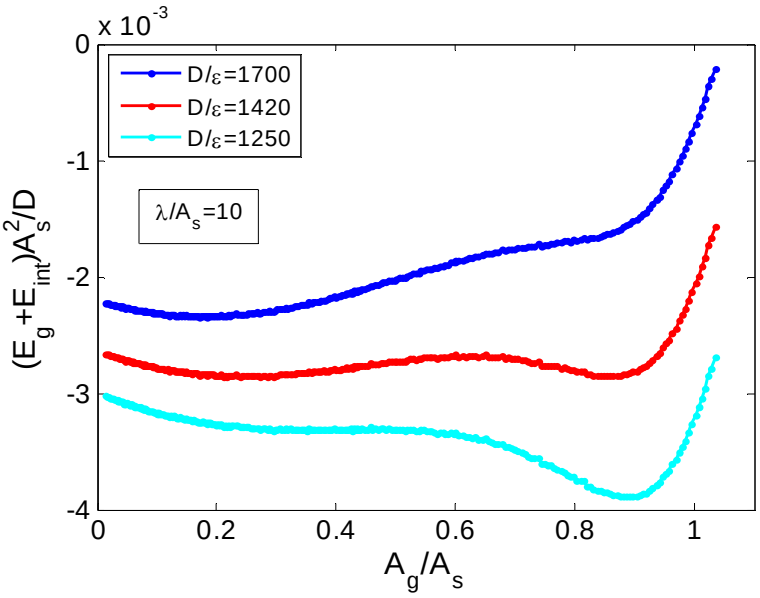

Figure 2.7. The normalized total energy as a function of A_g/A_s for various D/ε. At a threshold value of D/ε = 1420, $\left(E_g + E_{int}\right)$ minimizes at both A_g/A_s = 0.27 and 0.86, corresponding to the two distinct states of the graphene morphology, respectively.

Besides the interfacial bonding energy, the substrate surface roughness also can influence the graphene morphology. Figure 2.8a further shows the effect of substrate surface roughness λ/A_s on the graphene amplitude A_g/A_s for various values of D/ε. For a given interfacial bonding energy D/ε, there exists a threshold λ_{min}, smaller than which $A_g/A_s = 0$ (i.e., the graphene is flat, and thus not conforming to the substrate surface); and a threshold λ_{max}, greater than which A_g/A_s = 1 (i.e., the graphene fully conforming to the substrate surface). As λ increases from λ_{min} to λ_{max}, A_g/A_s ramps up from zero to one. This can be understood as follows. For a given amplitude of substrate surface groove A_s, if the groove wavelength λ is small, conforming to substrate surface results in a significant increase in the graphene bending energy (e.g., $E_g \propto 1/\lambda^4$ in Equation (2.9)). Consequently, A_g tends to zero.

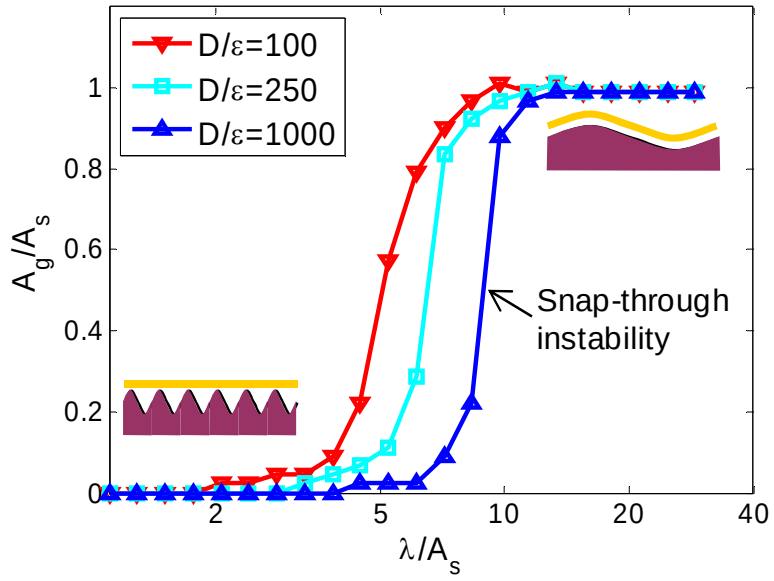

(a)

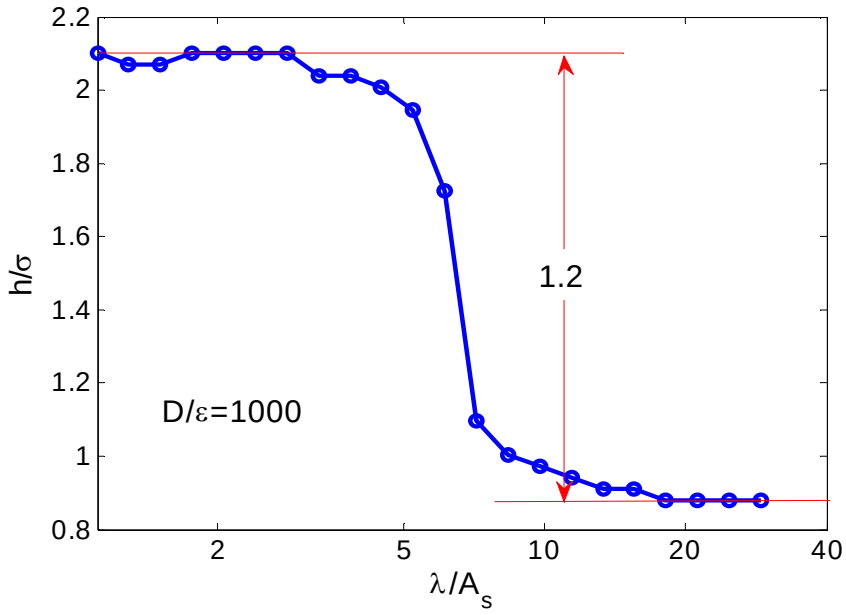

(b)

Figure 2.8. (a) A_g/A_s as a function of λ/A_s for various D/ε. The insets illustrate the two distinct states of the equilibrium graphene morphology. (b) h/σ as a function of λ/A_s for D/ε = 1000. The difference in the equilibrium distance of the two distinct states ($\Delta h/\sigma$ = 1.2) agrees well to the amplitude of the substrate surface groove (A_s/σ = 1.3).

On the other hand, if λ is large, the graphene bending energy becomes negligible; the graphene closely follows the substrate morphology (i.e., A_g/A_s tends to one). Figure 2.8b plots the equilibrium graphene-substrate distance h/σ as a function of λ/A_s for the case of D/ε = 1000. The equilibrium distance h tends to be constant when $\lambda < \lambda_{min}$ or $\lambda > \lambda_{max}$, corresponding to the two distinct states described above (as illustrated in the insets of Figure 2.8a). The difference in the equilibrium distance of the two distinct states is $\Delta h = 1.2\sigma$ = 0.459 nm, which is well close to the amplitude of the substrate surface groove A_s= 0.5 nm, further demonstrating the distinction between the graphene morphologies in the two limiting states.

Also worth of noting in Figure 2.8 is that, for certain range of graphene-substrate interfacial bonding energy (e.g., $D/\varepsilon >$ 1000), the snap-through instability of the graphene morphology, similar to that shown in Figure 2.6, exists. That is, the graphene morphology sharply switches between two distinct states: closely conforming to the substrate surface and nearly remaining flat on the substrate surface, when the substrate surface roughness λ/A_s reaches a threshold value. Such a threshold value increases as D/ε increases. The snap-through instability shown in Figure 2.8 also results from the double-well feature of the total energy profile at the threshold value of λ/A_s, similar to that shown in Figure 2.7.

2.5. Graphene Morphology on a Substrate with Herringbone or Checkerboard Corrugations

The out-of-plane herringbone corrugations of the substrate surface (Figure 2.9) and the out-of-plane corrugations of the graphene regulated by such a substrate surface are described by

$$w_s = A_s \cos\left[\frac{2\pi}{\lambda_x}\left(x + A_y \cos\left(\frac{2\pi y}{\lambda_y}\right)\right)\right] - h$$
$$w_g = A_g \cos\left[\frac{2\pi}{\lambda_x}\left(x + A_y \cos\left(\frac{2\pi y}{\lambda_y}\right)\right)\right], \tag{2.10}$$

respectively, where A_s and A_g are the amplitudes of the substrate surface corrugations and the graphene corrugations, respectively; for both the graphene and the substrate, λ_x is the wavelength of the out-of-plane corrugations, λ_y and A_y are the wavelength and the amplitude of in-plane jogs, respectively; and h is the distance between the middle planes of the graphene and the substrate surface. Given the symmetry of the herringbone pattern, we only need to consider a graphene segment over an area of $\lambda_x/2$ by $\lambda_y/2$.

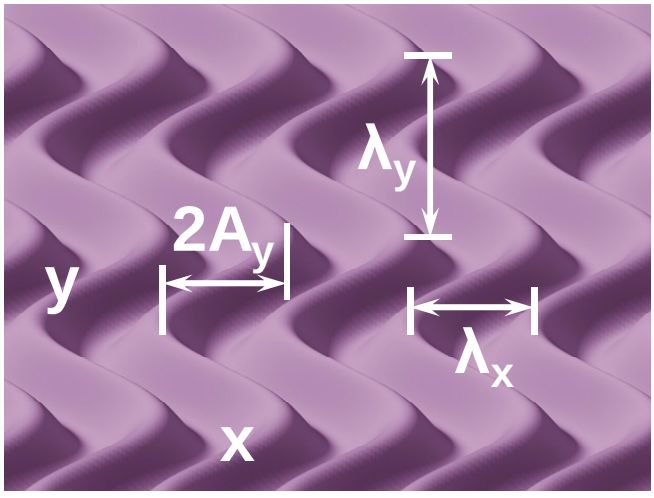

Figure 2.9. Schematics of substrate surface with herringbone corrugations

By substituting Equation (2.10) into Equation (2.8), the strain energy of such a graphene segment is given by

$$E_g = D\pi^4 A_g^2 \left(6\pi^4 A_y^4 + \lambda_y^4 + 2\pi^2 A_y^2 \left(\lambda_x^2 + 2\lambda_y^2\right)\right)/\lambda_x^3 \lambda_y^3. \qquad (2.11)$$

As shown in Equation (2.11), for a given substrate surface corrugation (i.e., A_s, A_y, λ_x, and λ_y), E_g increases monotonically as A_g increases. On the other hand, the graphene–substrate interaction energy, E_{int}, minimizes at finite values of A_g and h, due to the nature of van der Waals interaction. As a result, there exists a minimum of $(E_g + E_{int})$ where A_g and h reach their equilibrium values. The energy minimization was carried out by running a customized code on a high performance computation cluster. In all computations in this Section, D = 1.41 eV, l = 0.142 nm, ρ_s = 2.20 × 10^{28}/m^3, σ = 0.353 nm and A_s = 0.5 nm, which are representative of a graphene-on-SiO_2 structure [82, 85]. Various values of ε, λ_x, λ_y, and A_y were used to study the effects of interfacial bonding energy and substrate surface roughness on the regulated graphene morphology. Also, here we use cut-off distance R = 3 nm, n = 10^6, and m = 400.

Figures 2.10a plots the normalized amplitude of the regulated graphene corrugation, A_g/A_s, as a function of D/ε for various λ_x. Here $\lambda_y = 2\lambda_x$ and $A_y = \lambda_x/4$. Thus various λ_x define a family of substrate surfaces with self-similar in-plane herringbone patterns and the same out-of-plane amplitude (i.e., A_s). For a given substrate surface pattern, if the interfacial bonding energy is strong (i.e., small D/ε), A_g tends to A_s. In other words, the graphene closely follows the substrate surface (Figure 2.10b). In

contrast, if the interfacial bonding is weak (i.e., large D/ε), A_g approaches zero. That is, the graphene is nearly flat and does not conform to the substrate surface (Figure 2.10c). Interestingly, there also exists a threshold value of D/ε, below and above which a sharp transition occurs between the above two distinct states of the graphene morphology, similar to the snap-through instability of the graphene in Section 2.4. The threshold value of D/ε increases as λ_x increases. For a given interfacial bonding energy, A_g increases as λ_x increases. That is, graphene tends to conform more to a substrate surface with smaller out-of-plane waviness.

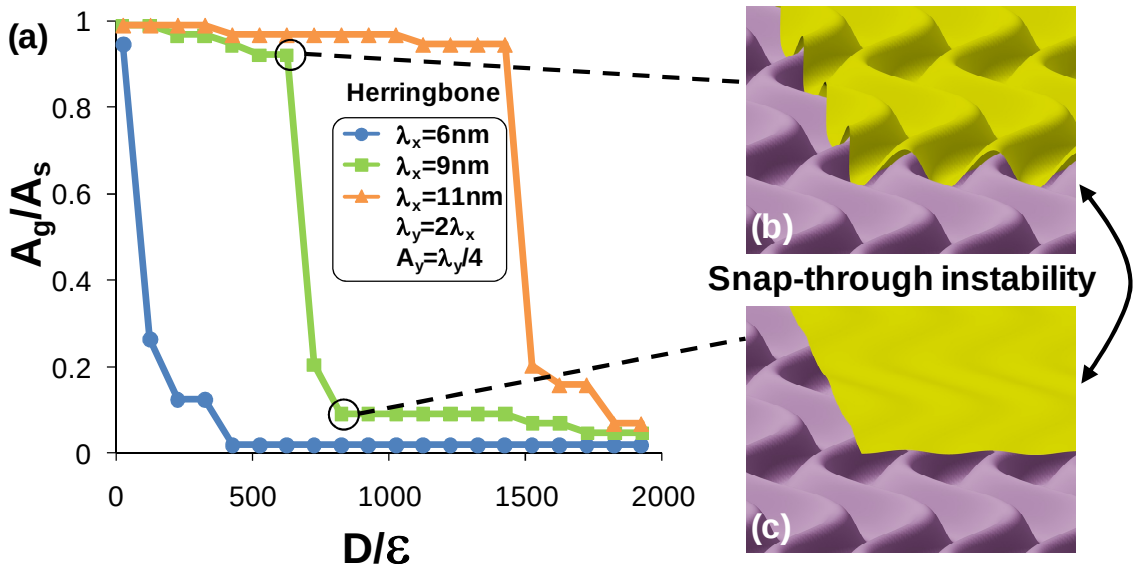

Figure 2.10. (a) A_g/A_s on substrates with herringbone surface corrugation as a function of D/ε for various λ_x. At a threshold value of D/ε, the graphene morphology snaps between two distinct states: (b) closely conforming to the substrate surface and (c) remaining nearly flat on the substrate surface.

Figure 2.11 shows the effect of in-plane waviness of the substrate surface on graphene morphology. Figure 2.11a plots A_g/A_s as a function of D/ε for various λ_y.

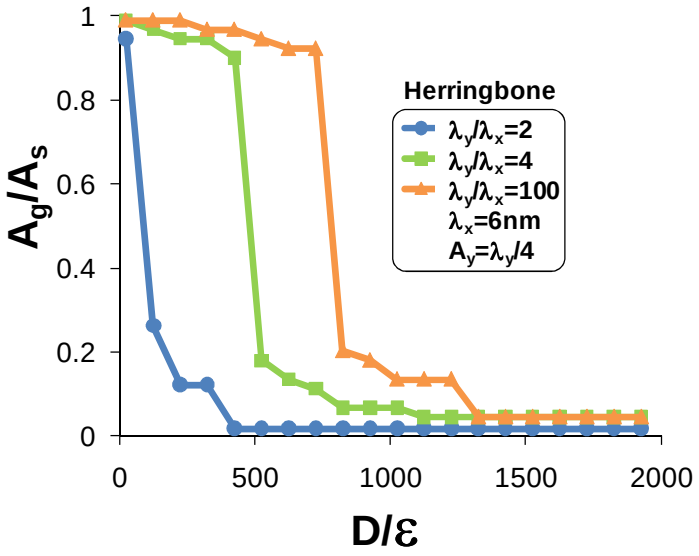

(a)

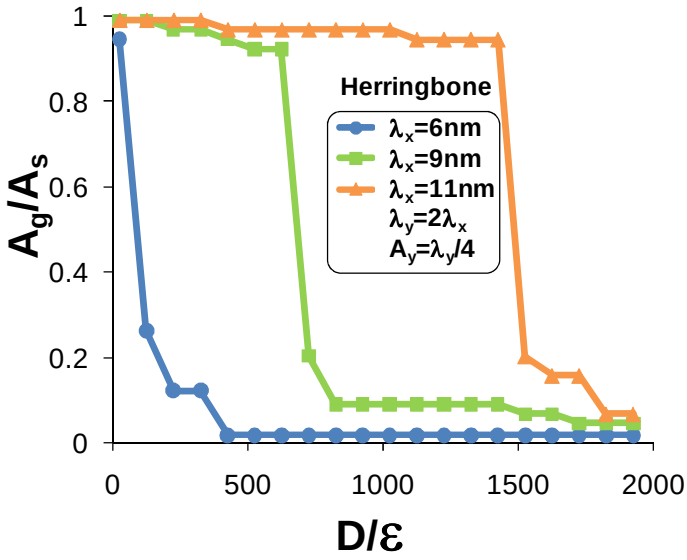

(b)

Figure 2.11. Effects of in-plane waviness of the substrate surface on graphene morphology. (a) A_g/A_s as a function of D/ε for various λ_y. (b) A_g/A_s as a function of D/ε for various A_y. The snap-through instability of graphene morphology, similar to that shown in Figure 2.10, is evident in both cases.

Here λ_x = 6 nm and $A_y = \lambda_y/4$. For a given substrate surface pattern, if the interfacial bonding energy is strong (i.e., small D/ε), A_g tends to A_s. For a given interfacial bonding energy, A_g increases as λ_y/λ_x increases. That is, graphene tends to conform more to a substrate surface with smaller in-plane waviness. In particular, when λ_y/λ_x is large (e.g., 100), the predicted graphene corrugation amplitude converges to that of graphene regulated by straight substrate surface grooves with the same λ_x and A_s. Figure 2.11b further plots A_g/A_s as a function of D/ε for various A_y with fixed λ_x and λ_y. Similar effect of in-plane waviness of the substrate surface on graphene morphology emerges from Figure 2.11b. Moreover, the snap-through instability of graphene, similar to that illustrated in Figure 2.10, is also evident in the results shown in Figure 2.11.

The snap-through instability of the graphene on a substrate surface can also be explained by the double well profile of total energy, similar to that in Section 2.4. Figure 2.12 plots the normalized total system energy as a function of A_g/A_s for various D/ε. Here λ_x = 9 nm, $\lambda_y = 2\lambda_x$ and $A_y = \lambda_y/4$. If the interfacial bonding energy is weaker (D/ε = 575) than a threshold value, the total energy profile reaches its minimum at a small graphene corrugation amplitude A_g/A_s = 0.14. If the interfacial bonding energy (D/ε = 750) is stronger than the threshold value, the total energy profile reaches its minimum at a large graphene corrugation amplitude A_g/A_s= 0.93. At the threshold value of D/ε = 650, the total energy profile assumes a double-well shape, whose two minima (A_g/A_s = 0.20 and 0.91) correspond to the two distinct states of the graphene morphology on the substrate surface.

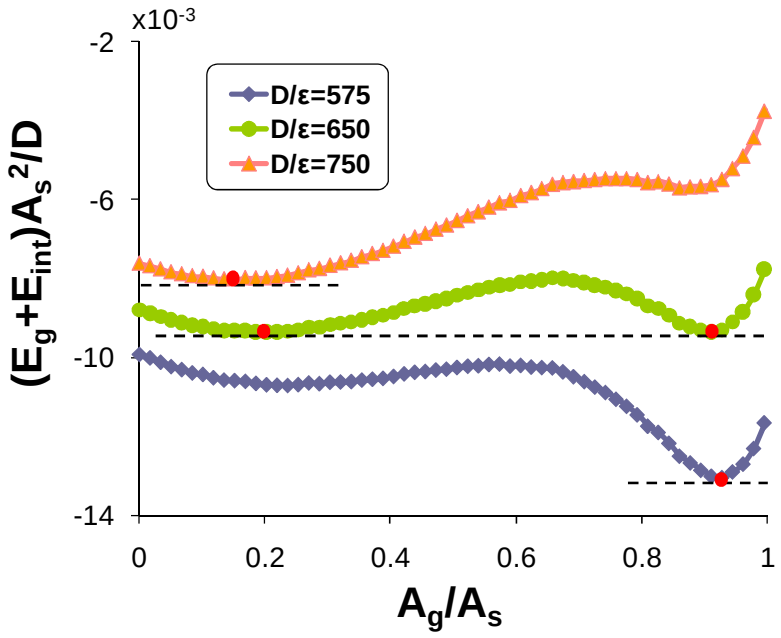

Figure 2.12. The normalized total system energy as a function of A_g/A_s for various D/ε. At a threshold value of D/ε, the total system energy minimizes at two points, corresponding to the two distinct states of graphene morphology.

In the case of graphene regulated by a substrate surface with checkerboard pattern (Figure 2.13), the substrate surface corrugation and the regulated graphene corrugation are described by

$$w_s = A_s \cos\left(\frac{2\pi x}{\lambda}\right)\cos\left(\frac{2\pi y}{\lambda}\right) - h$$
$$w_g = A_g \cos\left(\frac{2\pi x}{\lambda}\right)\cos\left(\frac{2\pi y}{\lambda}\right), \quad (2.12)$$

respectively, where λ is the wavelength of the out-of-plane corrugation for both the graphene and the substrate surface. Since checkerboard corrugation is also 2 dimensional symmetric, the interaction energy and strain energy are only calculated over an area $S = (\lambda/2) \times (\lambda/2)$. The numerical strategy similar to that

aforementioned was implemented to determine the equilibrium amplitude of the regulated graphene morphology.

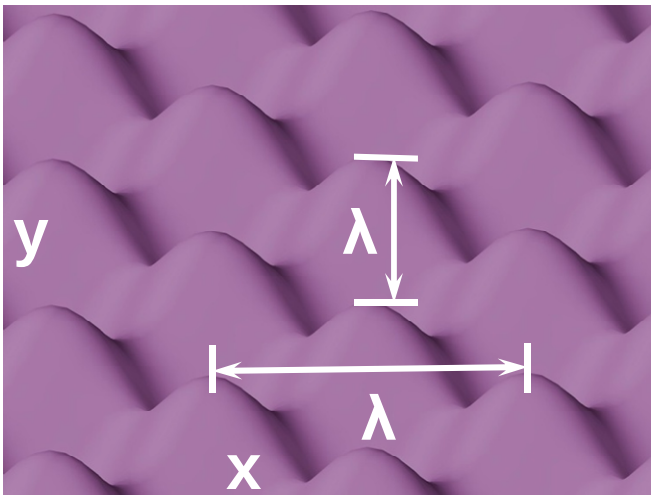

Figure 2.13. Schematics of substrate surface with checkerboard corrugations.

Figure 2.14 plots A_g/A_s on the checkerboard substrate surface as a function of D/ε for various λ. For a given substrate surface roughness, A_g/A_s decreases as D/ε increases. For a given interfacial bonding energy, A_g/A_s increases as λ increases. On a substrate surface with checkerboard corrugation, graphene exhibits the snap-through instability as well, which also results from the double-well shape of the system energy profile at the threshold value of D/ε, similar to that shown in Figure 2.11. The threshold value of D/ε at the graphene snap-through instability increases as λ increases.

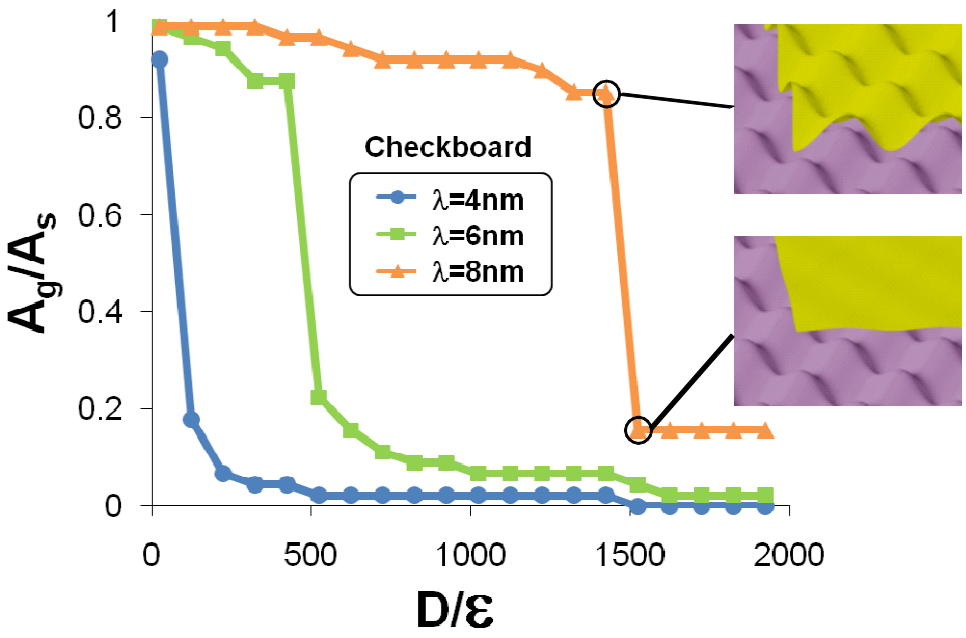

Figure 2.14. A_g/A_s on substrates with checkerboard surface corrugation as a function of D/ε for various λ. The insets illustrate the two distinct states of graphene morphology at the snap-through instability.

2.6. Discussions

The results reported here, combined with recent experimental observations, reveal a promising strategy to achieve quantitative control of the graphene morphology by tailoring the surface profile of the underlying substrate. While it is difficult to directly manipulate freestanding graphene at the atomistic scale, it is feasible to pattern the substrate surface with nano-scale features via micro/nano- fabrication techniques [68, 86-88]. The graphene on such a patterned substrate surface will assume a regular morphology, rather than random thermal fluctuation as in its freestanding counterpart. Such a strategy is justified by recent direct experimental observation of the suppression of any intrinsic ripples in graphene regulated by the atomically flat

terraces of cleaved mica surfaces [76]. This strong experimental evidence also suggests the robustness of the snap-through instability of graphene on substrates over the thermal fluctuations. If graphene can be tailored into desired morphologies, its unusual properties (e.g., tunable electrical conductivity and mobility), which are impossible in freestanding graphene, may be achieved. These unusual mechanical and electrical properties of the graphene can be potentially used to develop graphene-based devices. For example, the snap-through instability of the graphene can possibly enable the design of graphene switches for nano-electronics.

In our model, the graphene is assumed to adhere to the substrate surface spontaneously during fabrication and result in negligible deformation of the substrate. When a graphene-substrate laminate is subject to external loading, the graphene strain energy due to stretching and the substrate strain energy may also need to be considered to determine the graphene morphology. In this sense, the present model overestimates the equilibrium amplitude of the graphene morphology. We also assume the weak graphene/substrate interaction. In practice, it is possible to have chemical bondings or pinnings between the graphene and the substrate, leading to enhanced interfacial bonding [81, 89]. In this sense, the present model underestimates the equilibrium amplitude of the graphene morphology. The contribution of the chemical bonding to the interaction energy is additive to that of the van de Waals bonding, thus can be readily incorporated in the energetic framework. We also assume that the regulated graphene morphology has the same wavelength of the substrate surface grooves. This assumption is justified if the substrate surface is modestly rough. On a severely rough substrate surface, the graphene may assume

morphology of a longer wavelength to reduce the strain energy [90]. In this Chapter, we study the graphene morphology modulated by a substrate surface with one-dimensional or two-dimensional features. The surface features of natural substrates are often random in three dimensions. The equilibrium graphene morphology on such substrate surfaces is yet to be explored.

2.7. Summary

In this Chapter, we delineate a theoretical framework to determine the substrate-regulated morphology of the graphene through energy minimization. This framework is then applied to investigate the graphene morphology regulated by substrates with sinusoidal surface grooves, herringbone and checkerboard surface corrugations. Depending on interfacial bonding energy and substrate surface roughness, the graphene morphology exhibits a sharp transition between two distinct states: 1) closely conforming to the substrate surface and 2) remaining nearly flat on the substrate surface. This snap-through instability appears for all three substrate surface features. The graphene with controlled morphology could enable systematic exploration into the effect of corrugation-induced strain on the transport properties of graphene, an important but largely unexplored topic. Furthermore, the rich features of the substrate-regulated graphene morphology (e.g., the snap-through instability) could find their potential applications in designing new functional graphene device components.

Chapter 3: Graphene Morphology Regulated by Nanowires Patterned on a Substrate

In this Chapter, we quantitatively determine the graphene morphology regulated by nanowires patterned on a substrate surface. Thanks to the progress in nano-fabrication technology, it has become possible to fabricate nanowires patterned on substrates with diameter as small as several nanometers, which provides a new platform to regulate graphene morphology (Section 3.1). The computational model developed in Chapter 2 is extended for the graphene morphology regulated by the nanowires patterned in parallel on a substrate surface (Section 3.2). Simulations are conducted for two cases: (1) graphene regulated by widely spaced nanowires on a substrate surface, and (2) graphene regulated by densely spaced nanowires on a substrate surface. Particular efforts are focused on the effects of nanowire spacing and interfacial bonding energy on the regulated graphene morphology, as well as the snap-through instability of the graphene morphology. In order to capture the full characteristics of the graphene morphology regulated by ultrathin nanowires and determine the exact positions of each carbon atom in graphene at the equilibrium morphology, the morphologic interaction between graphene and Si nanowires on a SiO_2 substrate, using molecular mechanics simulations (Section 3.3). Two cases are considered: 1) a graphene nanoribbon intercalated by a single Si nanowire on a SiO_2 substrate and 2) a blanket graphene flake intercalated by an array of Si nanowires evenly patterned in parallel on a SiO_2 substrate. The results are summarized and discussed in Section 3.4.

3.1. Introduction

The past decade has seen significant progresses in fabricating low-dimensional nanostructures (e.g., nanowires and nanoparticles) with controllable size and shape. Particularly, fabricating silicon nanowires is more of interest to the researchers, given the central role of Si in the semiconductor industry. Therefore, many efforts have been made to fabricate of ultra-thin silicon nanowires. For example, silicon nanowires with diameter of 1 nm have been successfully prepared. Figure 3.1 shows a STM image of a silicon nanowire with diameter of 2 nm [72].

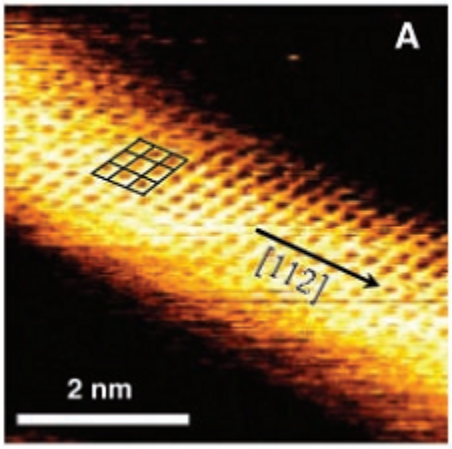

Figure 3.1. STM image of a silicon nanowire on a highly ordered pyrolytic graphite substrate. The arrow indicates the crystallographic direction [72].

Metal nanowires have also attracted much research interest because of the electron transport properties of the quantum wire. Suspended gold nanowires with diameter down to 0.6 nm have been made in an UHV (ultra-high vacuum)-TEM with the electron beam thinning technique [91]. The electron microscope image in Figure 3.2 shows the nanowire structure observed after the thinning.

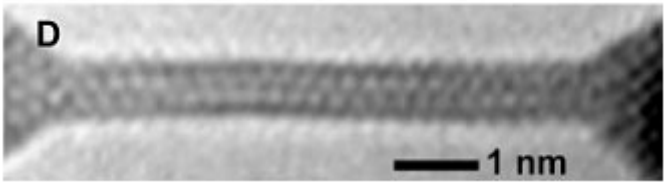

Figure 3.2. TEM images of stable gold nanowires observed after one thinning process. The diameter of the wire is 0.6 nm. The dark dots represent positions of atoms projected on the image plane [91].

There has also been promising demonstration of controllable patterning of nanowires of various materials on substrate surface via self-assembly or epitaxial growth. For example, using a technique based on translating thin film growth thickness control into planar wire arrays, well patterned nanowire arrays were fabricated with diameters and pitches (center-to-center distances) as small as 8 nanometers and 16 nanometers, respectively [73]. Figure 3.3 shows Pt nanowires fabricated by this technique with diameter of 8 nm at a pitch of 16 nm. Silicon nanowire arrays on a similar scale could also be made by this technique.

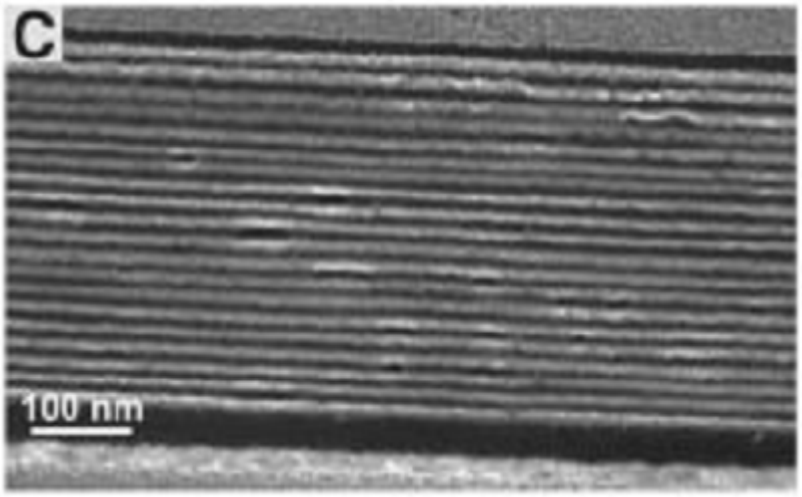

Figure 3.3. An aligned Pt nanowire array consists of 20 Pt nanowires 8 nm in diameter at a pitch of 16 nm [73].

These ultrathin nanowires patterned on a substrate surface can potentially serve as scaffolds to regulate the graphene morphology at an even higher resolution that approaches the atomic feature size of graphene (e.g., the carbon-carbon bond length in graphene is about 0.14 nm). Furthermore, the computational studies in Chapter 2 consider the graphene fully or partially conforming to idealized substrate surface features (e.g., sinusoidal grooves, herringbone corrugations), which thus results in well defined graphene morphology (i.e., similar to that of the substrate surface but with different out-of-surface amplitude). An array of nanowires patterned on a substrate defines a nonsmooth surface feature on which the graphene morphology can be fine tuned. The resulting graphene morphology cannot be readily predicted or extrapolated from the results of the abovementioned studies. Moreover, the energetic framework in Chapter 2 does not include the contribution of stretching to the graphene strain energy. Therefore, this Chapter aims to address the above concerns and establishes effective strategies for precise extrinsic regulation of the graphene morphology by nanowires

3.2. Graphene Morphology Regulated by Nanowires Patterned in Parallel on a Substrate Surface: a Continuum Mechanics Approach

3.2.1. Computational model

Figure 3.4 depicts the model configuration considered in Section 3.2, in which a blanket graphene partially conforms to an array of nanowires of diameter d_{nw} equally spaced in parallel on a substrate surface. Given the periodicity of the structure, in the rest of the section we focus on one period of the graphene and the underlying

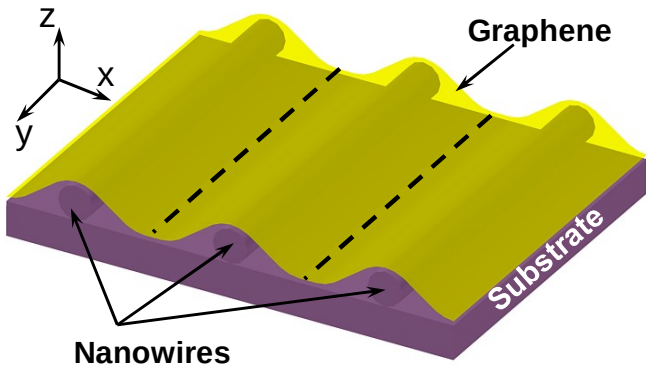

(a)

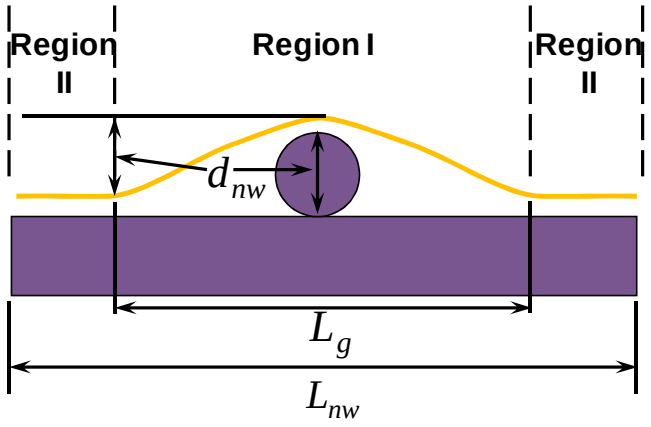

(b)

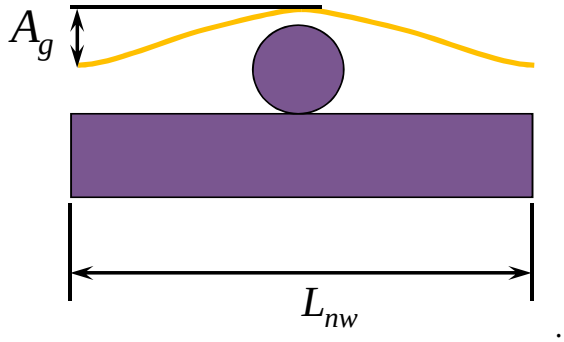

(c)

Figure 3.4. (a) Schematic of a blanket graphene regulated by nanowires patterned in parallel on a substrate surface. The graphene between the two dashed lines and the underlying nanowire and the substrate are modeled (e.g., in (b) and (c)) due to the configuration

symmetry. (b) and (c) depict two limiting cases of the regulated graphene morphology. (b) If the nanowire spacing L_{nw} is large, graphene corrugates to wrap around the nanowire in a region of width L_g (Region I) and remains flat on the substrate in Region II. The amplitude of the graphene corrugation is equal to the nanowire diameter d_{nw}. (c) If the nanowire spacing L_{nw} is small, graphene corrugates to partially conform to the envelope of the nanowire surfaces, with a period of L_{nw} and an amplitude A_g which is much smaller than d_{nw}.

substrate and the nanowire (Figure 3.4a). When the spacing between the nanowires, L_{nw}, is large, the graphene tends to wrap around each individual nanowire (e.g., Figure 3.4b). The regulated graphene morphology in one period can be divided into two regions. In region I, graphene corrugates to wrap around the nanowire; In region II the graphene remains flat on the substrate surface. The maximum amplitude of the graphene corrugation in region I is assumed to be equal to the diameter of the nanowire, as suggested by the graphene morphology regulated by substrate surface grooves in Chapter 2. The width of the corrugated graphene region I, L_g, is to be determined later in the Chapter. When the spacing between the nanowires is small, the graphene tends to partially wrap around the envelope of the nanowires with a maximum corrugation amplitude A_g which is smaller than the diameter of the nanowire, and a period that is equal to L_{nw} (Figure 3.4c). In Section 3.2, we will quantitatively determine: (1) L_g as a function of nanowire radius and interfacial bonding energies (graphene-substrate and graphene-nanowire) when $L_{nw} >> L_g$; and

(2) A_g as a function of nanowire radius and interfacial bonding energies when L_{nw} is comparable to or less than L_g.

The total interaction energy, denoted by E_{int}, including the interaction between a graphene of area S and a substrate of volume V_s, as well as that between such a graphene and the underlying nanowires of volume V_{nw}, is then given by

$$E_{\text{int}} = \int_S \int_{V_s} V_{LJ}^s(r)\rho_s dV_s \rho_c dS + \int_S \int_{V_{nw}} V_{LJ}^{nw}(r)\rho_{nw} dV_{nw} \rho_c dS \tag{3.1}$$

where V_{LJ}^s and V_{LJ}^{nw} are the Lennard–Jones pair potentials of the graphene-substrate interaction and the graphene-nanowire interaction, respectively, ρ_c is the homogenized carbon atom area density of graphene that is related to the equilibrium carbon–carbon bond length l by $\rho_c = 4/\left(3\sqrt{3}l^2\right)$, ρ_s and ρ_{nw} are the molecular density of the substrate and the nanowires, respectively, which can be derived from the molecular mass and mass density.

Following the similar Monte-Carlo numerical scheme described in Chapter 2, the two terms of multiple domain integrals in Equation (3.1) are computed separately and then summed up to obtain the total interaction energy.

The strain energy in the system of graphene spontaneously regulated by nanowires patterned on a substrate surface results from the corrugating deformation of the graphene and the interaction-induced deformation of the substrate and the nanowires. When an ultrathin monolayer graphene partially conforms to rigid nanowires patterned on a rigid substrate (e.g., SiO_2 nanowires on a SiO_2 substrate), the resulting

deformation of the substrate and the nanowires due to the weak graphene–substrate and graphene-nanowire interactions is expected to be negligible. Under such an assumption, the strain energy of the system is dominated by the strain energy of the graphene, which results from the out-of-plane corrugation and in-plane stretching of the graphene under nanowire/substrate regulation. The resulting strain energy in the substrate and the nanowires is thus not considered in this Section.

The deformation of the regulated graphene consists of both out-of-plane bending and in-plane stretching. Denoting the out-of-plane corrugation of the graphene by $w(x, y)$, the bending energy of the graphene is given by

$$E_b = \int_S D\left[\frac{1}{2}\left(\frac{\partial^2 w}{\partial x^2}+\frac{\partial^2 w}{\partial y^2}\right)^2-(1-\nu)\left(\frac{\partial^2 w}{\partial x^2}\frac{\partial^2 w}{\partial y^2}-\left(\frac{\partial^2 w}{\partial x \partial y}\right)^2\right)\right]dS \tag{3.2}$$

where D and ν are the bending rigidity and the Poisson's ratio of graphene, respectively.

The membrane energy of the graphene due to in-plane stretching is given by

$$E_s = \int_S \frac{Eh}{2(1-\nu^2)}\left[\left(\varepsilon_{xx}+\varepsilon_{yy}\right)^2+2(1-\nu)\left(\varepsilon_{xy}^2-\varepsilon_{xx}\varepsilon_{yy}\right)\right]dS \tag{3.3}$$

where E and h are the Young's Modulus and the thickness of graphene, respectively, ε_{xx}, ε_{yy} and ε_{xy} are the components of the in-plane membrane strain of the corrugated graphene.

The total strain energy of the graphene is then given by

$$E_g = E_b + E_s \tag{3.4}$$

We next apply the above consideration to compute the graphene strain energy for the two cases of nanowire spacing described at the beginning of Section 3.2.

Case 1: Graphene regulated by widely spaced nanowires on a substrate surface

When the spacing between the nanowires is large (i.e., $L_{nw} >> L_g$), the graphene strain energy results from the deformation of the graphene portion in region I. The graphene portion in region II is undeformed and thus has no contribution to the strain energy. Given the symmetry of the configuration (Figure 3.4b), the out-of-plane corrugation of graphene in region I, $w(x)$, is taken to be described by a cubic polynomial of *x*, whose coefficients can be determined by the following boundary conditions: $w = 0$ and $dw/dx = 0$ at $x = 0$, and $w = -d_{nw}$ and $dw/dx = 0$ at $x = L_g/2$. This consideration leads to

$$w(x) = 4d_{nw}\left(4\left(\frac{x}{L_g}\right)^3 - 3\left(\frac{x}{L_g}\right)^2\right) \tag{3.5}$$

We next determine the in-plane membrane strain of the graphene. Given the symmetry of the configuration, the membrane strain components ε_{yy} and ε_{xy} are taken to be zero. At the equilibrium morphology, in-plane shear stress acting on the graphene vanishes, which leads to a constant non-zero membrane strain ε_{xx} in the graphene portion in region I. That is,

$$\varepsilon_{xx} = \frac{du}{dx} + \frac{1}{2}\left(\frac{dw}{dx}\right)^2 = \text{constant.} \tag{3.6}$$

where $u(x)$ is in-plane displacement of graphene in x direction. The symmetric configuration requires the boundary conditions of $u(0) = u(L_g/2) = 0$. The above consideration leads to

$$\varepsilon_{xx} = \frac{12d_{nw}^2}{5L_g^2} = \text{constant.} \tag{3.7}$$

Substituting Equations (3.5) and (3.7) into Equations (3.2) and (3.3), respectively, the strain energy of the graphene is given by

$$E_g = E_b + E_s = \frac{48Dd_{nw}^2}{L_g^3} + \frac{36Ehd_{nw}^4}{25L_g^3\left(1-\nu^2\right)}. \tag{3.8}$$

Case 2: Graphene regulated by densely spaced nanowires on a substrate surface

When the spacing between the nanowires is small, the graphene partially conforms to the nanowires. The out-of-plane corrugation and the in-plane stretching of the graphene can be determined by a similar approach described above but with different boundary conditions.

For the out-of-plane corrugation of the graphene $w(x)$, the boundary conditions in this case are $w = 0$ and $dw/dx = 0$ at $x = 0$, and $w = -A_g$ and $dw/dx = 0$ at $x = L_{nw}/2$, where A_g is the maximum amplitude of the graphene corrugation that remains to be determined. These considerations lead to

$$w(x) = 4A_g\left(4\left(\frac{x}{L_{nw}}\right)^3 - 3\left(\frac{x}{L_{nw}}\right)^2\right). \tag{3.9}$$

For the in-plane displacement $u(x)$ of the graphene, the symmetric configuration requires the boundary conditions of $u(0) = u(L_{nw}/2) = 0$. These considerations lead to

$$\varepsilon_{xx} = \frac{12A_g^2}{5L_{nw}^2}. \tag{3.10}$$

Accordingly, the strain energy of the graphene in this case is given by

$$E_g = E_b + E_s = \frac{48DA_g^2}{L_{nw}^3} + \frac{36EhA_g^4}{25L_{nw}^3(1-\nu^2)}. \tag{3.11}$$

3.2.2. Regulated graphene morphology

The computational models described in Section 3.2.1 are used to compute the total system free energy ($E_{\text{int}} + E_g$) of the following two simulation cases.

Case 1: Graphene regulated by widely spaced nanowires on a substrate surface

In this case, the graphene portion near the nanowires corrugates and wraps around each nanowire, while the rest portion of graphene remains flat on the substrate surface. As shown in Equation (3.8), the graphene strain energy E_g monotonically decreases as the width of corrugated graphene portion L_g increases. On the other hand, due to the nature of van der Waals interaction, the interaction energy E_{int} minimizes at a finite value of L_g. As a result, there exists a minimum value of the

total system free energy ($E_{\text{int}} + E_g$), where L_g (i.e., the width) and d_{nw} (i.e., the amplitude) define the equilibrium morphology of the graphene regulated by widely spaced nanowires on a substrate surface.

Case 2: Graphene regulated by densely spaced nanowires on a substrate surface

In this case, the graphene partially conforms to the nanowires. As shown in Equation (3.11), the graphene strain energy E_g monotonically increases as the maximum amplitude of the graphene corrugation A_g increases. On the other hand, due to the nature of van der Waals interaction, the interaction energy E_{int} minimizes at a finite value of A_g. As a result, there exists a minimum value of the total system free energy ($E_{\text{int}} + E_g$), where L_{nw} (i.e., the period) and A_g (i.e., the amplitude) define the equilibrium morphology of the graphene regulated by densely spaced nanowires on a substrate surface.

The energy calculation and minimization are carried out by running a customized code on a high performance computer cluster. In all simulations, we use $D = 1.41\,\text{eV}$, $E = 1\,\text{TPa}$, $h = 0.34\,\text{nm}$, $\nu = 0.4$, $l = 0.142\,\text{nm}$, $\rho_s = \rho_w = 2.20 \times 10^{28}\,/\,\text{m}^3$ and $\sigma = 0.353\,\text{nm}$ [82, 85]. These parameters are representative of a graphene/SiO_2 nanowire/SiO_2 substrate material system. Various values of d_{nw}, L_{nw} and ε are used to study the effects of nanowire size and spacing as well as the interfacial bonding energy on the regulated graphene morphology.

3.2.3. Results and discussion

Case 1: Graphene regulated by widely spaced nanowires on a substrate surface

Figure 3.5a plots the equilibrium width of the corrugated graphene region I, L_g, as a function of the nanowire diameter d_{nw} for various values of D/ε. For a given interfacial bonding energy (i.e., a given value of D/ε), L_g increases as the nanowire diameter d_{nw} increases in an approximately linear manner, as indicated by the straight fitting lines in Figure 3.5a. In other words, the width of the corrugated graphene region is generally linearly proportional to the nanowire size. For a given nanowire diameter d_{nw}, L_g decreases as the interfacial bonding energy between graphene and nanowire/substrate increases (i.e., smaller value of D/ε). That is, a stronger interfacial bonding results in a narrower region of corrugated graphene. The effect of interfacial bonding energy on graphene morphology is further elucidated by the L_g vs. D/ε curves in Figure 3.5b for various values of d_{nw}. Emerging from Figure 3.5b is an apparent power law dependence of L_g on D/ε. Combined with the linear dependence of L_g on d_{nw} that is evident in Figure 3.5a, the correlation between the width of corrugated graphene region and the nanowire size as well as the interfacial bonding energy can be described by

$$\frac{L_g}{d_{nw}} \cong 3.84\left(\frac{D}{\varepsilon}\right)^{\frac{1}{4}}. \tag{3.12}$$

Together with Equation (3.5), Equation (3.12) offers a rule-of-thumb estimate of the graphene morphology regulated by widely spaced nanowires on a substrate surface, agreeing with the full-scale simulation results within 5%.

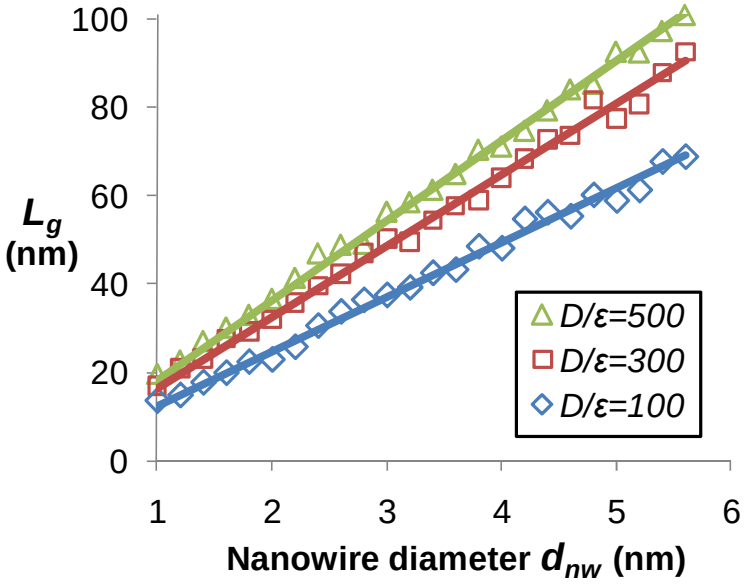

(a)

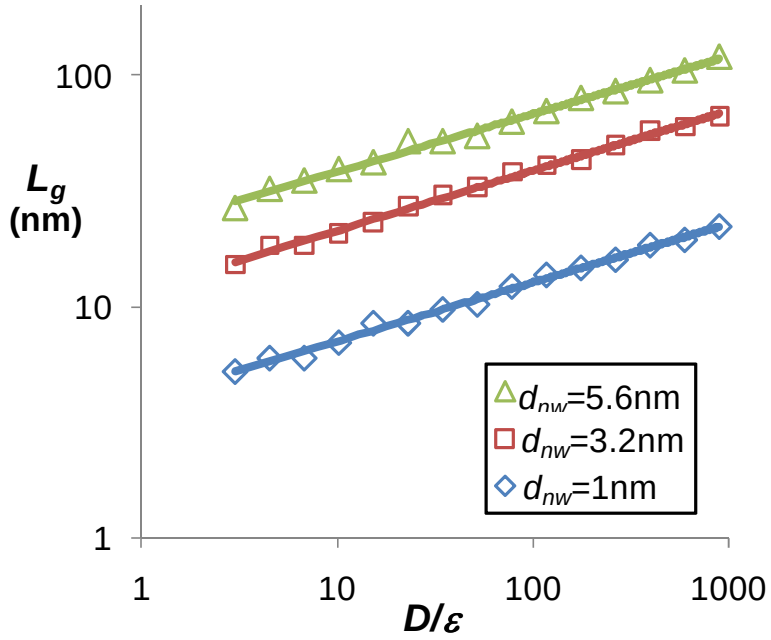

(b)

Figure 3.5. (a) The equilibrium width of the corrugated graphene region I, L_g, as a function of the nanowire diameter d_{nw} for various values of D/ε. The straight fitting lines denotes the linear dependence of L_g on d_{nw}. (b) L_g as a function of D/ε for various values of d_{nw}. The

straight fitting lines denotes the power law dependence of L_g on D/ε (note the logarithmic scales of both axes).

Case 2: Graphene regulated by densely spaced nanowires on a substrate surface

Figure 3.6a plots the amplitude of graphene corrugation normalized by the nanowire diameter A_g / d_{nw} as a function of the spacing between nanowires L_{nw} for two nanowire diameters $d_{nw} = 2.0nm$ and $3.2nm$. Here, $D/\varepsilon = 300$. For a given nanowire size (i.e., d_{nw}), if the spacing between nanowires L_{nw} is large, A_g / d_{nw} tends to one. In other words, the graphene can fully wrap around the nanowires, leading to a corrugated morphology that can be described by $w(x) = 4d_{nw}(4(x/L_{nw})^3 - 3(x/L_{nw})^2)$. By contrast, if the spacing between nanowires L_{nw} is small, A_g / d_{nw} approaches zero. That is, the graphene is nearly flat and does not conform to the patterned nanowires. Such a trend can be understood as follows. For a given nanowire size, if the spacing between nanowires is small, conforming to each nanowire results in a significant increase in the graphene strain energy (note that $E_g \propto 1/L_{nw}^3$ in Equation (3.11)). Consequently, A_g tends to zero. On the other hand, if L_{nw} is large, the resulting graphene strain energy is limited even when A_g / d_{nw} tends to one. Consequently, the graphene tends to closely follow the surface envelope of the patterned nanowires.

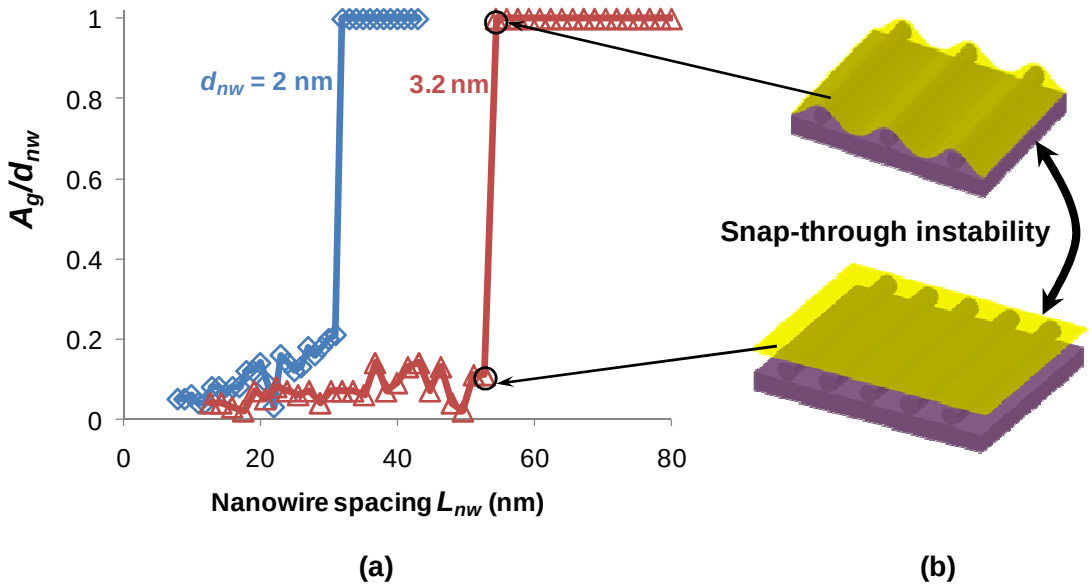

Figure 3.6. (a) The amplitude of graphene corrugation normalized by the nanowire diameter A_g / d_{nw} as a function of nanowire spacing L_{nw} for two nanowire diameters $d_{nw} = 2.0nm$ and 3.2*nm*. Here, $D/\varepsilon = 300$. As the nanowire spacing approaches a critical value L_{nw}^{cr}, the graphene morphology snaps between two distinct states: (1) closely conforming to the envelope of the nanowires patterned on a substrate surface and (2) nearly remaining flat on the nanowires patterned on a substrate surface, as illustrated in (b).

A significant feature shown in Figure 3.6a is the sharp transition in the equilibrium amplitude of the graphene corrugation as the nanowire spacing varies. For example, for $d_{nw} = 3.2nm$, A_g / d_{nw} raises abruptly from 0.1 to 1.0, as L_{nw} varies slightly from 52.8*nm* to 54.4*nm*. In other words, the graphene morphology snaps between two distinct states (Figure 3.6b): (1) closely conforming to the envelope of the nanowires patterned on a substrate surface and (2) nearly remaining flat on the nanowires patterned on a substrate surface, when the spacing of nanowires reaches a critical value, L_{nw}^{cr}. Further comparison shows that the critical nanowire spacing is

approximately equal to the width of corrugated graphene region L_g determined in Section 3.2.3 A (e.g., in Figure 3.5 or Equation (3.12)). For example, Equation (3.12) gives $L_g = 51.1nm$ for $d_{nw} = 3.2nm$ and $D/\varepsilon = 300$, which agrees well with the critical nanowire spacing defined in Figure 3.6. Such a snap-through instability of graphene morphology is similar to that of graphene morphology regulated by the underlying substrate surface with engineered nanoscale patterns (e.g., surface grooves, herringbone or checkerboard wrinkles). It has been shown that the snap-through instability of graphene morphology results from a double-well profile of total free energy of the system (i.e., $E_g + E_{\text{int}}$) as a function of the amplitude of the graphene morphology (e.g., A_g) at a critical value of surface feature size (e.g., nanowire spacing, surface groove roughness, etc.). For example, the simulation results in this Section show that ($E_g + E_{\text{int}}$) minimizes at two values of A_g when $L_{nw} = L_{nw}^{cr}$.

Emerging from the results in Section 3.2.3 A and B is a coherent understanding of the graphene morphology regulated by nanowires patterned in parallel on a substrate surface: for a given nanowire size (e.g., d_{nw}) and graphene/nanowire/substrate interfacial bonding energy (e.g., D/ε), there exists a critical nanowire spacing L_{nw}^{cr}, which can be estimated by $L_{nw}^{cr} \cong 3.84 d_{nw} \left(D/\varepsilon\right)^{1/4}$. If the nanowire spacing L_{nw} is greater than L_{nw}^{cr}, graphene can corrugate to wrap around the nanowires, with a maximum amplitude equal to the nanowire diameter and in a region of width equal to L_{nw}^{cr}. The morphology of the corrugated portion of graphene can then be described by

$$w(x) = \begin{cases} 4d_{nw}(4(x/L_{nw}^{cr})^3 - 3(x/L_{nw}^{cr})^2) & 0 < x < L_{nw}^{cr} \\ 0 & L_{nw}^{cr} < x < L_{nw} \end{cases}. \quad (3.13)$$

By contrast, if the nanowire spacing L_{nw} is smaller than L_{nw}^{cr}, graphene remains near flat on the patterned nanowires. When $L_{nw} = L_{nw}^{cr}$, the regulated graphene morphology snaps between the above two distinct states.

The above understanding also implies that, besides the nanowire spacing, the interfacial bonding energies can influence the graphene morphology. Figure 3.7 further shows the effect of D/ε on the normalized amplitude of graphene corrugation A_g / d_{nw} for various values of L_{nw}. Here, $d_{nw} = 3.2nm$. For a given nanowire spacing L_{nw}, if the interfacial bonding is strong (i.e., small D/ε), A_g / d_{nw} tends to one (i.e., graphene wraps around nanowires); if the interfacial bonding is weak (i.e., large D/ε), A_g / d_{nw} approaches zero (graphene does not conform to the nanowires). There also exists a snap-through instability at which the graphene morphology switches abruptly between the abovementioned two distinct states when D/ε reaches a critical value, for a given value of L_{nw}. For example, such a critical value of D/ε is about 15, 100 and 400 for L_{nw} =24*nm*, 40*nm* and 56*nm*, respectively. Substituting these critical values of D/ε into Equation (3.12) yields L_{nw} = 24.2*nm*, 38.9*nm* and 55.0*nm*, respectively, further demonstrating quite well agreement with the simulation results.

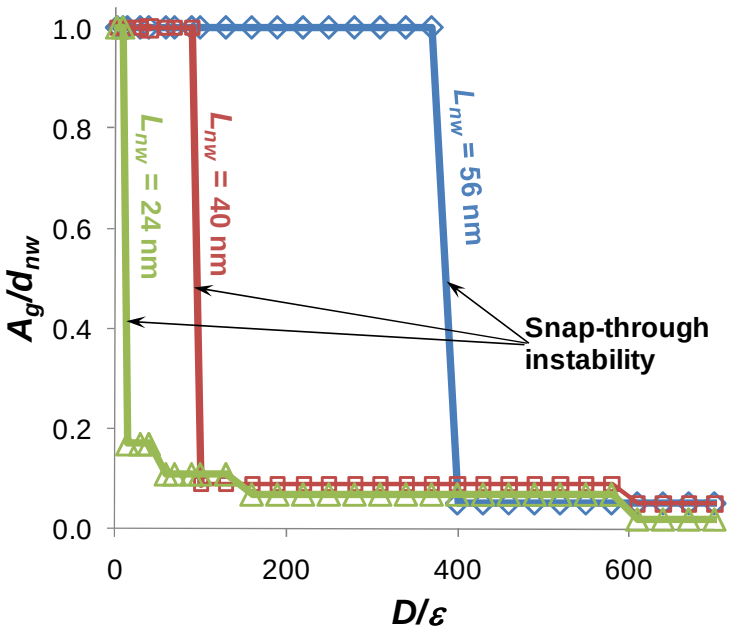

Figure 3.7. A_g / d_{nw} as a function of D/ε for various values of L_{nw}. Here, $d_{nw} = 3.2nm$. Note the snap-through instability similar with that in Figure 3.6 as D/ε reaches a critical value for a given value of L_{nw}.

3.2.4. Concluding remarks

In Section 3.2, we determine the graphene morphology regulated by nanowires patterned in parallel on a substrate surface through energy minimization. The equilibrium graphene morphology is governed by the interplay between the corrugation-induced strain energy of the graphene and the interaction energy between the graphene and the underlying nanowires and substrate. The graphene strain energy consists of the contribution from both out-of-plane bending and in-plane stretching, which are derived from nonlinear plate theory. The interaction energy is characterized by the sum of all atomic pair potential between the graphene carbon atoms and the substrate atoms/molecules, which is computed through a Monte Carlo type numerical

scheme. The major conclusions emerging from the modeling results are summarized as follows:

- The graphene morphology on nanowires evenly patterned in parallel on a substrate surface can be regulated by the nanowire size, nanowire spacing, and interfacial bonding energy between the graphene and the nanowire and that between the graphene and the substrate surface.

- For a given nanowire size and a given interfacial bonding energy, there exists a critical nanowire spacing, greater than which the graphene can conform to the surface envelope of the patterned nanowires, while smaller than which the graphene remains nearly flat on the nanowires. The graphene morphology snaps between these two distinct states at the critical nanowire spacing. The conforming morphology of the graphene can be quantitatively determined.

- For a give nanowire size and spacing, there exists a critical interfacial bonding energy, higher than which the graphene can conform to the surface envelope of the patterned nanowires, while lower than which the graphene remains nearly flat on the nanowires. The snap-through instability of graphene morphology also exists at this critical interfacial bonding energy.

- The abovementioned critical nanowire spacing, critical interfacial bonding energy and the nanowire size can be correlated by $L_{nw}^{cr} / d_{nw} \cong 3.84\left(D/\varepsilon\right)^{1/4}$, a rule-of-thumb estimate that agrees quite well with the full-scale simulation results.

3.3. Morphologic Interaction between Graphene and Si Nanowires on a SiO_2 Substrate: a Molecular Mechanics Study

The continuum mechanics model in Section 3.2 cannot capture the full characteristics of the graphene morphology regulated by ultrathin nanowires (e.g., with diameters on the order of 1 nm). Furthermore, the continuum model cannot determine the exact positions of each carbon atom in graphene at the equilibrium morphology. Such information will be needed in further first principle calculation of the electronic properties of the graphene. To address the above concerns, in Section 3.3, we carry out molecular mechanics (MM) simulations to study the morphological interaction between graphene nanoribbons/flakes and Si nanowires on a SiO_2 substrate.

3.3.1. Computational model

Figure 3.8 depicts the two configurations simulated in this Section: (1) a graphene nanoribbon of finite width in *y*-direction on a SiO_2 substrate with a Si nanowire intercalating in between (Figure 3.8a) and (2) a blanket graphene flake intercalated by an array of Si nanowires patterned in parallel on a SiO_2 substrate (Figure 3.8b). Given the periodicity of these two configurations, only the portion of the graphene marked by dash lines and the corresponding nanowire and substrate underneath are simulated. In the MM simulations, periodic boundary conditions are applied to the two end surfaces in *y*-direction in Figure 3.8a, and to the end surfaces in both *x*-and *y*-directions in Figure 3.8b. The depth of the MM simulation box in *y*-direction is 30 Å and the substrate thickness is 15 Å, larger than the cut-off radius in calculating van der Waals force. The width of the graphene portion demarcated by the dash lines and

that of the underlying substrate in *x*-direction, and the nanowire diameters are varied to study their effects on the graphene morphology.

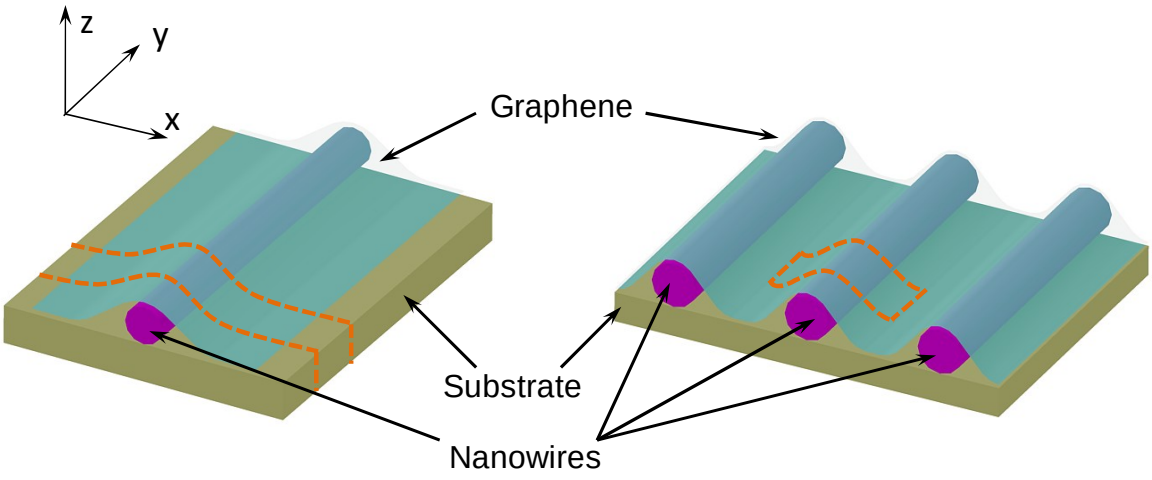

Figure 3.8. Schematics of two simulation cases. (a) A graphene nanoribbon intercalated by a Si nanowire on a SiO_2 substrate; (b) A blanket graphene flake intercalated by an array of Si nanowires evenly patterned in parallel on a SiO_2 substrate. The dash lines delineate the portion of graphene and the underlying nanowire and substrate simulated by molecular mechanics in each case.

The C-C bonding energy in the graphene is described by the second generation Brenner potential [92]. The interaction energy between the graphene and the nanowires and that between the graphene and the substrate are computed by the sum of the van der Waals forces between all C-Si and C-O atomic pairs in the system. These two types of van der Waals forces are described by two Lennard-Jones (LJ) pair potentials, respectively, both of which take the general form of $V(r) = 4\varepsilon(\sigma^{12}/r^{12} - \sigma^6/r^6)$, where $\sqrt[6]{2}\sigma$ is the equilibrium distance of the atomic pair and ε is the bonding energy at the equilibrium distance. Parameters in the C-Si pair

potential and those in the C-O pair potential are listed in Table 3.1. To reduce the computation cost, the bonding energy in the Si nanowire and the SiO_2 substrate, and the non-bonding Si-SiO_2 interaction are assumed to be constant, thus not considered in the energy minimization. This assumption is justified given the rigidity of Si and SiO_2 solids compared with the out-of-plane flexibility of a graphene monolayer.

Table 3.1. LJ potential parameters used in molecular mechanics simulations [93]

	ε (eV)	σ (Å)
C-Si	0.00213	1.506
C-O	0.00499	2.256

In each MM simulation case, the graphene is prescribed with an initial morphology that partially conforms to the envelope defined by the nanowire and the substrate surface (e.g., in Figure 3.8). The carbon atoms in the graphene then adjust their spatial positions to minimize the system energy, and eventually define the equilibrium morphology of the graphene. The total energy of the system is minimized using the limited-memory Broyden-Fletcher-Goldfarb-Shanno (BFGS) algorithm [94], until the total net force is less than 10^{-6} eV/ Å. The MM simulations are carried out by running a code in a high performance computer cluster.

3.3.2. Results and discussions

Case 1: Morphological interaction between a graphene nanoribbon and a Si nanowire on a SiO_2 substrate

We consider the interaction between a graphene nanoribbon of finite width W and a Si nanowire of diameter d on a SiO_2 substrate. Such a structure can be fabricated by transfer printing a mechanically exfoliated graphene nanoribbon onto a SiO_2-supported Si nanowire [95], with the length direction of the graphene nanoribbon parallel to the axial direction of the nanowire. As will be shown in this section, the regulated morphology of the graphene nanoribbon depends strongly on its width W and the nanowire diameter d.

If W is smaller than or comparable to d, the morphology of such a narrow graphene nanoribbon is mainly determined by the interaction between the graphene and the nanowire, and that between the graphene and the substrate becomes negligible. Depending on the relative value of W and d, the narrow graphene nanoribbon can have two different morphologies, as illustrated in Figure 3.9. For example, on a Si nanowire of d = 4 nm, a graphene nanoribbon of W = 6 nm remains nearly flat (Figure 3.9a). By contrast, on Si nanowire of d = 10 nm, a graphene nanoribbon of W = 12 nm fully conforms to the surface of the Si nanowire (Figure 3.9b). These two different morphologies of the graphene nanoribbon can be explained as follows. The strain energy density of the graphene due to out-of-plane bending approximately scales with the square of the local curvature of the graphene. Therefore, the graphene strain energy due to conforming to the Si nanowire surface is roughly proportional to $1/d^2$. If the Si nanowire is too thin, the significant increase of the graphene strain energy can overbalance the decrease of the graphene-nanowire interaction energy due to graphene conforming to the nanowire. As a result, the graphene nanoribbon remains nearly flat on the Si nanowire. On the other hand, if the Si nanowire is

sufficiently thick, the decrease of the interaction energy outweighs the increase of the graphene strain energy. Consequently, the graphene nanoribbon conforms to the nanowire surface. Also note when the graphene nanoribbon remains nearly flat on the Si nanowire, the two free edges in *y*-direction form ripples due to the edge stress in the graphene nanoribbon [40].

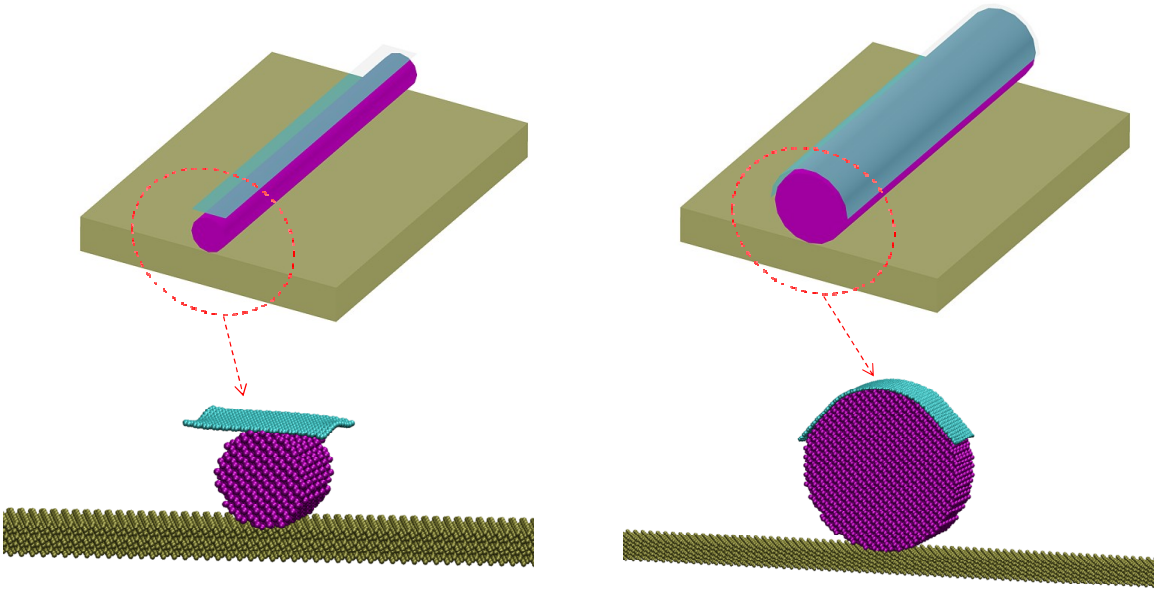

Figure 3.9. (a) On a nanowire of diameter of 4 nm, a narrow graphene nanoribbon of width of 6 nm remains nearly flat, with slight ripples along two long edges. (b) On a nanowire of diameter of 10 nm, a narrow graphene nanoribbon of width of 12 nm can fully conform to the nanowire surface.

If W is much larger than d, the equilibrium morphology of the graphene nanoribbon takes the form as shown in Figure 3.10a. The graphene portion far away from the Si nanowire conforms to the flat surface of the SiO_2 substrate while the middle portion of the graphene partially wraps around the Si nanowire. The geometry of the graphene-nanowire-substrate system at the equilibrium can be characterized by three

parameters: the width of the corrugated portion of the graphene nanoribbon *L*, the width of the graphene nanoribbon *W*, and nanowire diameter *d* (Figure 3.10a).

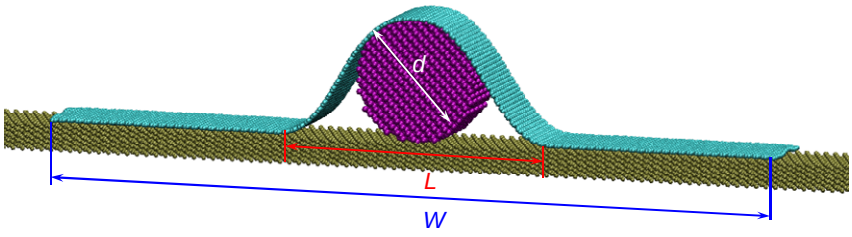

(a)

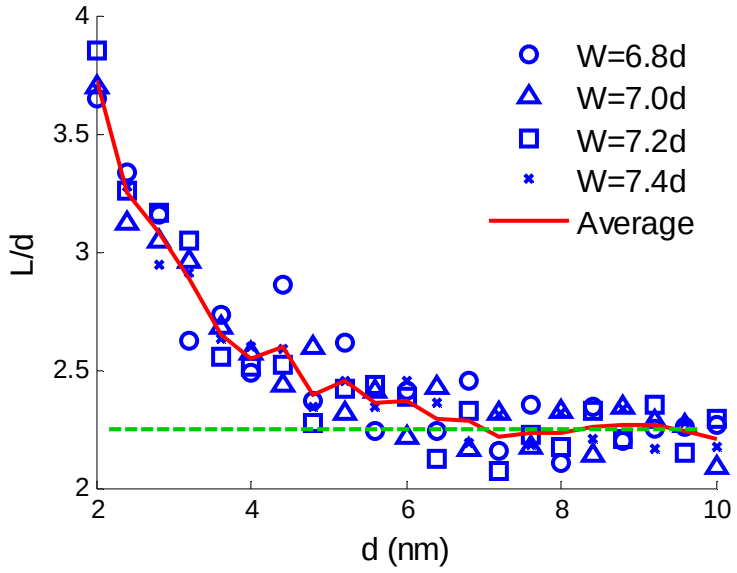

(b)

Figure 3.10. (a) Molecular mechanics simulation result of the morphology of a wide graphene nanoribbon intercalated by a Si nanowire on a SiO_2 substrate. Here d = 6 nm and W = 40 nm. (b) Normalized width of the corrugated portion of the graphene L/d as a function of d for various widths of the graphene nanoribbon W = 6.8d, 7.0d, 7.2d and 7.4d, respectively. The solid line plots the average of the four data sets. The dash line shows the plateau value of L/d when d is sufficiently large.

Figure 3.10b plots *L/d* as a function of *d* for various widths of graphene nanoribbon *W/d* = 6.8, 7.0, 7.2 and 7.4, respectively. When the graphene nanoribbon is sufficiently wide (e.g., much larger than *d*), *L* is roughly independent of *W*, as evident with the small variation among the results for the four different values of *W*. As shown in Figure 3.10b, *L/d* decreases as *d* increases, and then approaches to a plateau of about 2.2 when *d* exceeds 7 nm. Such a trend can be explained by the similar argument aforementioned. If the Si nanowire is too thin, the graphene nanoribbon can only barely wrap around the nanowire, given the significant constraint of possible strain energy increase in the graphene. The corrugated portion of the graphene ribbon gradually transits to the flat portion on the substrate surface, resulting in a relatively large *L/d* (e.g., 3.7 for *d* = 2 nm). If the Si nanowire is thick enough, the graphene nanoribbon can wrap more of the nanowire surface, leading to a higher slope of the graphene sagging down toward the substrate surface, and thus a smaller *L/d.* As the nanowire diameter is greater than ~7 nm, *L/d* tends to a constant of ~2.2. In other words, the morphology of the corrugated portion of the graphene nanoribbon intercalated by a sufficiently thick nanowire is self-similar.

Figure 3.11 further plots the Brenner potential energy of the carbon atoms in the graphene nanoribbon at the equilibrium state (e.g., Figure 3.10a), which depicts the strain energy profile of the corrugated graphene. As indicated by the color shades, high strain energy states in the graphene nanoribbon occur at the regions near the top of the nanowire and where the graphene becomes flat on the substrate. At such regions the graphene nanoribbon bends the most. The inset of Figure 3.11 further shows the average C-C bond lengths in *x*-direction at three locations, as indicated by

three marked lines A (where graphene remains flat on the substrate), B (in the middle of the intercalated portion of the graphene) and C (the crest of the corrugated graphene portion). Given the equilibrium C-C bond length of 1.42 Å, it is evident that the C-C bonds are stretched at B in *x*-direction and un-stretched at A and C. Since the Brenner potential energy of the carbon atoms at B is at the same level of that of carbon atoms at A, it can be estimated that the strain energy of the corrugated graphene nanoribbon is mainly due to bending, rather than stretching.

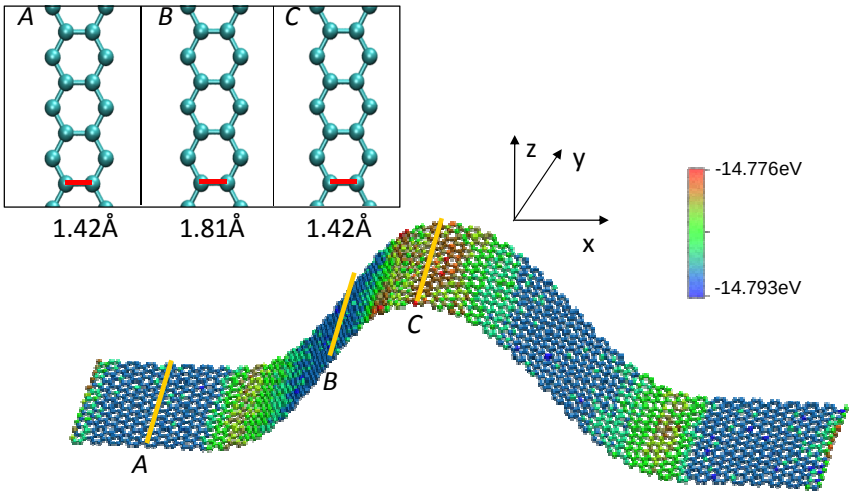

Figure 3.11. The distribution of Brenner potential energy of the carbon atoms in a graphene nanoribbon intercalated by a Si nanowire (not shown) on a SiO_2 substrate (not shown). The inset shows the C-C bond lengths in *x*-direction at three cross-sections marked by the solid lines on graphene, indicating the graphene is under tension near location B. Here d = 4 nm and W = 20 nm.

Case 2: Morphologic interaction between a blanket graphene flake and an array of Si nanowires evenly patterned in parallel on a SiO_2 substrate

When a blanket graphene flake is intercalated by an array of Si nanowires evenly patterned in parallel on a SiO_2 substrate, the nanowire spacing W comes into play in determining the regulated morphology of the graphene flake. Emerging from the simulations are two types of morphologies of graphene at equilibrium, depending on W and d, as shown in Figure 3.12.

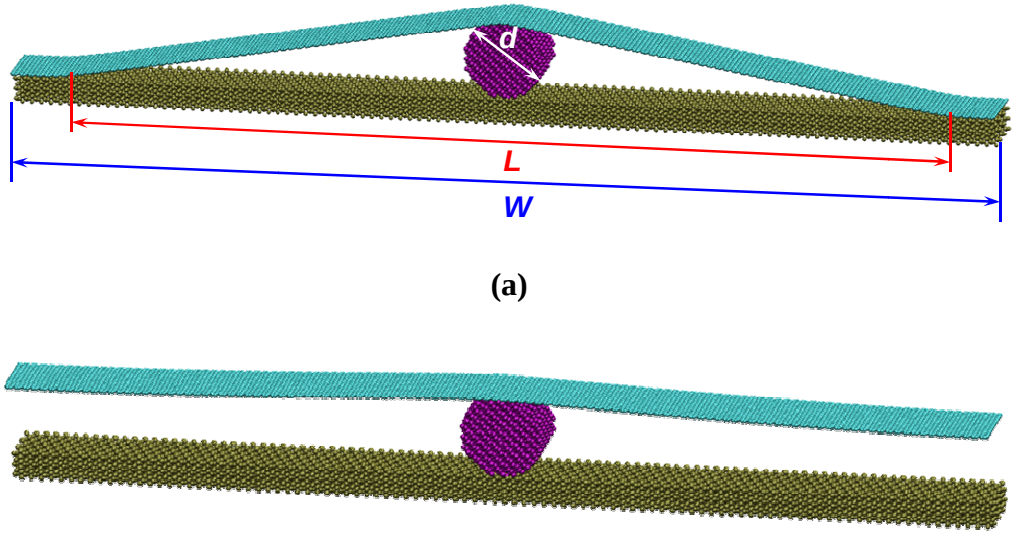

Figure 3.12. Molecular simulation results of the morphology of a blanket graphene flake intercalated by Si nanowires evenly patterned in parallel on a SiO_2 substrate. (a) When the Si nanowires are widely spaced (e.g., W is large), graphene sags in between neighboring nanowires and adhere to the substrate surface. The width of the corrugated portion of the graphene is denoted by L. (b) If the nanowire spacing is small, graphene remains nearly flat, just slightly conform to the envelope of the nanowires. Here d = 4 nm and W = 48 nm in (a) and 46 nm in (b). The sharp transition between (a) and (b) as W varies indicates a snap-through instability of the graphene morphology.

If the nanowires are widely spaced (e.g., $W>>d$), the graphene tends to wrap around each individual nanowire (Figure 3.12a), sags down and adheres to the substrate in between neighboring nanowires. The corrugated portion of the graphene is of a width of L and an amplitude of A_g ($\approx d$ in this case). Figure 3.13a further plots L/d as a function of d for various values of W. For a given W, L/d increases as d increases in a roughly linear manner.

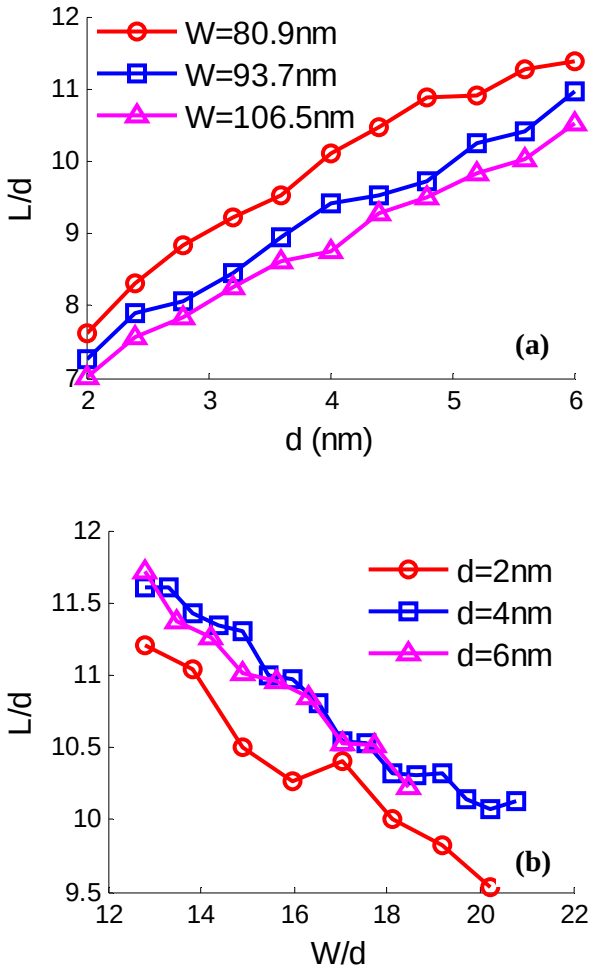

Figure 3.13. (a) L/d as a function of d for various values of W. (b) L/d as a function of W/d for various values of d.

When compared with the case of graphene nanoribbon intercalated by a single nanowire on a substrate (e.g., Figure 3.10b), the width of the corrugated portion of the graphene intercalated by patterned nanowires on a substrate is much larger. This can be explained by the constraint of the portion of the graphene sagged in between neighboring nanowires and adhered to the substrate. Therefore, the graphene cannot slide easily on the substrate to wrap around each individual nanowire closely. As a result, the corrugated portion of the graphene is under modest stretch in *x*-direction. By contrast, the graphene nanoribbon intercalated by a single nanowire is shown to be able to slide on the substrate surface to wrap around more of the nanowire surface. As a result, the stretch in the graphene in *x*-direction can be nearly fully relaxed (e.g., Figure 3.11), leading to a much smaller value of L/d. Figure 3.13a also indicates the increase of L/d as W decreases, for a given value of d. To further clarify this trend, Figure 3.13b plots L/d as a function of W/d for various values of d, which indicates a roughly linear dependence between L and W, as well as a weak dependence on d. This can be explained that, when nanowire spacing is larger, the corrugation-induced graphene stretching is accommodated by a longer graphene segment, leading to smaller strain energy of the graphene. Therefore the graphene wraps more around nanowires. The limiting case of infinitely large nanowire spacing corresponds to that of graphene intercalated by a single nanowire (e.g., Figure 3.10).

If the spacing between the patterned nanowires is not sufficiently large, the graphene flake remains nearly flat, just slightly conforming to the envelop of the nanowires with a negligible amplitude A_g (Figure 3.12b), a morphology of graphene distinct from that regulated by widely distributed nanowires on a substrate (i.e., Figure 3.12a).

For a given nanowire diameter d, there is a sharp transition between these two distinct morphologies as the nanowire spacing reaches a critical value W_{cr}. This result agrees with the snap-through instability of the graphene morphology regulated by patterned nanowires on a substrate predicted by our previous continuum model results. Such a snap-through instability of the graphene morphology results from the double-well energy profile of the system. For the bonding parameters given in Table 3.1, W_{cr}/d ranges from 12.3 to 12.8, and is approximately independent of d. In practice, it is possible to have chemical bonding or pinnings between the graphene and the substrate, the nanowire surface can also be functionalized to facilitate chemical bonding with the graphene, both of which lead to an enhanced interfacial bonding energy of the graphene. Based on the energetic interplay as described in Section 2.2, it is expected that the resulting graphene morphology can also be tuned by the interfacial bonding energy.

To investigate the effect of graphene-substrate interfacial bonding energy on the graphene morphology, a tuning factor λ is used to vary the bonding energy in the LJ pair potential describing the graphene-substrate van der Waals interaction. A tuning factor $\lambda>1$ denotes a graphene-substrate interaction energy stronger than that described in Table 3.1. Here, the graphene-nanowire interaction energy remains the same. Figure 3.14 plots the normalized amplitude of graphene corrugation A_g/d as a function of tuning factor λ for d = 4 nm, 4.2 nm and 4.4 nm, respectively. Here, W=46.9 nm. For a given nanowire diameter and spacing, there exists a critical graphene-substrate interaction energy (i.e., a critical tuning factor λ_c), weaker than which the graphene only slightly conform to the envelope of the nanowires (e.g., A_g/d

<<1), and stronger than which the graphene can sag in between the nanowires and adhere to the substrate (e.g., $A_g/d \approx 1$). The sharp transition between these two distinct morphologies at the critical graphene-substrate interfacial energy reveals the similar snap-through instability of the graphene morphology aforementioned. Previous studies based on continuum model suggest that $W/d \propto \lambda_c^{1/4}$, or $W\lambda_c^{1/4}/d$ is a constant. The results shown in Figure 2.14 give $W\lambda_c^{1/4}/d$ =12.40, 12.25, and 12.26 for d = 4 nm, 4.2 nm, and 4.4 nm, respectively. In this sense, the molecular mechanics simulation results agree well with the continuum model prediction.

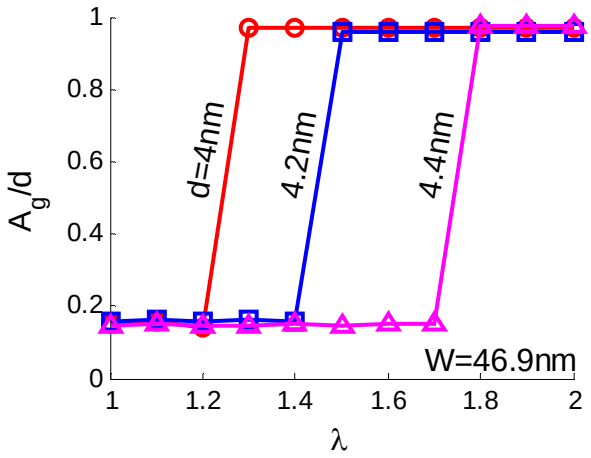

Figure 3.14. A_g/d as a function of tuning factor λ for various values of d. Here, W=46.9 nm. The sudden jumps of A_g/d at a critical value of λ indicate the snap-through instability of the graphene morphology shown in Figure 3.12.

3.3.3. Concluding remarks

Using molecular mechanics simulations, we determine the morphologic interaction between a graphene nanoribbon and a Si nanowire on a SiO_2 substrate, and that between a blanket graphene flake and an array of Si nanowires evenly patterned in

parallel on a SiO_2 substrate. The regulated graphene morphology is shown to be determined by the interplay between the graphene strain energy due to bending and stretching and the graphene-substrate and graphene-nanowire interaction energies. Specifically, the graphene morphology can be tuned by both geometric parameters (e.g., graphene nanoribbon width, nanowire diameter, and nanowire spacing) and material properties (e.g., graphene-nanowire and graphene-substrate bonding strength). Various simulations are conducted to quantify the relation between the graphene morphology and these parameters and properties.

The molecular mechanics simulation results agree well with our previous continuum mechanics modeling results, and furthermore, provide atomistic scale information of each carbon atoms in the graphene. Such information can be consequently used to determine the effect of the morphologic interaction and the mechanical deformation on the electronic properties of the graphene (e.g., bandgap). Though much remains to be done to achieve fine tuning of graphene's electronic properties via morphologic interaction, the present study demonstrates the beginning steps toward this promising approach that could potentially enable new graphene-based device applications.

3.4. Summary and Discussions

In this Chapter, we study the graphene morphology regulated by nanowires on a substrate surface, using continuum mechanics approach and molecular mechanics simulation. The equilibrium graphene morphology is dependent on both geometric parameters and interaction properties. The snap-through instability is found in the results of both continuum mechanics modeling and molecular mechanics simulations.

Results from the present study offer guidelines in nanostructural design to achieve desired graphene morphology via regulation with a resolution approaching the atomic feature size of graphene.

In the present models, we consider graphene morphology regulated by rigid nanowires (e.g., SiO_2 or Si) patterned on a rigid substrate (e.g., SiO_2). The graphene corrugation induced deformation in the nanowires and the substrate is expected to be negligible. Recent experimental progress enables transfer printing graphene onto a wide variety of substrate surfaces (e.g., polymers or elastomers). The graphene-substrate interaction may result in appreciable deformation of the underlying compliant polymer or elastomer substrate. To extend the results from the present study to such a case, the strain energy of the substrate needs to be considered in the energy minimization.

Chapter 4: Morphology of Few-layer Graphene Regulated by Patterned Surface of a Compliant Substrate

In this Chapter, we present an analytic model to explicitly determine the morphology of few-layer graphene regulated by a compliant substrate with surface grooves (Section 4.1). We reveal the effects of substrate stiffness, graphene-substrate adhesion and number of graphene layers on the regulated graphene morphology (Section 4.2). Depending on the number of graphene layers, substrate stiffness and graphene/substrate adhesion, graphene exhibits two types of morphology: I) graphene remains bonded to the substrate and corrugates to an amplitude up to that of the substrate surface grooves; II) graphene debonds from the substrate and remains flat on top of the substrate surface grooves. The sharp transition between these two types of graphene morphology can be potentially used to determine the adhesion between graphene and elastic materials, a crucial property that remains challenging to measure.

4.1. Introduction and Model Description

The existing analytic and computational models to determine the morphology of substrate-supported graphene on substrate surface (Chapter 2) are mainly based on two assumptions. First, the substrate is assumed to be rigid and thus does not deform when interacting with the graphene. Second, only mono-layer graphene is considered. Results from these existing models shed important light on the substrate-regulated graphene morphology; however, the two assumptions limit the general applicability

of these models. In reality, it is much easier to fabricate few-layer graphene than mono-layer graphene, and thus few-layer graphene is more commonly used in applications such as graphene-reinforced nanocomposites. Transfer printing technique also allows for transferring graphene from a mother wafer onto a wide range of substrate materials, such as polymers and elastomers [77, 78]. The morphology of few-layer graphene regulated by a compliant substrate depicts rather rich characteristics that cannot be readily captured by the existing models.

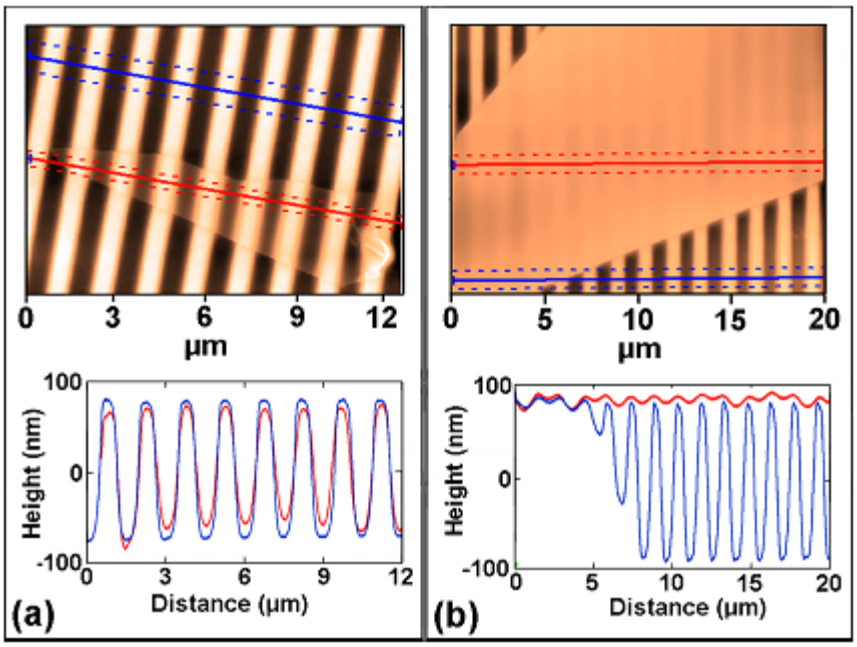

Figure 4.1. Image (top) and height measurements (bottom) for a. 8-layer and b. 13-layer graphene. Red lines show trajectories of scans over graphene, corresponding to red height curves (averaged between the dotted lines). Blue lines show scans of surrounding PDMS substrate [78].

For example, recent experiments show that an 8-layer graphene on a compliant polydimethylsiloxane (PDMS) substrate can closely conform to the sinusoidal surface

grooves of the PDMS [78]. By contrast, a 13-layer graphene remains nearly flat on the grooved substrate surface (Figure 4.1).

To overcome the limitations of existing models, we explicitly determine the morphology of few-layer graphene regulated by the patterned surface of a compliant substrate. Figure 4.2 illustrates the typical transfer printing process of graphene from a mother wafer to a compliant substrate with patterned surface and possible resulting structures. An *n*-layer graphene ($n \geq 1$) fabricated on a stiff and smooth mother wafer (e.g., silica for mechanically exfoliated graphene or copper for chemically grown graphene) is brought in contact with a compliant substrate (e.g., polymer or elastomer) with patterned surface, pressure is then applied to guarantee the full contact between the graphene and the substrate (e.g., the patterned surface is flattened under pressure). Upon release of the pressure, the mother wafer is lifted from the compliant substrate. If the graphene adheres more strongly to the compliant substrate than to the mother wafer, the graphene is left on the compliant substrate.

The resulting morphology of the graphene on the patterned surface of the compliant substrate is dictated by the competition between the graphene-substrate adhesion energy and the strain energy in the graphene-substrate laminate. The regulated graphene morphology can be categorized into two types:

Type I: If the graphene-substrate adhesion energy (denoted as Γ_{gs}) is strong, the graphene remains bonded to the compliant substrate at the price of increased strain energy due to the corrugation of the graphene (denoted as E_g) and the distortion of the substrate near the portion underneath the graphene (denoted as E_s) (e.g., Figures

4.2b-d). The amplitude of the graphene corrugation can be determined through minimizing the total free energy (i.e., $E_g+E_s-\Gamma_{gs}$), as illustrated in Figure 4.2e;

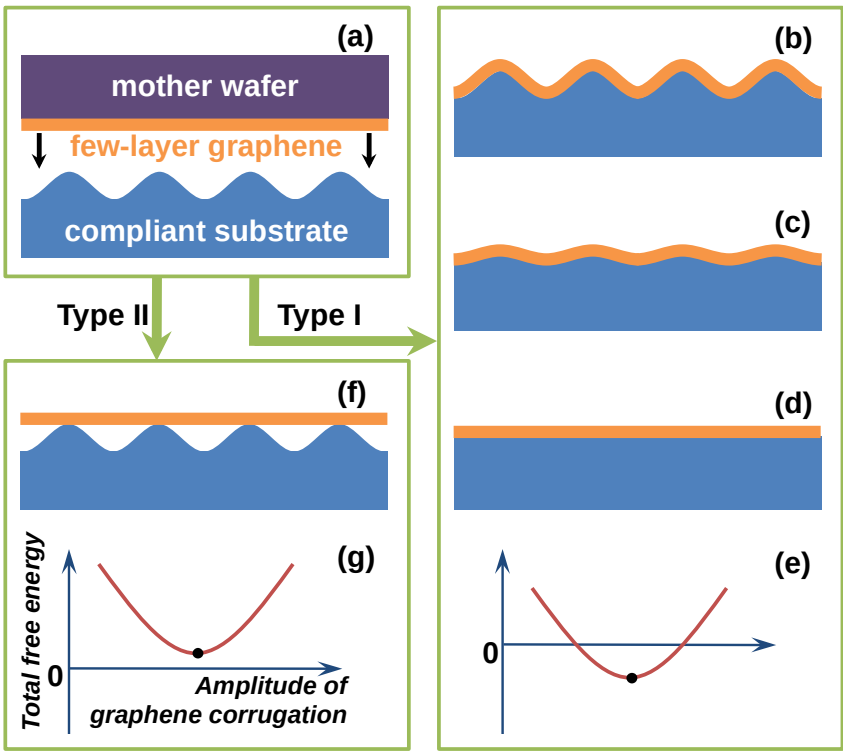

Figure 4.2. (a) Schematic of the transfer printing of a few-layer graphene from a flat and stiff mother wafer onto a compliant substrate with sinusoidal surface grooves. The resulting graphene morphology can be categorized into two types. Type I: If the graphene-substrate adhesion is sufficiently strong, graphene remains bonded to the compliant substrate and corrugates to an amplitude up to that of the substrate surface grooves (b-d). The graphene amplitude depends on the substrate stiffness and the number of graphene layers. Type II: If the graphene-substrate adhesion is weak, graphene debonds from the substrate and remains flat on top of the substrate surface grooves (f). (e) and (g) schematically plot the total free energy, $E_g+E_s-\Gamma_{gs}$, as a function of the amplitude of graphene corrugation in Type I and Type II, respectively.

Type II: If the graphene-substrate adhesion energy is weak and cannot balance the aforementioned strain energy of the graphene-substrate laminate (i.e., $E_g+E_s > \Gamma_{gs}$, Figure 4.2g), the graphene-substrate interface debonds. As a result, the graphene remains nearly flat on the top of the patterned substrate surface while the substrate surface recovers to its original pattern (Figure 4.2f). In such a case, the strain energy of the graphene-substrate laminate is negligible.

After the transfer printing process, the strain energy of the Type I corrugated graphene consists of the contributions from bending and stretching of the graphene. While the bending energy of the graphene is determined by its out-of-the-plane deflection, the membrane energy of the graphene depends on both its in-plane displacement and out-of-plane deflection. In reality, relative sliding between the graphene and the underlying substrate may occur during transfer printing, which can mitigate the in-plane stretching of the graphene. Such relative sliding depends on the graphene-substrate friction and detailed transfer printing conditions, which is often difficult to quantify. To overcome such an uncertainty, here we consider the following two limiting cases.

In one limiting case, we assume there is no relative sliding, i.e., the graphene deforms from a flat profile to a sinusoidal wavy profile by purely deflecting out of the plane while the in-plane displacement of the graphene is zero. Assuming the profiles of the patterned substrate surface and the Type I corrugated graphene morphology in *x*-*y* plane to be $w_s(x,y)$ and $w_g(x,y)$, respectively, the bending energy of the graphene is given by

$$E_g^b = \iint \frac{D}{2}\left[\left(\frac{\partial^2 w_g}{\partial^2 x} + \frac{\partial^2 w_g}{\partial^2 y}\right)^2 + 2(1-\nu)\left(\left(\frac{\partial^2 w_g}{\partial x \partial y}\right)^2 - \frac{\partial^2 w_g}{\partial^2 x}\frac{\partial^2 w_g}{\partial^2 y}\right)\right] dxdy, \quad (4.1)$$

where D is the bending rigidity and ν the Poisson's ratio of the graphene, respectively.

The in-plane strain of the graphene in such a limiting case results from the out-of-plane deflection and the strain components are given by

$$\varepsilon_{xx} = \frac{1}{2}\left(\frac{\partial w_g}{\partial x}\right)^2, \varepsilon_{yy} = \frac{1}{2}\left(\frac{\partial w_g}{\partial y}\right)^2 \text{ and } \varepsilon_{xy} = \frac{1}{2}\frac{\partial w_g}{\partial x}\frac{\partial w_g}{\partial y}. \quad (4.2)$$

Therefore the membrane energy of the graphene is given by

$$E_g^m = \iint \frac{C}{2}\left[\left(\varepsilon_{xx} + \varepsilon_{yy}\right)^2 + 2(1-\nu)\left(\varepsilon_{xy}^2 - \varepsilon_{xx}\varepsilon_{yy}\right)\right] dxdy \quad (4.3)$$

where C is the in-plane elastic modulus of the graphene. The total strain energy of the graphene is thus given by

$$E_g = E_g^b + E_g^m \quad (4.4)$$

In another limiting case, the graphene is allowed to slide freely on the substrate surface so that the stretching in the graphene can be fully relaxed. In other words, the strain energy of the graphene results solely from its bending, that is,

$$E_g = E_g^b \quad (4.5)$$

Assuming the distortion deformation of the compliant substrate underneath the graphene is elastic, the resulting strain energy of the substrate is equivalent to the

work done by the graphene-substrate interfacial traction $p(x,y)$ over the distortion displacement of the substrate surface $(w_s - w_g)$. That is,

$$E_s = \iint \frac{1}{2} p(w_s - w_g) dx dy \tag{4.6}$$

The total strain energy, $E_g + E_s$, obtained from the above formulation can then be compared with the graphene-substrate adhesion energy, Γ_{gs}, to determine the resulting graphene morphology. For example, for a given substrate material and its surface profile, $E_g + E_s$ is computed over a certain range of graphene corrugation amplitude (e.g., from zero to the amplitude of the substrate surface pattern). If $(E_g + E_s)_{min} < \Gamma_{gs}$, the graphene remains bonded with the substrate and corrugate with an amplitude corresponding to $(E_g + E_s)_{min}$ (i.e., Type I, Figure 4.2e). If $(E_g + E_s)_{min} > \Gamma_{gs}$, the graphene debonds from the substrate and remains flat on the substrate grooves (i.e., Type II, Figure 4.2g).

4.2. Results and Discussions

We next apply the above analytic model formulation to determine the morphology of *n*-layer graphene regulated by a compliant substrate patterned with sinusoidal surface grooves. The profiles of the surface grooves and the resulting Type I graphene morphology are described by $w_s = A_s \cos(2\pi x/\lambda)$ and $w_g = A_g \cos(2\pi x/\lambda)$, respectively, where A_s and A_g are the amplitude of the grooves and the graphene corrugation, respectively, and λ the wavelength. Substituting w_g into Equations (4.1)-(4.3) gives that, for the limiting case of no relative sliding of the graphene, the average strain energy of the graphene over one groove period is

$$E_g = \frac{1}{\lambda}\int_0^{\lambda}\left[\frac{D}{2}\left(\frac{\partial^2 w_g}{\partial^2 x}\right)^2 + \frac{C}{8}\left(\frac{\partial w_g}{\partial x}\right)^4\right]dx = \frac{4\pi^4 D A_g^2}{\lambda^4} + \frac{3\pi^4 C A_g^4}{4\lambda^4}, \quad (4.7)$$

where the first term on the right side denotes the contribution from the bending energy and the second the contribution from the membrane energy; and thus for the limiting case of graphene freely sliding on the substrate surface, the average strain energy of the graphene over one groove period is

$$E_g = \frac{4\pi^4 D A_g^2}{\lambda^4}, \quad (4.8)$$

The distortion deformation of the elastic substrate surface underneath the graphene $(A_s - A_g)\cos(kx)$ results in a graphene-substrate interfacial traction $p = (\pi\tilde{Y}_s/\lambda)(A_s - A_g)\cos(kx)$, where $\tilde{Y}_s$ is the plane strain Young's Modulus of the substrate material [71, 96, 97]. Thus, the average strain energy of the substrate over one groove period is given by

$$E_s = \frac{\pi\tilde{Y}_s}{4\lambda}(A_s - A_g)^2, \quad (4.8)$$

To benchmark the above formulation, we take $\Gamma_{gs} = 0.1\,J/m^2$ (representative of graphene-polymer adhesion), $\lambda = 1.5\,\mu m$ and $A_s = 100\,nm$ (comparable to recent experiments [78]). For an *n*-layer graphene, its bending rigidity *D* is taken to be $(3.8n^3 - 3.6n^2) \times 10^{-18}\,Nm$ [98], and its in-plane elastic modulus $C = 340n\,N/m$ [23]. Figure 4.3 plots the normalized graphene amplitude A_g/A_s as a function of the substrate plane strain Young's modulus $\tilde{Y}_s$ for various numbers of graphene layers *n* =1, 10 and 35, respectively. For the limiting case of no graphene sliding on the substrate (Figure 4.3a), if the substrate is very compliant (e.g., $\tilde{Y}_s \leq 1MPa$), the

graphene remains bonded to the substrate and assumes a rather flat morphology (e.g., Type I, $A_g/A_s \ll 1$). In other words, the substrate surface grooves underneath the graphene are nearly flattened. As the substrate becomes stiffer, the graphene becomes more corrugated (increasing A_g).

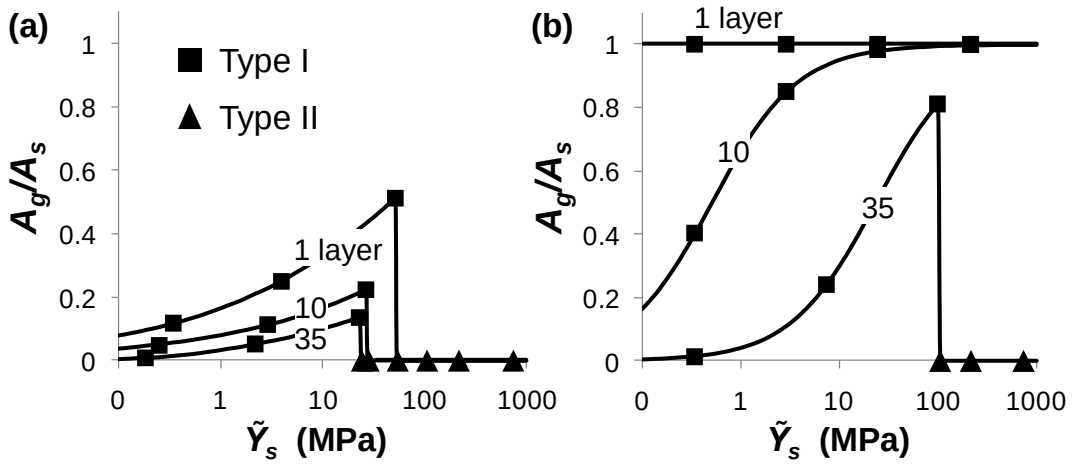

Figure 4.3. The normalized graphene amplitude A_g/A_s as a function of $\tilde{Y}_s$ for n =1, 10 and 35, respectively, for (a) the limiting case of no graphene sliding on the substrate and (b) the limiting case of graphene freely sliding on the substrate. Note the sharp transition between Type I (square marks) and Type II (triangle marks) graphene morphology at certain combinations of $\tilde{Y}_s$ and n.

For a given substrate stiffness, the thicker the graphene layers (higher bending rigidity), the less the graphene is corrugated. For a given n, however, there exists a critical substrate stiffness, higher than which the graphene debonds from the substrate and remains flat on the substrate surface grooves (e.g., Type II, $A_g/A_s = 0$). The transition from Type I to Type II graphene morphology is sharp. The critical substrate stiffness decreases as n increases. For the limiting case of the graphene freely sliding on the substrate (Figure 4.3b), a monolayer graphene completely conforms to the

surface grooves of a substrate of any stiffness ($A_g/A_s = 1$), a few-layer graphene (e.g., n = 10) corrugates slightly on a rather compliant substrate but conforms closely to the surface of a sufficiently stiff substrate. However, the morphology of a thick graphene layer can sharply switch between Type I and Type II at a critical substrate stiffness (e.g., at $\tilde{Y}_s \approx 100MPa$ for n = 35).

Figure 4.4 further plots A_g/A_s as a function of n for $\tilde{Y}_s = 1MPa, 10\ MPa$ and $1GPa$, respectively. For the limiting case of no graphene sliding on the substrate (Figure 4.4a), if the substrate is compliant (e.g., $\tilde{Y}_s = 1MPa$ or $10MPa$), the graphene remains bonded to the substrate and assumes a slightly corrugated morphology (e.g., Type I). For a given $\tilde{Y}_s$, A_g decreases as n increases. On a sufficiently stiff substrate (e.g., $\tilde{Y}_s = 1GPa$), graphene with any number of layers debonds from the substrate and remains flat (Type II). For the limiting case of the graphene freely sliding on the substrate (Figure 4.4b), if the substrate is compliant (e.g., $\tilde{Y}_s = 1MPa$ or $10MPa$), graphene remains bonded to the substrate and A_g decreases gradually as n increases (Type I). If the substrate is sufficiently stiff (e.g., $\tilde{Y}_s = 1GPa$), a thinner graphene (n $\leq$ 32) remains bonded and fully conformed to the substrate (Type I) while a thicker graphene ($n \geq 33$) debonds from the substrate and remains flat (Type II). Such a sharp transition in graphene morphology is similar to the snap-through instability of graphene morphology on a corrugated substrate predicted by models and observed in experiments [78, 99].

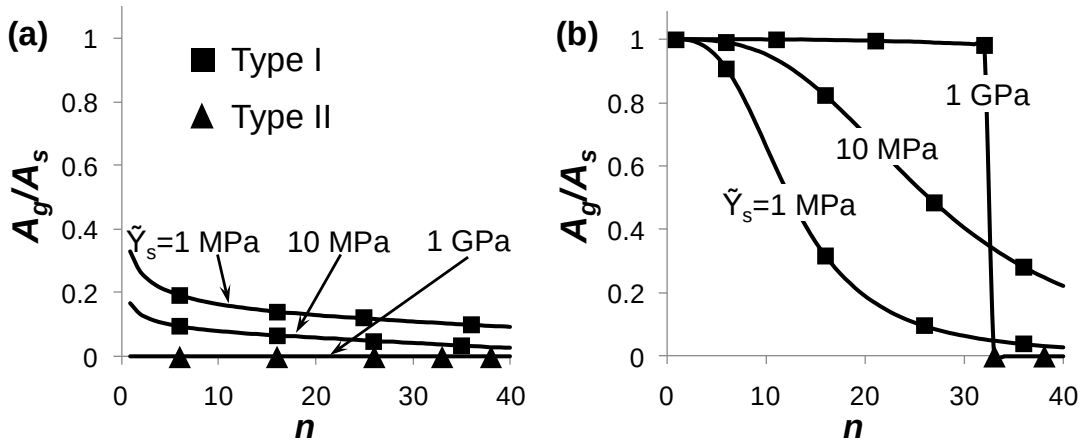

Figure 4.4. The normalized graphene amplitude A_g/A_s as a function of *n* for $\tilde{Y}_s = 1$ MPa, 10 MPa and 1 GPa, respectively, for (a) the limiting case of no graphene sliding on the substrate and (b) the limiting case of graphene freely sliding on the substrate. Note the sharp transition between Type I (square marks) and Type II (triangle marks) graphene morphology at certain combinations of $\tilde{Y}_s$ and *n*.

The sharp transition between Type I and Type II graphene morphologies shed light on characterizing the graphene-substrate adhesive properties. As an illustration, Figure 4.5 maps the minimum strain energy of the graphene-substrate laminate, $(E_g+E_s)_{min}$, in the space of $\tilde{Y}_s$ and *n*, for the limiting cases of no graphene sliding (Figure 4.5a) and graphene sliding freely (Figure 4.5b) on the substrate surface. If, for a given $\tilde{Y}_s$, a critical number of graphene layers n_{cr} can be determined from experiments at which the graphene morphology switches between Type I and Type II, the energy levels corresponding to (n_{cr}, $\tilde{Y}_s$) in Figures 4.5a and 4.5b define the upper and lower bounds of the graphene-substrate adhesion energy Γ_{gs}. For example, taking n_{cr} = 13, $\tilde{Y}_s = 1.6MPa$, Figure 4.5 gives Γ_{gs} ranging from 3.5 mJ/m^2 to 7.4 mJ/m^2, which agrees

reasonably well with the experimental results on graphene-PDMS adhesion (~7.1 mJ/m^2) [78].

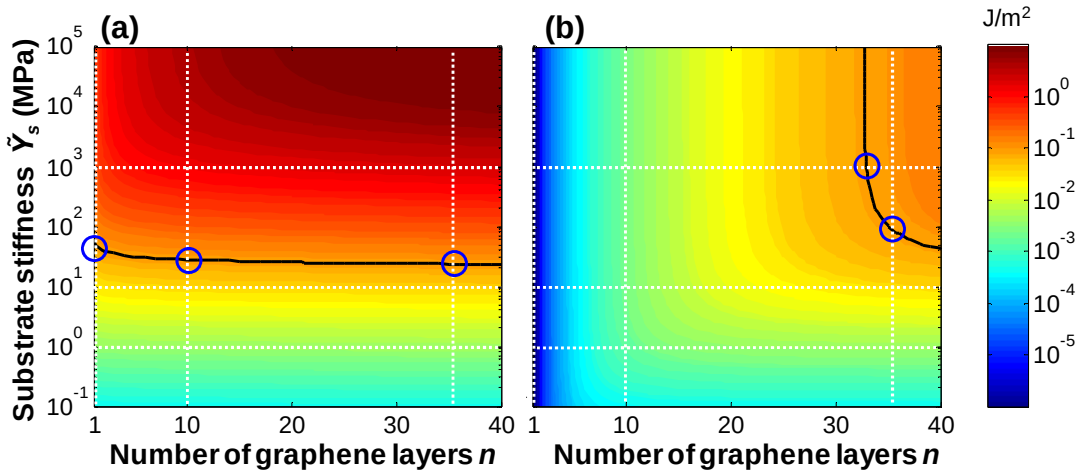

Figure 4.5. The map of $(E_g+E_s)_{min}$ in the space of $\tilde{Y}_s$ and n for the limiting cases of (a) no graphene sliding and (b) graphene freely sliding on the substrate, respectively. The energy levels in (a) and (b) corresponding to a combination of $\tilde{Y}_s$ and n at which graphene morphology switches between Type I and Type II define the upper and lower estimates of the graphene-substrate adhesion energy Γ_{gs}. The solid contour line denotes $\Gamma_{gs} = 0.1\, J/m^2$, which defines a boundary below which the graphene assumes Type I morphology and above which it assumes Type II morphology. The three vertical dotted lines in (a) and those in (b) correspond to the cases in Figures 4.3a and b, respectively. The three horizontal dotted lines in (a) and those in (b) correspond to the cases in Figures 4.4a and b, respectively. The intersections of the dotted lines and the solid lines (circles) indicate the sharp transitions between Type I and Type II in Figures 3 and 4.

On the other hand, for a given Γ_{gs}, the corresponding contour line in the energy map defines a boundary below which the graphene assumes Type I morphology and above which it assumes Type II morphology. For example, the solid contour line of

$\Gamma_{gs} = 0.1\, J/m^2$ in Figure 4.5a intersects the dotted lines of n = 1, 10, and 35, defining a critical substrate stiffness for each n that corresponds to the sharp transition between Type I and Type II morphology revealed in Figure 4.3a. Similarly, the solid contour line in Figure 4.5b intersects the dotted line of n = 35 and that of $\tilde{Y}_s = 1GPa$, defining a critical substrate stiffness and a critical number of graphene layer that correspond to the sharp morphologic transition revealed in Figures 4.3b and 4.4b, respectively. While Figure 4.5 is specifically applicable to the case of few-layer graphene on a compliant substrate with sinusoidal surface grooves, similar energy maps for few-layer graphene morphology regulated by other patterned substrate surfaces can be readily obtained following the formulation of the generalized analytic model delineated in Section 4.1.

4.3. Summary

In summary, we show that strong correlation exists between the adhesion property of graphene and its morphology regulated by the patterned surface of a compliant substrate. We delineate an analytic model to quantitatively determine the regulated morphology of the graphene. Two distinct types of graphene morphology emerge from the results: Type I) graphene remains bonded to the substrate and corrugates to an amplitude up to that of the substrate surface patterns; Type II) graphene debonds from the substrate and remains flat on top of the substrate surface patterns. The sharp transition between these two types of graphene morphology can potentially open up a feasible pathway to characterizing the adhesion between graphene and various elastic materials, a property that is rather challenging to measure directly.

Chapter 5: Carbon Nanotube Initiated Formation of Carbon Nanoscrolls and its Application as Ultrafast Nano-oscillators

In this Chapter, we demonstrate the spontaneous formation of a carbon nanoscroll (CNS) from graphene on a substrate, initiated by a carbon nanotube (CNT) and an ultra-fast oscillator based on the resulting nano-structure. Using molecular dynamics simulations, we show that the interaction energy between the CNT and graphene sheet can help the system overcome the initial energy barrier to achieve an overlap (Section 5.1). The rolling of graphene into a CNS is modulated by the CNT size, the carbon-carbon interlayer adhesion, and the graphene-substrate interaction. The resulting nano-structure is a CNS with the CNT housed inside. The CNT inside the CNS can oscillate along axial direction at a natural frequency of 10s gigahertz (GHz) (Section 5.2). We demonstrate an effective strategy to reduce the dissipation of the CNS-based nano-oscillator by covalently bridging the carbon layers in the CNS. We further demonstrate that, such a CNS-based nano-oscillator can be excited and driven by an external AC electric field, and oscillate at more than 100 GHz.

5.1. Carbon Nanotube Initiated Scrolling of Graphene

5.1.1. Existing approaches to fabricating CNSs

The scrolling of graphene into a CNS has been demonstrated by both experiments and simulations. After intercalated by alkali metals (e.g., potassium), high-purity graphite could be exfoliated in ethanol (EtOH) solvents (Figure 5.1) [55]. Upon sonication, the

exfoliated graphite sheets curl onto themselves, forming carbon nanoscrolls. Using TEM analysis, it was revealed that these nanoscrolls have an interlayer spacing of 3.4 Å and no end caps.

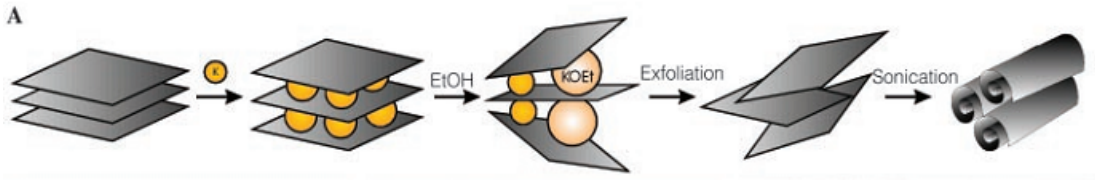

Figure 5.1. Schematic of the intercalation/exfoliation process. Graphite is intercalated with potassium metal and then exfoliated with ethanol (EtOH) to form a dispersion of carbon sheets. Sonication produces carbon nanoscrolls [55].

The scrolling process of graphene was *in situ* observed when a single layer graphene on SiO_2/Si substrate rolled up into CNSs spontaneously when the chip with graphene was immersed in isopropyl alcohol (IPA) solution (Figure 5.2) [62].

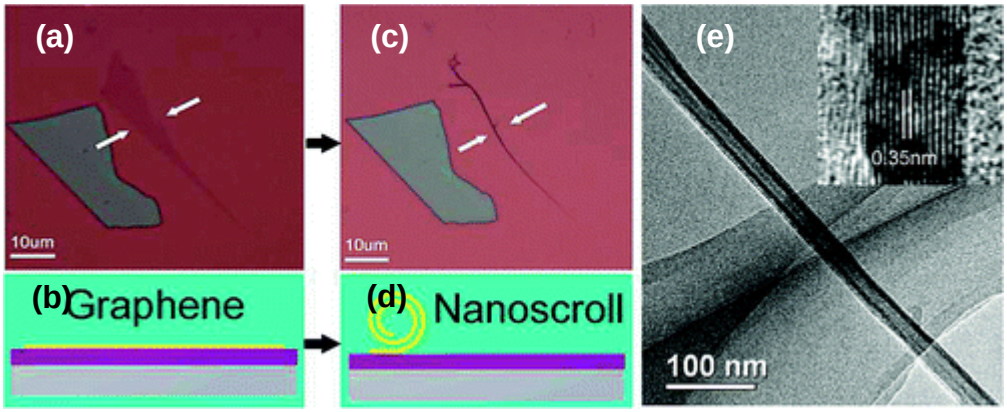

Figure 5.2. Optical microscope images and schematics of the original (a) (b) and scrolled (c) (d) graphene monolayer on the SiO_2 substrate, respectively.(e) TEM image of a fabricated CNS. The inset is a higher magnification image of part of the CNS, showing that the distance between adjacent graphene layers is about 0.35 nm [62].

The authors claimed that the surface strain and the perturbations in the IPA solution environment are the assistant forces to roll up graphene. The formation of CNSs is also highly sensitive to the concentration of IPA solution and the shape of the graphene. TEM studies revealed that the resulting CNS has a tube-like structure with a hollow core surrounded by graphene walls 0.35 nm apart (Figure 5.2e). The unique structure of CNS is confirmed by the difference in the Raman spectra between graphene, CNS, and MWCNT.

Recent molecular dynamics simulations demonstrated that water nanodroplets could activate and guide the folding of planar graphene nanostructures [63]. If water nanodroplets are deposited at one end of graphene nanoribbons with selected droplet size and ribbon width, they could help graphene overcome deformation barriers and roll into CNS (Figure 5.3). The ribbon tip first folds around the spherical droplet (Figures 5.3a and 5.3b). Once a overlap forms (Figure 5.3c), the droplet guided rolling continues (Figure 5.3d) until reaching the other end of ribbon (Figure 5.3e).

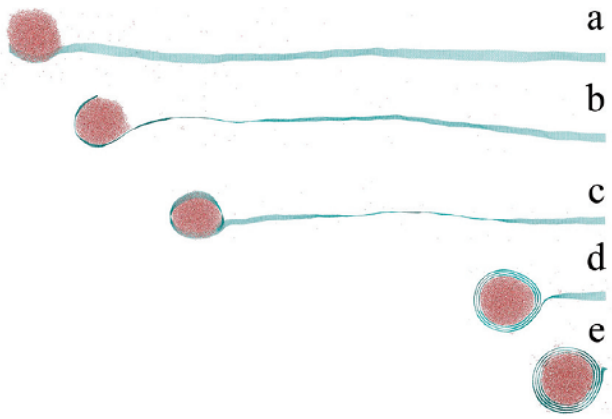

Figure 5.3. Folding and rolling of a graphene ribbon. (a, b) The ribbon tip folds around the water droplet into a wrapped cylinder, and (c-e) the wrapped cylinder is induced to roll on the ribbon surface (c-e) [63].

5.1.2. An all-dry physical approach to fabricating CNSs

The existing chemical approaches to fabricating CNS may lead to possible contamination of chemical residue and the simulation demonstrations are rather challenging to be realized in experiments. Aiming to address these issues in existing approaches, we use MD simulations to demonstrate an all-dry physical approach to fabricating CNSs, in which the rolling of a substrate-supported graphene monolayer is initiated by a CNT. Figure 5.4 depicts the molecular dynamics simulation model, in which a CNT is placed along the left edge of a flat rectangular graphene monolayer supported by a SiO_2 substrate.

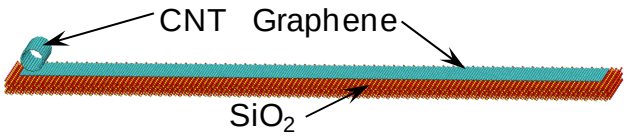

Figure 5.4. The MD simulation model. A graphene is supported by a SiO_2 substrate, with a CNT placed along the left edge of the graphene.

The CNT-initiated formation of a CNS from the substrate-supported graphene is governed by the interplay among the following energies: the CNT-graphene interaction energy E_{tg}, the graphene-graphene interlayer interaction energy E_{gg} (once graphene starts to roll into a CNS), the graphene strain energy E_g, and the graphene-substrate interaction energy E_{gs}. The non-bonded CNT-graphene interaction and graphene-graphene interlayer interaction can be characterized by vdW force. The weak interaction between a mechanically exfoliated graphene and its substrate can also be characterized by vdW force. Due to the nature of vdW interaction, E_{tg} and E_{gg}

minimize when the carbon-carbon (C-C) interlayer distance reaches an equilibrium value, so does E_{gs} when the distance between the graphene and the substrate surface reaches its equilibrium. When the graphene separates from the substrate, curls up to wrap the CNT, and later starts to roll into a CNS, E_{tg} and E_{gg} decrease; on the other hand, E_{gs} increases, so does E_g due to the mechanical deformation of the graphene associated with the wrapping and rolling. Above said, E_{tg} and E_{gg} serve as the driving force, while E_{gs} and E_g represent the resistant force in the CNT-initiated formation of a CNS from a substrate-supported graphene.

In the simulations, the C-C bonds in the CNT and graphene are described by the second generation Brenner potential [92]. The non-bonded CNT-graphene interaction and graphene-graphene interlayer interaction are described by a Lennard-Jones pair potential $V_{CC}(r) = 4\lambda_{CC}\varepsilon_{CC}(\sigma_{CC}^{12}/r^{12} - \sigma_{CC}^{6}/r^{6})$, where $\varepsilon_{CC} = 0.00284\text{eV}$, $\sigma_{CC} = 0.34\text{nm}$ and λ_{CC} is a tuning factor that is used to vary the C-C interaction energy to study its effect on the CNS formation [100]. It has been shown that the effective C-C interaction energy in a CNS can be tuned by an applied dc/ac electric field [101, 102]. The non-bonded graphene-SiO_2 substrate interaction is described by a Si-C pair potential and an O-C pair potential, both of which take the same form of $V_{CC}(r)$ but with different parameters, that is, $\varepsilon_{SiC} = 0.00213\text{eV}$, $\sigma_{SiC} = 0.15\text{nm}$, $\varepsilon_{OC} = 0.00499$ eV and $\sigma_{OC} = 0.23$ nm, respectively [93]. The tuning factor for the graphene-substrate interaction λ_{CS} is taken to be the same for both Si-C and O-C pair potentials. To reduce the computation size, all atoms in the SiO_2 substrate are fixed during simulation. This assumption is justified by the weak graphene-substrate

interaction and the rigidity of bulk SiO_2. The graphene used in the simulations is 50 nm long and 4 nm wide, with the right edge constrained on the substrate by a linear spring. CNTs with length of 4 nm but various diameters are used to study the effect of CNT size on the CNS formation. The MD simulations are carried out using LAMMPS [103] with NVT ensemble at temperature 300K and with time step 1 fs.

Depending on the CNT size, C-C interaction strength and C-SiO_2 interaction strength, the CNT-graphene-substrate system shown in Figure 5.4 evolves in three different modes. Figure 5.5 illustrates the time sequential snapshots of each mode of evolution and the corresponding variation in the total potential energy of the system. In the three cases shown in Figure 5.5, $\lambda_{CC} = 1$ and $\lambda_{CS} = 1$. CNTs of various diameters (i.e., (10,10), (12,12) and (18,18)) are used, respectively.

Mode I: CNT gliding on graphene. The graphene strain energy E_g due to wrapping a CNT is roughly inversely proportional to the square of the CNT diameter. If the CNT diameter is too small, the significant increase of E_g and the corresponding increase of E_{gs} due to graphene-substrate separation can overbalance the decrease of E_{tg} due to graphene wrapping the CNT. As a result, instead of wrapping the CNT, the graphene remains flat on the substrate, while the CNT glides on the graphene driven by the thermal fluctuation, as shown in Figure 5.5b-e. The translational motion of the CNT on the graphene is expected to cause negligible variation to the total potential energy of the system except the thermal fluctuation, which is evident in Figure 5.5a.

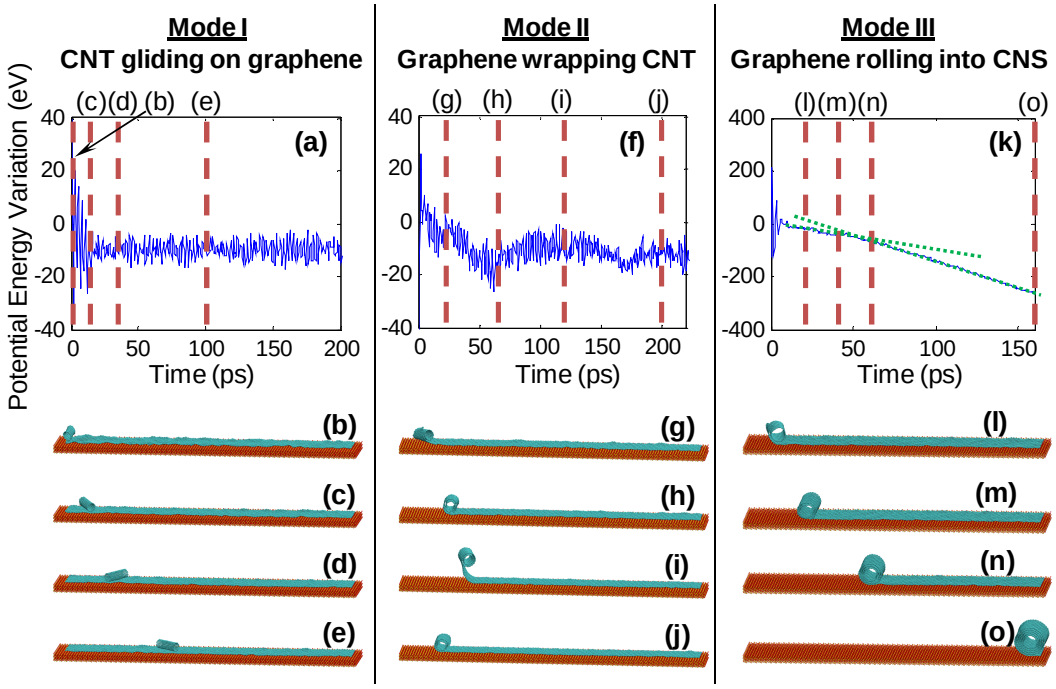

Figure 5.5. Three modes of evolution of the CNT-graphene-substrate system. (a, f, k) plot the variation in the total potential energy of the system as a function of simulation time for each mode, respectively; (b-e): Snapshots of a (10, 10) CNT gliding on the substrate-supported graphene at 0 ps, 15 ps, 40 ps and 100 ps, respectively; (g-j): Snapshots of the graphene wrapping a (12, 12) CNT at 20 ps, 65 ps, 120 ps and 200 ps, respectively; (l-o): Snapshots of the graphene rolling into a CNS, initiated by a (18,18) CNT, at 20 ps, 45 ps, 60 ps and 160 ps, respectively. The two dotted fitting curves in (k) show that the graphene further rolling into a CNS (from (n) to (o)) leads to more substantial decrease of potential energy than that due to graphene wrapping CNT (from (l) to (m)). In all three cases shown here, $\lambda_{CC} = 1$ and $\lambda_{CS} = 1$.

Mode II. Graphene wrapping CNT. If a CNT of intermediate diameter is used, the increase of E_g due to graphene bending and E_{gs} due to graphene-substrate separation can be outweighed by the corresponding decrease of E_{tg}. Consequently, graphene can separate from the substrate under thermal fluctuation and start to wrap around the

CNT (Figure 5.5g). The total potential energy continues decreasing until the whole surface of the CNT is nearly wrapped by the graphene (Figure 5.5h). Further rolling of the graphene is hindered by a local energy barrier due to the step formed by the left edge of the graphene adhering to the CNT. If the CNT radius is not sufficiently large, the energy barrier due to the graphene edge step can be too high and thus prevent the further rolling of graphene. This is analogous to a roller moving toward a speed bump of a fixed height. If the roller is too thin, instead of passing the bump, it can be bounced up in the air. As shown in Figure 5.5h-i, the graphene-wrapped CNT rolls toward the graphene edge step, and is then bounced upward. The kinetic energy of the graphene-wrapped CNT leads to further separation of a short segment of graphene from the substrate, and then the graphene-substrate interaction pulls the separated graphene re-adhered back to the substrate. Such two processes repeat several times and the graphene segment eventually re-adheres back to the substrate after the excess translational kinetic energy is dissipated. The CNT remains wrapped by the graphene (Figure 5.5j).

Mode III. Graphene rolling into a CNS. If the diameter of the CNT is sufficiently large, the translational kinetic energy of the graphene-wrapped CNT can overcome the fixed energy barrier due to the graphene edge step. As a result, CNT-initiated rolling of the graphene continues and then an overlap between the left edge and the flat portion of the graphene forms. Such an overlap leads to the decrease of E_{gg}, which drives further rolling of graphene into a CNS (Figure 5.5l-o). As shown in Figure 5.5k, the continuous rolling of the graphene results in further decrease of the overall potential energy, which is more substantial than that due to the graphene

wrapping the CNT. The resulting CNS is energetically stable against thermal perturbations at 300 K.

When the CNT size and C-SiO_2 interaction strength are fixed, the evolution of the CNT-graphene-substrate system can be modulated by the C-C interaction strength. Figure 5.6a defines a phase diagram of the evolution of the CNT-graphene-substrate system in the space of C-C interaction strength and CNT size, for a given C-SiO_2 interaction strength (i.e., $\lambda_{CS} = 1$). The same three modes of evolution as described above are observed.

For a given CNT size, the mode of evolution changes from CNT gliding to graphene wrapping and then to graphene forming a CNS, as the C-C interaction becomes stronger. For a given C-C interaction strength, the similar change of the mode of evolution is shown as the CNT size increases. Emerging from the simulations are a boundary between mode I and mode II and that between mode II and mode III, the latter of which can serve as a guidance for controlling CNS formation by varying C-C interaction and selecting CNT size. Figure 5.6b plots the case of $\lambda_{CS} = 4$. When the C-SiO_2 interaction strength increases, a stronger C-C interaction is needed for the CNS formation, for a given CNT size; similarly, a CNT with larger diameter is needed to initiate the CNS formation, for a given C-C interaction strength. For the case of $\lambda_{CS} = 4$, there exists a critical value of λ_{CC}, below which graphene rolling into a CNS cannot be initiated by a CNT of any given size.

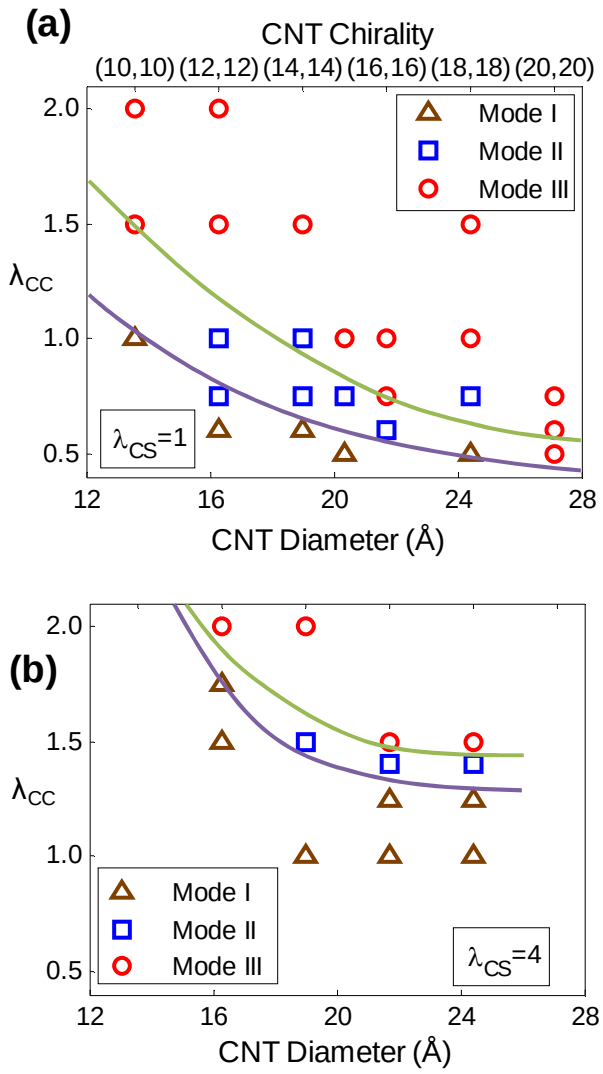

Figure 5.6. Phase diagrams of the evolution of the CNT-graphene-substrate system in the space of C-C interaction strength and CNT size, for a given C-SiO_2 interaction strength. Here, (a) $\lambda_{CS}=1$, (b) $\lambda_{CS}=4$.

5.2. Ultrafast Nano-oscillators based on Interlayer-bridged Carbon Nanoscrolls

Axial nano-oscillators based on multi-walled CNTs (MWCNTs) have been proposed previously [104, 105]. In the proposed MWCNT-based axial nano-oscillator, the ends

of the outer tubes of a MWCNT are opened. When the inner tubes are displaced from their original position along the axial direction and then released, the restoring force from the outer tubes pulls the inner ones back. Due to the ultralow friction between the carbon layers, the inner tubes can oscillate along its axial direction, and the natural frequency of the oscillation is estimated to be on the order of GHz [105-108]. Figure 5.7a illustrates a double-walled CNT (DWCNT)-based axial nano-oscillator.

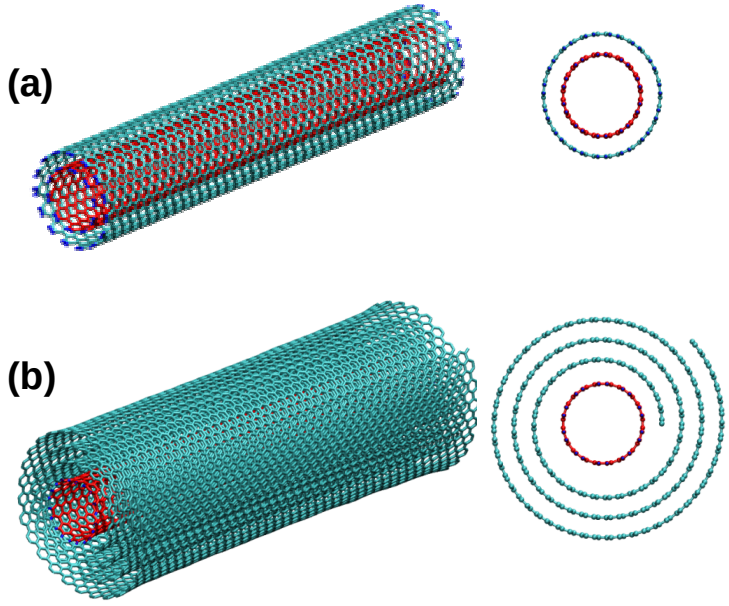

Figure 5.7. Perspective view (left) and end view (right) of (a) a DWCNT and (b) a CNS with a SWCNT housed inside. When displaced from its equilibrium position along axial direction, the inner tube (red) can oscillate inside the outer tube (cyan) or CNS (cyan), at GHz frequency.

Enthusiasm for MWCNT-based axial nano-oscillators aside, the realization of such promising nano-devices hinges upon feasible fabrication techniques. For example, well-controlled opening of the ends of the outer tubes of a MWCNT and chemical

treatment of the inner tubes in a MWCNT (e.g., doping or polarization) still remain as significant challenges. As a result, successful fabrication of MWCNT-based axial nano-oscillators has not yet been demonstrated, let alone the exploration of exciting the axial oscillation of such nano-oscillators via external interferences [109-111].

It has been demonstrated in Section 5.1 that a CNT of suitable diameter can initiate the scrolling of a monolayer graphene on a substrate into a CNS. The CNT near the edge of the graphene can help overcome the initial energy barrier for the scrolling of graphene. Once the scrolling is initiated, the graphene can spontaneously roll up into a CNS. The resulting CNS-CNT nanostructure has the two ends of the CNS naturally open and a CNT housed inside the CNS (e.g., Figure 5.7b). Similar scrolling of a graphene oxide layer initiated by a MWCNT has been experimentally demonstrated recently [112]. As to be detailed later, when the CNT is displaced partially out of the CNS along the axial direction, the van der Waals force acting on the two ends of the CNT is not balanced and the resultant force on the CNT serves as the restoring force to pull the CNT back into the CNS. Given the ultralow CNT-CNS friction similar to the inter-tube friction in a MWCNT, the CNT in the CNS is shown to be able to oscillate at a frequency of 10s GHz. In this Section, we use molecular dynamics simulations to perform systematic investigation of the characteristics of the ultrafast oscillation of the abovementioned CNS-based axial nano-oscillators. We propose a feasible strategy to significantly reduce the energy dissipation of the CNS-based nano-oscillators. We further demonstrate that the CNS-based nano-oscillators can be excited by an external AC electrical field and oscillate at a frequency more than 100 GHz. A distinct advantage of the CNS-based nano-oscillators against the MWCNT-

based ones is as follows. The CNT and the basal graphene are fabricated separately before the scrolling process. For example, the CNT and the graphene can be treated differently and thus possess different features, such as defects, chirality and polarization. These features make it possible to significantly enhance the performance of the CNS-based axial nano-oscillators, as to be detailed later in this paper. With the ever-maturing fabrication technique of high quality graphene, CNS-based axial nano-oscillators hold promise to become a viable approach to achieving nanoscale GHz mechanical oscillators. In particular, the excitation of CNS-based nano-oscillators under external interferences demonstrates their great potential as nanoelectromechanical systems (NEMS) for nanoscale energy transduction (e.g., from electrical and/or magnetic to mechanical), harvesting and storage (e.g., as mechanical oscillation).

5.2.1.CNS-CNT nanostructure formation

The CNS-based axial nano-oscillator depicted in Figure 5.7b was formed using a 10 nm long (10, 10) single-walled CNT (SWCNT) to initiate the scrolling of a 10 nm by 30 nm graphene along its long (armchair) edge. The formation of the CNS/CNT nanostructure is similar to that described in Section 5.1. As shown in Figure 5.8a, the graphene is supported by a SiO_2 substrate, with a (10, 10) single wall CNT placed along the left edge of the graphene. The substrate is 34 nm long, 14 nm wide and 1 nm thick. In the MD simulations, the C–C bonds in the CNT and CNS are described by the second generation Brenner potential [92], which allows for C-C covalent bond forming and breaking. The non-bonded C-C interaction is described by a Lennard–Jones pair potential [100]. The graphene-substrate interaction is considered in the

same way as in Section 5.1. The MD simulations are carried out using LAMMPS [103] with Canonical Ensemble at 500 K and with time step 1 fs.

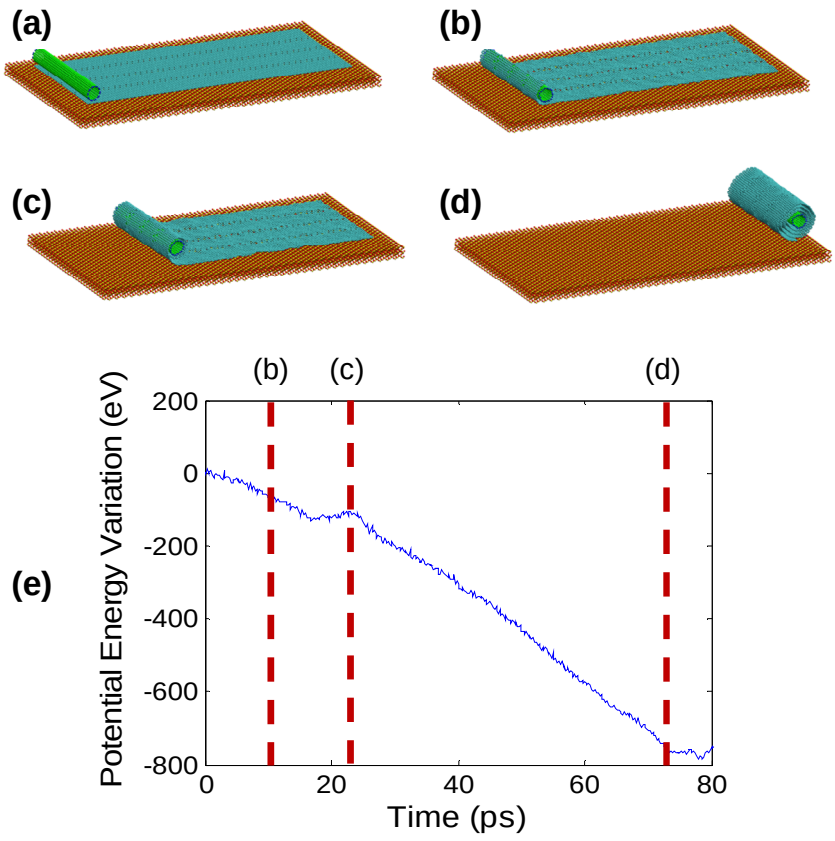

Figure 5.8. (a - d) Snapshots of the graphene scrolling into a CNS, initiated by a (10, 10) SWCNT, before equilibration, at 10 ps, 22 ps, and 76 ps, respectively. (e) The variation in the total potential energy of the system as a function of simulation time.

Initiated by the CNT, the graphene first separates from the substrate and curls up to wrap the CNT (Figure 5.8b). Once the overlap between the left edge and the flat portion of the graphene forms (Figure 5.8c), graphene starts to scroll continuously into a CNS (Figure 5.8d) with the CNT housed inside. Figure 5.8e shows the decrease of the total potential energy due to the graphene wrapping the CNT and further scrolling into a CNS. Our simulations show that there is no appreciable difference

between the scrolling of a pristine graphene (without any defects) and that of a graphene with defects. For example, the graphene shown in Figure 5.8 has patterned vacancies along three parallel lines, the effect of which is to be detailed later.

5.2.2. Oscillation of a CNT housed inside a naturally formed CNS

The CNS-based nano-oscillator formed by scrolling up a pristine graphene is first equilibrated for 50 ps at 100 K, and then the CNT housed inside is assigned a velocity 2.5 Å/ps along its axial direction to initiate the oscillation. In order to constrain the rigid body motion of the nano-oscillator, two rows of carbon atoms along the axial direction on the outermost shell of the CNS are fixed.

Figure 5.9(a) shows the snapshots of the axial oscillation of the CNS/CNT nanostructure at 5 ps, 15 ps, 20 ps, 30 ps, 40 ps and 50 ps, respectively. The simulations are carried out at 100K. The axial motion of the CNT is excluded in the calculation of temperature. Besides the oscillation of the CNT inside the CNS, the CNS itself also oscillates through inter-layer relative sliding in axial direction, initiated by the reaction force from the CNT (i.e., opposite to the restoring force applied on the CNT). The reaction force pulls the inner shells of the CNS to slide outward during the CNT oscillation, thus the CNS itself starts to oscillate accompanying the CNT motion. As a result, the oscillation of the CNS/CNT nanostructure is indeed the coupled CNT oscillation and that of the CNS itself. It needs to be pointed out that the CNS self-oscillation is not only driven by the van der Waals-type reaction force between the CNS and the CNT but also affected by the in-plane shear rigidity of the basal graphene. The different energetic interplays for the

CNT oscillation and the CNS self-oscillation lead to a rather irregular coupled oscillation, similar to the axial oscillation observed in a MWCNT [113].

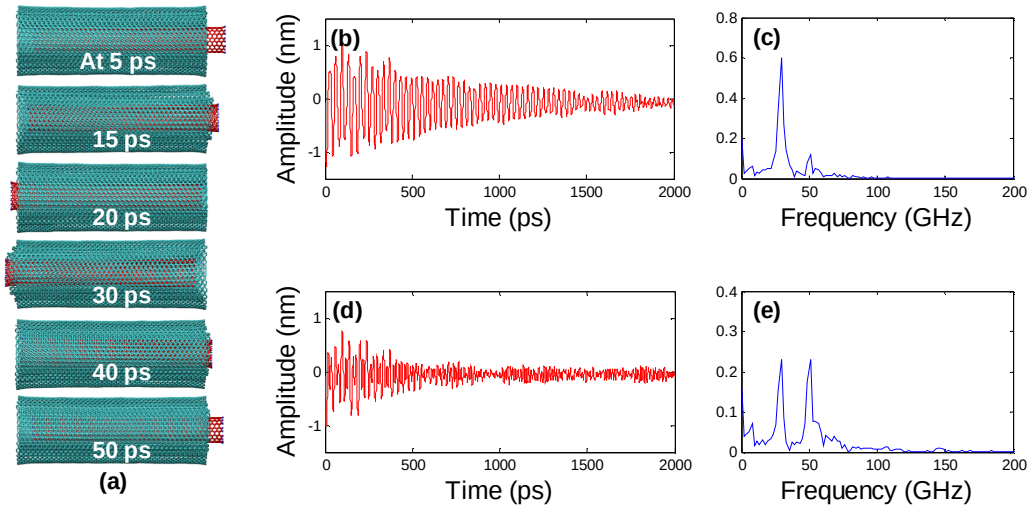

Figure 5.9. (a) Snapshots of the axial oscillation of the CNS-based nano-oscillator at 5 ps, 15 ps, 20 ps, 30 ps, 40 ps and 50 ps, respectively. Note the coupled axial oscillations of the CNT and the CNS itself. The evolution of (b) the absolute amplitude and (d) the relative amplitude of the CNT oscillation inside the CNS, as a function of simulation time, respectively. The Fast Fourier Transform (FFT) analysis of the absolute amplitude (c) and the relative amplitude (e) for the first 500 ps reveals a frequency of the oscillation of the CNT inside the CNS (29.4 GHz) and that of the oscillation of the CNS itself (50.9 GHz), respectively. The simulations are carried out at 100K.

To further decipher the coupled oscillation of the CNS/CNT nanostructure, we define two oscillation amplitudes: the absolute amplitude which is the axial distance from the left end of the CNT to the outermost atom at the left end of the CNS (which is fixed), and the relative amplitude which is the axial distance from the left end of the CNT to the innermost atom at the left end of the CNS (which moves as the CNS oscillates). Figures 5.9b and 5.9d plot the absolute and relative amplitudes as the

function of simulation time, respectively. While the absolute amplitude captures the oscillation of the CNT, the relative amplitude characterizes the coupled oscillation of the CNS/CNT nanostructure, which is more irregular and decays faster. Fast Fourier Transform (FFT) analysis is also performed for the first 500 ps of the oscillation. FFT of the absolute amplitude shows a peak at 29.4 GHz (Figure 5.9c), which represents the frequency of CNT oscillation. By contrast, FFT of the relative amplitude shows two peaks, 29.4 GHz and 50.9 GHz, respectively (Figure 5.9e). While the first peak corresponds to the frequency of CNT oscillation inside the CNS, the second peak reveals the frequency of the CNS self-oscillation. The higher frequency of the CNS self-oscillation results from the restoring force contributed by both the non-bonded van der Waals force among carbon layers and the covalent C-C bonding force in the basal graphene.

5.2.3. Oscillation of a CNT housed inside an interlayer-bridged CNS

While the ultrafast oscillation of the CNT inside the CNS at 10s GHz is encouraging, the quick dissipation and rather irregular behavior of the oscillation definitely limit the potential application of CNS-based nano-oscillators as NEMS devices. The quick dissipation and irregular oscillation result from the coupled oscillation, during which the kinetic energy of the CNT is continuously transduced into the self-oscillation of the CNS and then dissipates by the friction due to interlayer sliding. To address this issue, we next demonstrate a feasible and effective strategy to suppress the relative interlayer sliding in the CNS, which can lead to a much more sustainable ultrafast CNS-based nano-oscillator.

Both simulations and experiments have shown that, when a MWCNT is treated by ion irradiation, some carbon atoms can be knocked off, leaving vacancies in the tubes of the MWCNT [114]. Upon heating, the carbon atoms near the vacancies tend to form covalent bonds with other similar carbon atoms in a neighboring tube, driven by the reduction of high-energy dangling bonds of these carbon atoms. As a result, the tubes in the MWCNT are covalently bridged, leading to a significant increase of the inter-tube shear rigidity of the MWCNT. In other words, the relative inter-tube sliding in such a bridged MWCNT involves breaking the covalent C-C bridging bonds, thus is energetically unfavorable. The ion irradiation induced vacancies are also used to facilitate the bridging bond formation among SWCNTs to form CNT bundles [115, 116]. Inspired by these previous studies, next we demonstrate that vacancies can facilitate the formation of interlayer bridging bonds in a CNS, which in turn can effectively suppress the interlayer relative sliding in the CNS.

Instead of using a pristine graphene, we use graphene with patterned vacancies to form a CNS. The vacancies in the graphene are patterned along three parallel lines in the scrolling direction (Figure 5.10a) to facilitate bridging bond formation after scrolling. In reality, such vacancies can be introduced using focus ion beam to irradiate the graphene along those parallel lines. A SWCNT is used to initiate the scrolling of the aforementioned graphene with patterned vacancies. The carbon atoms at the two ends of the SWCNT are saturated by hydrogen atoms, so that no bridging bonds can be formed between the SWCNT and the CNS. After the scrolling process of the basal graphene with vacancies, the resulting CNS/CNT nanostructure is first heated up from 300 K to 1300 K in 100 ps, then maintained at 1300 K for 1600 ps,

and finally cooled down back to 300 K in 100 ps. As shown in Figure 5.10b, interlayer bridging bonds start to form after the temperature reaches 1000 K. The total number of interlayer bridging bonds in the CNS increases as the temperature further increases to and maintains at 1300 K, and gradually saturates. After cooled down to room temperature, the interlayer bridging bonds formed at high temperature remain in the CNS. Figure 5.10c depicts the end view of the bridged CNS after the heat treatment. Besides the interlayer bridging bonds inside the CNS, bridging bonds are also formed along the unsaturated edges of the CNS (i.e., at the two ends of the CNS and the two edges along its axial direction). No bridging bond is formed between the CNS and the SWCNT with saturated ends.

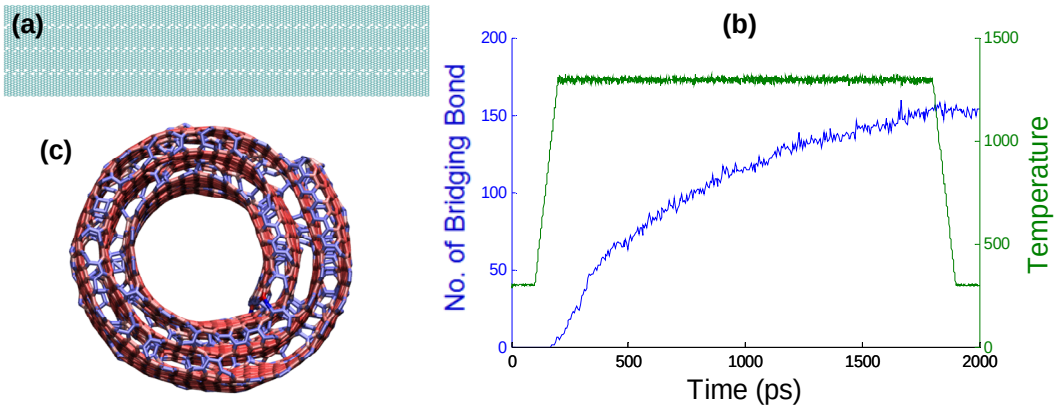

Figure 5.10. (a) The graphene with patterned vacancies. (b) The evolution of the number of interlayer bridging bond in the CNS and the temperature change as a function of time, respectively. Note that the bridging bonds remain after cooling down to room temperature. (c) The end view of the interlayer-bridged CNS after the heat treatment. The color shades represent potential energy level of the carbon atoms. Here the SWCNT housed inside the CNS is not shown for visual clarity.

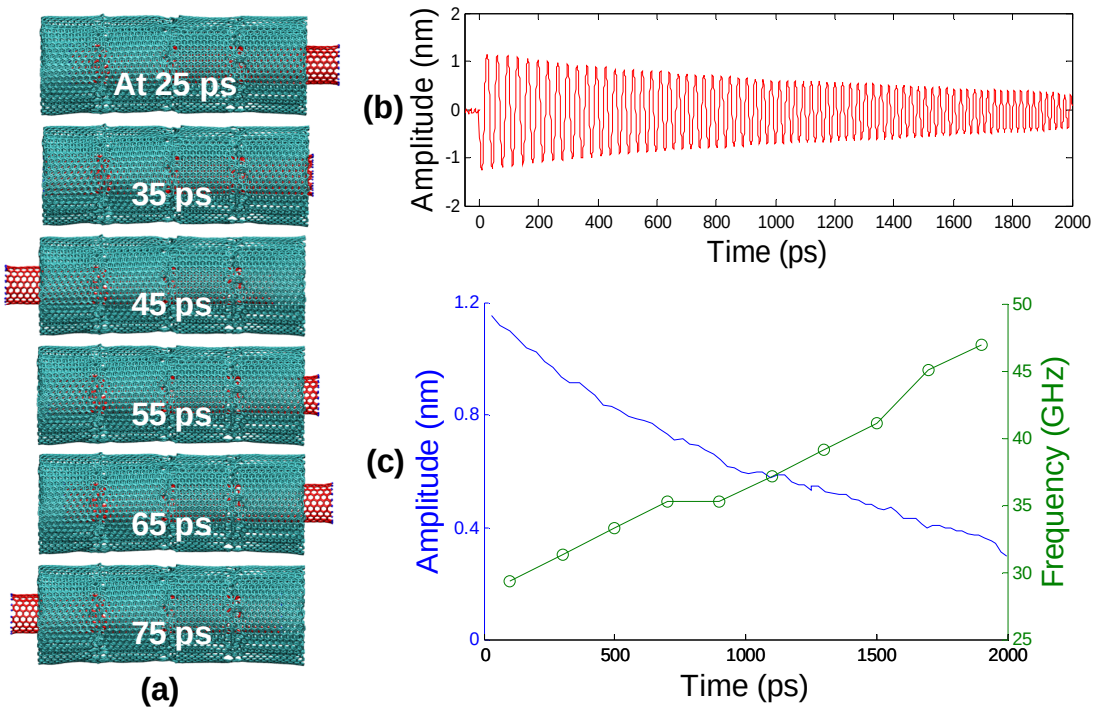

Figure 5.11. (a) Snapshots of the axial oscillation of the bridged-CNS-based nano-oscillator at 25 ps, 35 ps, 45 ps, 55 ps, 65 ps and 75 ps, respectively. Note the oscillation of the CNS itself is fully constrained by the interlayer bridging bonds. (b) The evolution of CNT oscillation amplitude. (c) The peak amplitude of each oscillation cycle and the corresponding oscillation frequency as a function of time, respectively. The simulations are carried out at 100K.

The oscillation of the SWCNT housed inside the interlayer-bridged CNS is then investigated following the similar procedure used for that of the SWCNT inside the un-bridged CNS. Figure 5.11a shows the snapshots of the axial oscillation of the interlayer-bridged CNS/CNT nanostructure at 25 ps, 35 ps, 45 ps, 55 ps, 65 ps and 75 ps, respectively. No appreciable relative sliding among the CNS layers is found during the oscillation of the CNT. In other words, the self-oscillation of the CNS is effectively suppressed by the interlayer bridging bonds. This is further confirmed by

the negligible difference between the absolute amplitude and relative amplitude of the CNT as defined above.

Figures 5.11b plots the absolute amplitude of CNT as a function of simulation time. Compared with the oscillation of the CNT inside an un-bridged CNS, the CNT oscillation inside an interlayer-bridged CNS is much more regular. Also evident in Figure 5.11b is the slower decay of the oscillation amplitude when compared with Figure 5.11b, which results from the suppression of energy dissipation due to interlayer relative sliding in the CNS. Figure 5.11c plots the peak amplitude of each oscillation cycle and the corresponding oscillation frequency obtained from FFT analysis as a function of simulation time, respectively. The initial frequency of the CNT oscillation is 29.4 GHz when the oscillation amplitude is about 1.15 nm, and the oscillation frequency at 2 ns is 47.0 GHz when the oscillation amplitude is about 0.30 nm. The oscillation frequency increases monotonically as the oscillation amplitude decreases over the time. Such a dependence of oscillation frequency on oscillation amplitude is consistent with the MWCNT-based axial oscillators as reported in earlier studies [117, 118].

We next compare the performance of bridged-CNS-based nano-oscillators with that of MWCNT-based nano-oscillators. Our studies show that, there is negligible difference in the oscillation behaviors between an MWCNT-based nano-oscillator and a DWCNT-based one, if the DWCNT is identical to the two innermost tubes of the MWCNT. Thus, here we report the simulation results of the oscillation behaviors of a (10, 10)/(15, 15) DWCNT, following the similar procedure aforementioned. In order to constrain the rigid body motion of the nano-oscillator, one ring of carbon

atoms in the middle of the outer tube of the DWCNT are fixed. The inner tube is assigned a velocity 2.5 Å/ps along its axial direction to initiate the oscillation.

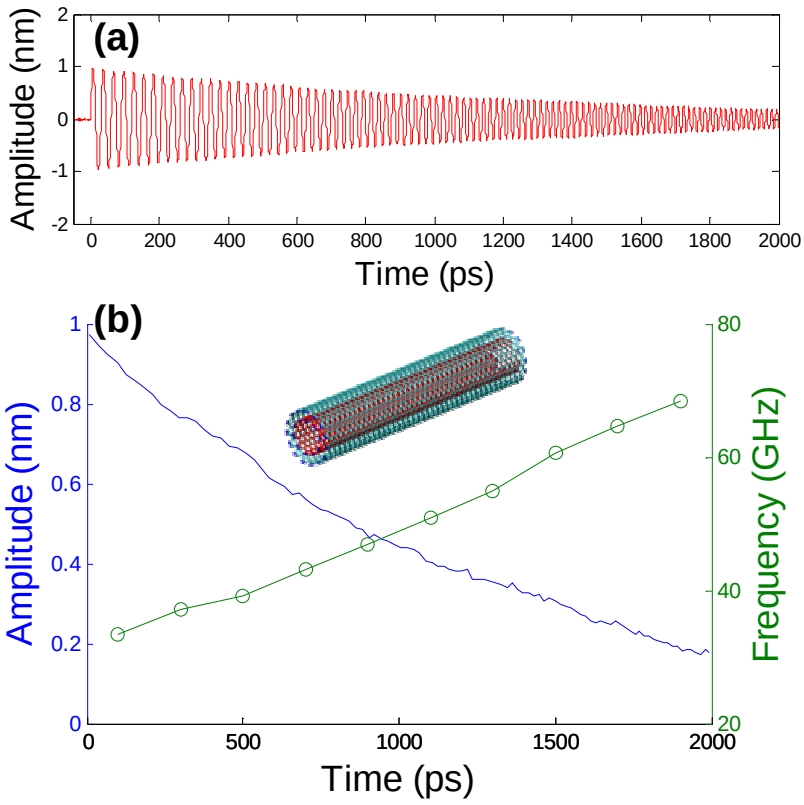

Figure 5.12. (a) The evolution of the oscillation amplitude of the inner tube of a (10, 10)/(15, 15) DWCNT. (b) The peak oscillation amplitude of each cycle and the corresponding oscillation frequency as a function of time, respectively. The simulations are carried out at 100K.

The oscillation amplitude, defined as the axial distance from the left end of the inner tube to the left end of the outer tube, is plotted as a function of simulation time in Figure 5.12a. The peak oscillation amplitude of each cycle and the corresponding oscillation frequency as a function of time are shown in Figure 5.12b. While the initial velocity of the inner tube is the same, the resulting initial oscillation amplitude

of the DWCNT-based nano-oscillator is slightly smaller than that of the bridged-CNS-based nano-oscillator. Such a difference results from the slight difference in the geometry between the outer tube of the DWCNT (a perfect tube) and the innermost layer of the bridged-CNS (a tube that is cut in axial direction and then slightly displaced radially), leading to a restoring force of the DWCNT-based nano-oscillator modestly larger than that of the bridged-CNS-based one. The difference in the restoring force also explains the relatively higher oscillation frequency of the DWCNT-based nano-oscillator than that of the bridged-CNS-based one for a given oscillation magnitude. Nonetheless, the comparison between Figure 5.11c and Figure 5.12b shows that, the bridged-CNS-based nano-oscillator has a modestly slower dissipation rate than the DWCNT-based nano-oscillator. For example, it takes about 1000 ps for the magnitude of DWCNT-based nano-oscillator to decay from 0.9 nm to 0.4 nm, while it takes 1300 ps for the bridged-CNS-based nano-oscillator. Earlier studies have shown that the translational energy in a DWCNT-based oscillator is mainly dissipated via a wavy deformation in the outer tube undergoing radial vibration [108]. In a bridged CNS, the constraint from the covalent interlayer bridging bonds can largely suppress the radial deformation of all layers in the CNS. In other words, the bridged CNS serves as a thick-walled tubular nanostructure with a much higher rigidity in both axial and radial directions than a MWCNT. As a result, the axial oscillation of the SWCNT housed inside the bridged CNS is more sustainable than that inside a MWCNT.

5.2.4. Effects of temperature and commensuration on the nano-oscillator performance

To understand the effect of temperature on the performance of the bridged-CNS-based nano-oscillator, Figure 5.13 compares the peak oscillation amplitude of each cycle and the corresponding oscillation frequency as a function of time for a bridged-CNS-based nano-oscillator and a DWCNT-based nano-oscillator at 300 K. For both nano-oscillators, the decay of the oscillation magnitude at 300K is modestly faster than that at 100K, while the corresponding oscillation frequency is slightly higher than that at 100K. At higher temperature, the thermal fluctuation of the carbon atoms in the nano-oscillators become more energetic, resulting in rougher surfaces of both the oscillating CNT and the carbon layers of the housing CNT or CNS and therefore increased interlayer friction. Nonetheless, the bridged-CNS-based nano-oscillators still have a modestly slower dissipation rate than the DWCNT-based nano-oscillator at an elevated temperature.

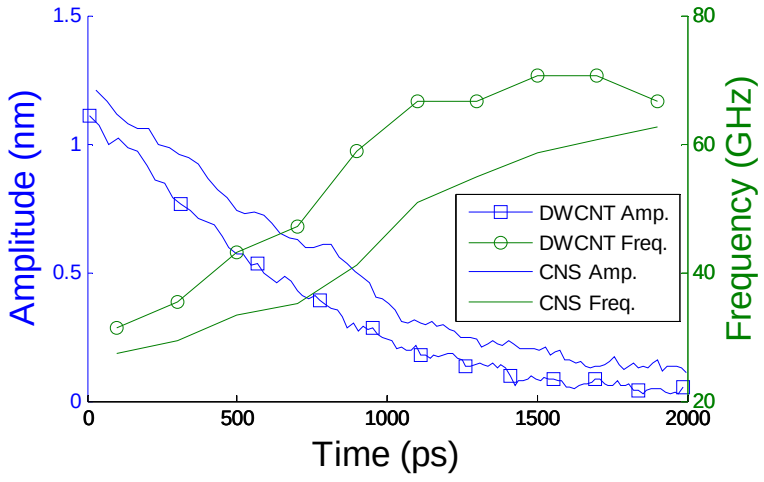

Figure 5.13. The comparison between the bridged-CNS-based nano-oscillator and the DWCNT-based nano-oscillator at 300K.

Besides the temperature, the commensuration between the oscillating CNT and the housing CNT or CNS also influences the oscillation performance. It has been shown

that the DWCNT-based oscillators with incommensurate inner and outer tubes have lower inter-tube friction force than the commensurate ones, leading to a much slower dissipation rate [117, 119]. To demonstrate the similar effect in bridged-CNS-based nano-oscillators, we replace the (10, 10) SWCNT that is housed inside and commensurate with the interlayer-bridged CNS with an incommensurate (15, 0) SWCNT (whose diameter is very close to (10, 10) SWCNT). Figure 5.14 reveals that the dissipation rate of the incommensurate bridged-CNS-based nano-oscillator (~0.237 nm/ns) is much slower than that of the commensurate one (~0.429 nm/ns). These results demonstrate an effective strategy to further enhance the performance of bridged-CNS-based nano-oscillators using an incommensurate oscillating SWCNT inside.

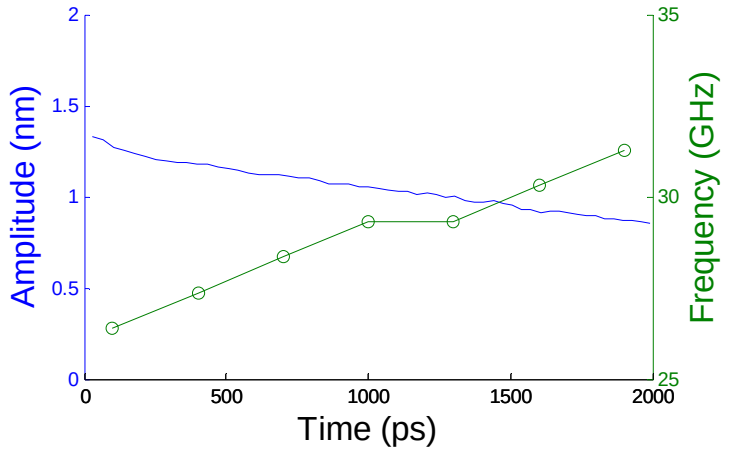

Figure 5.14. The peak oscillation amplitude of each cycle and the corresponding oscillation frequency as a function of time for a (15, 0) SWCNT inside the interlayer-bridged CNS, respectively. The simulations are carried out at 100K.

Our further studies show that the CNT-initiated scrolling of graphene is insensitive to the chirality of the CNT and the basal graphene. This further validates the feasibility

of such a strategy since the CNT and the basal graphene can be first synthesized and selected separately and then assembled. By contrast, synthesizing MWCNTs with controlled commensuration among constituent tubes still remains as a grand challenge, let alone leveraging such a strategy to improve the performance of MWCNT-based nano-oscillators.

5.2.5. Oscillation of the CNS/CNT nano-oscillator excited and driven by an external electric field

We further demonstrate that the bridged-CNS-based nano-oscillators can be excited and driven by an external electric field, a crucial feature to enable their potential application in ultrafast NEMS devices. For the MWCNT-based nano-oscillators, it has been proposed that, by inducing net charge [111] or electric dipole [109] into the inner tube, the carbon atoms in the charged/polarized inner tube are subjected to electrostatic capacitive force in an external electric field, which could be potentially used to initialize the oscillation. Controlled charging/polarization of the inner tube of a MWCNT require manipulation with sub-nanometer precision, thus remains rather challenging to achieve experimentally. However, such a strategy can become feasible for bridged-CNS-based nano-oscillators. For example, the SWCNT to be housed inside the interlayer-bridged CNS can be treated to possess net charges or dipoles before used to initiate the scrolling of the basal graphene that remains electrically neutral. Subject to an external AC electric field, the oscillation of the SWCNT housed inside the interlayer-bridged CNS can be initiated and driven by the alternating capacitive force.

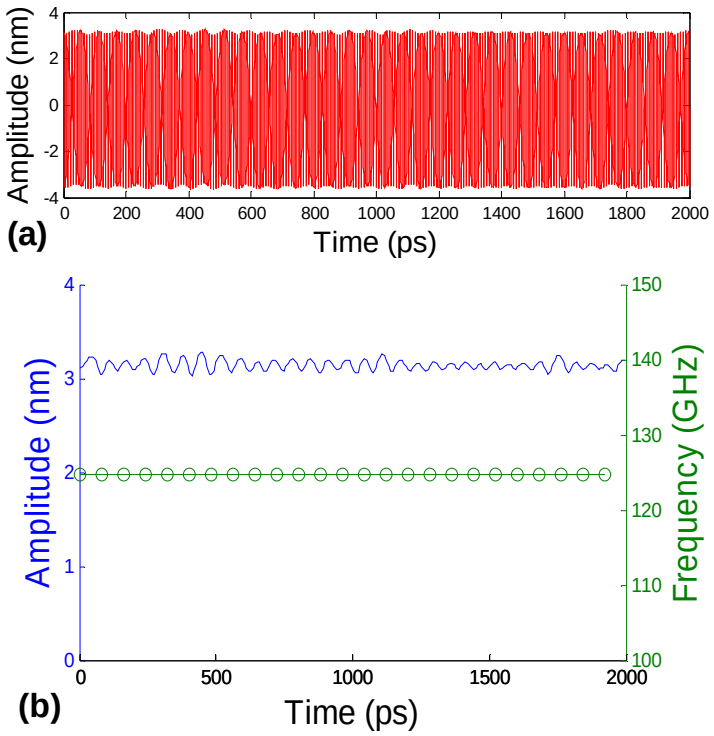

Figure 5.15. (a) The oscillation of the CNT in the interlayer-bridged CNS excited and driven by an external electrical field with an ac frequency of 125 GHz. (b) The peak oscillation amplitude of each cycle and the corresponding oscillation frequency as a function of time. The external ac electrical field can override the natural frequency of the CNS-based nano-oscillator. There is no appreciable decay of peak oscillation amplitude. The simulations are carried out at 100 K.

As a benchmark of such a strategy, Figure 5.15 shows the oscillation of the bridged-CNS-based nano-oscillator excited and then driven by a square-wave AC electric field with a frequency of 125 GHz. The amplitude of the resulting capacitive force acting on the SWCNT is 0.02 eV/Å per atom. Because such a driving force is much larger than the intensity of the intrinsic van der Waals restoring force between the atoms in the SWCNT and the CNS (~0.0004 eV/Å per atom), the oscillation driven by the external electric field can override the natural oscillation of the bridged-CNS-

based nano-oscillator. Figure 5.15b shows that the frequency of the resulting oscillation is identical to that of the external AC electric field. Furthermore, there is no appreciable decay in the oscillation amplitude, whose peak value in each oscillation cycle only fluctuates within 5%. In other words, the oscillation driven by the external electric field is highly sustainable.

Our further studies show that the resulting oscillation of the bridged-CNS-based nano-oscillator can be further fine tuned in a certain range under an external AC electric field of suitable frequency and magnitude. These explorations further demonstrate the potential to leverage CNS-based nano-oscillators to convert the electric energy of an external AC field into mechanical energy in the form of ultrafast oscillation. With proper treatment of the oscillating CNT, the above strategy can be potentially adapted to transduce and harvest electromagnetic and thermal energy into ultrafast mechanical oscillation [106, 120].

5.3. Summary

In summary, we demonstrate the CNT-initiated formation of a CNS from substrate-supported graphene, using MD simulations. The CNT is shown to help overcome the energy barrier to form an overlap in graphene. Once the overlap is formed, the graphene can spontaneously roll up into a CNS. The successful formation of a CNS depends on the CNT diameter, the C-C interaction strength and the graphene-substrate interaction strength. The phase diagram obtained from this study elucidates critical parameters governing the formation of CNSs from graphene. With the ever maturing fabrication of high quality CNTs and large area graphene on substrates, and

the nanopatterning technique to position these building blocks at high precision, the CNT-initiated formation of CNSs holds great potential leading to a feasible, all-dry, physical fabrication technique of high quality CNSs. The resulting CNS nanostructures hold potential to enable novel nanoscale electromechanical devices.

We then demonstrate a new type of ultrafast axial nano-oscillators based on the abovementioned CNS-CNT nanostrucures. The unique topological structure of the CNS-based nano-oscillator offers a viable pathway to fabricating ultrafast axial nano-oscillators, addressing a significant challenge that still remains for the previously proposed MWCNT-based axial nano-oscillator. We propose an effective and feasible strategy to reduce the oscillation dissipation of the CNS-based nano-oscillators by introducing interlayer bridging bonds in the CNS. The performance of the resulting bridged-CNS-based nano-oscillators is comparable or modestly better than the MWCNT-based ones. We further demonstrate the highly sustainable oscillation of the bridged-CNS-based nano-oscillators that can be excited and driven by an external AC electric field. With the ever maturing fabrication of high quality monolayer graphene and nanofabrication technique of patterning nanoscale building blocks, we envision a novel approach to harnessing and storing energy at nanoscale and over large area, enabled by distributing CNS-based nano-oscillators on an electronic surface.

Chapter 6: Summary and Future Work

6.1. Summary of Major Research Findings

The experimental discovery of graphene has inspired a surge of interest in developing its applications toward novel nanoelectronic devices due to its extraordinary electronic and mechanical properties. The atomically thin structure of graphene dictates the strong correlation between the electronic properties and the morphology of graphene. Therefore, the intrinsic or extrinsic random corrugations in graphene may result in unpredictable fluctuation of electronic properties that is undesirable for graphene-based nanodevice applications. This dissertation attempts to provide solutions to control the graphene morphology and thus its electronic properties via external regulation. It also demonstrates that the morphologic instability of graphene revealed from this research has fertile potential applications, such as characterizing the adhesion properties of graphene and fabricating carbon nanoscrolls. The main research findings of this dissertation are listed as follows:

Research Finding 1: The *extrinsic* morphology of graphene on a substrate surface is regulated, distinct from the random *intrinsic* morphology of freestanding graphene. The extrinsic morphology of the graphene regulated by the surface features of the underlying substrate results from the energy interplay among three types of energies: (1) graphene–substrate interaction energy, (2) graphene strain energy and (3) substrate strain energy. Via energy minimization, the substrate-regulated graphene morphology can be quantitatively determined.

Research Finding 2: Based on the energy interplay, computational models can be developed to quantitatively determine the equilibrium graphene morphology regulated by the substrates with various surface features, such as sinusoidal grooves, herringbone or checkerboard wrinkles. Depending on the substrate surface roughness and the graphene–substrate interfacial bonding energy, the equilibrium morphology of graphene ranges from (1) closely conforming to the substrate, to (2) remaining flat on the substrate.

Research Finding 3: The simulation results show that, in certain cases, the graphene morphology switches sharply between the abovementioned two distinct states. Such snap-through instability can be explained by the double-well shape of the total energy profile when the substrate surface roughness or the graphene-substrate interaction strength is near the threshold value.

Research Finding 4: The computational model developed for calculating substrate-regulated graphene morphology can be further extended to determine the graphene morphology regulated by nanowires patterned in parallel on substrate surface. Two cases are studied: (1) graphene regulated by widely spaced nanowires; (2) graphene regulated by densely spaced nanowires. The graphene morphology in these two cases can be regulated by the nanowire size, nanowire spacing, and interfacial bonding energy. The critical nanowire spacing and the critical interfacial bonding energy, where graphene switches between two representative morphologies, are determined.

Research Finding 5: The nanowire-regulated graphene morphology at atomistic resolution is obtained through molecular mechanics simulations. Two simulation

cases are considered: (1) a graphene nanoribbon intercalated by a Si nanowire on a SiO_2 substrate; (2) a blanket graphene flake intercalated by an array of Si nanowires evenly patterned in parallel on a SiO_2 substrate. The relationship between the graphene morphology and both geometric parameters and interfacial adhesion properties is revealed.

Research Finding 6: The morphology of few-layer graphene regulated by a compliant substrate with surface grooves can be explicitly determined by an analytic model. Few-layer graphene on compliant substrate exhibits two types of morphology: I) remaining bonded to the substrate; II) debonding from the substrate. The sharp transition between these two types of graphene morphology can be used to determine the adhesion between graphene and elastic materials, a crucial property that remains challenging to measure directly.

Research Finding 7: A carbon nanotube (CNT) can initiate the spontaneous rolling of substrate-supported graphene into a carbon nanotube (CNS). The successful fabrication is dependent on the CNT diameter, the C-C interaction strength and the graphene-substrate interaction strength. A phase diagram obtained from this study can serve as a guidance for controlling CNS formation by varying C-C interaction and selecting CNT size.

Research Finding 8: The nanostructure obtained from CNT initiated graphene scrolling is a CNS with a CNT housed inside. Because of the van der Waals restoring force between the CNT and the CNS, the single wall CNT can oscillate inside the CNS at a ultra-high frequency (a few tens to more than a hundred gigahertz). An

effective strategy is demonstrated to reduce the dissipation of the CNS-based nano-oscillator by introducing covalent bonds between the carbon layers in the CNS. Such a CNS-based nano-oscillator can be excited and driven by an external AC electric field.

6.2. Scientific Contributions

The scientific contributions of this dissertation are summarized in the following:

Contribution 1: A strategy to achieve precisely control of graphene morphology over large areas via extrinsic regulation (e.g., substrate surface features, patterned nanostructures on substrate) has been proposed. A general theoretical framework and computational models to determine the regulated graphene morphology have been formulated and benchmarked by a wide range of substrate features and nanoscale scaffolds.

Contribution 2: The snap-through instability in graphene morphology regulated by various types and dimensions of nanoscale extrinsic scaffolds has been revealed. The snap-through instability can potentially lead to desirable graphene electronic properties that could potentially enable new graphene-based functional electronic components (e.g. nano-switches). Furthermore, the snap-through instability of graphene morphology on compliant substrate sheds light on a feasible pathway to characterizing the graphene adhesion, a crucial property that remains challenging to measure directly due to the ultra-thin profile of graphene.

Contribution 3: An all-dry physical approach to fabricating carbon nanoscrolls

(CNSs) has been demonstrated. The results provided by this dissertation can serve as the guidance for high quality CNSs fabrication. A new type of ultra-fast nano-oscillators based on the resulting CNS/CNT nanostructure has been demonstrated, which could be potentially used for energy transduction, harnessing and storage at nanoscale.

6.3. Future research

Although this dissertation has attempted to address some critical issues in regulating graphene morphology and the related morphologic instability of graphene, the present research only reveals the tip of the iceberg of the fertile research field of graphene morphology and its applications. Following are some example issues on graphene morphology related to the present research which need to be further explored:

1. Graphene morphology on random rough substrate surface

This dissertation studies the morphology of graphene regulated by the patterned surface features on the substrate. In reality, it is more common that the substrate surfaces randomly fluctuate within a certain roughness range. These random fluctuations in substrate surface certainly will affect the morphology of graphene on top of the substrates. In order to precisely control graphene's electronic properties via strain engineering, the relationship between graphene morphology and the substrate random distributed roughness has to be investigated. Moreover, recent experiments show that the surface roughness as well as the friction of few-layer graphene increases as the number of graphene layers decreases. Because in graphene-reinforced nanocomposites, the interfacial friction between few-layer graphene and polymer

matrix plays a pivotal role in the mechanical failure of such nanocomposites, it is crucial to understand the effect of the substrate/matrix roughness and the number of graphene layers on the morphology and friction of few-layer graphene.

2. Morphological instability of graphene on compliant substrate under large deformation

The wrinkling of thin films on compliant substrate has been intensively investigated recently. The wrinkles come from the large compression in the thin film, induced by either the pre-stretching of the compliant substrate or the difference in the thermal expansion coefficients between thin film and substrate. Experiments have already observed the wrinkling in graphene on polymer substrate caused by the thermal mismatch. However, given the huge difference in mechanical properties between graphene and other thin film materials, the wrinkling modes of graphene could be quite different from that of thin films. It is uncertain that whether the buckling analysis of thin film based on elastic theory is still valid for graphene. Moreover, the length scale of graphene wrinkles observed in experiments ranges from hundreds of nanometers to several micrometers, which is much larger than the size of intrinsic ripples in graphene. Therefore, how to determine the wrinkle size in graphene and the effect of such wrinkling on the electronic properties of graphene becomes an important issue for the future realization of graphene based flexible electronics.

3. The deformation behaviors of carbon nanoscrolls

The deformation behaviors of CNTs have been studied comprehensively in the past two decades. For example, simulations and experiments have shown that CNTs are

susceptible to buckling under different loading conditions (compression, bending and torsion). The structure of CNSs looks similar to that of CNTs, but they are distinctly different. The unique spiral and topologically-open structure of CNSs may influence the deformation behavior of CNSs significantly. So far, no study has been done to investigate the deformation behaviors of CNSs, especially the buckling of CNSs. To address this question and further compare the bucking behaviors of CNSs with that of CNTs, atomistic simulations or theoretical modeling need to be carried out.

4. Applications of snap-through instability of the graphene morphology

The snap-through instability of graphene morphology on substrate with engineered surface features provides a new feature to enable graphene-based functional electronic components (e.g. nano-switches and nano-resonators). It is expected that when the dimensions of substrate surface features are close to the critical values where the snap-through instability occurs, a small external stimulus could lead to significant change of graphene morphology and thus alter the electronic properties of graphene. The external stimuli could be any subject that can either modify the interfacial adhesion between the graphene and the substrate, or vary the elastic properties of graphene. For example, the external stimuli could be electric fields, chemicals or gas molecules. However, further systematic studies, especially experimental studies, are desired to further demonstrate these novel device concepts based on the snap-through instability of graphene morphology.

References

[1] A. K. Geim and K. S. Novoselov, "The rise of graphene," *Nat Mater,* vol. 6, pp. 183-191, 2007.

[2] J. C. Meyer, A. K. Geim, M. I. Katsnelson, K. S. Novoselov, T. J. Booth, and S. Roth, "The structure of suspended graphene sheets," *Nature,* vol. 446, pp. 60-63, 2007.

[3] K. S. Novoselov, A. K. Geim, S. V. Morozov, D. Jiang, Y. Zhang, S. V. Dubonos, I. V. Grigorieva, and A. A. Firsov, "Electric Field Effect in Atomically Thin Carbon Films," *Science,* vol. 306, pp. 666-669, 2004.

[4] Y. B. Zhang, Y. W. Tan, H. L. Stormer, and P. Kim, "Experimental observation of the quantum Hall effect and Berry's phase in graphene," *Nature,* vol. 438, pp. 201-204, Nov 2005.

[5] http://nobelprize.org/nobel_prizes/physics/laureates/2010.

[6] A. K. Geim and P. Kim, "Carbon wonderland," *Scientific American,* vol. 298, pp. 90-97, Apr 2008.

[7] X. S. Li, W. W. Cai, J. H. An, S. Kim, J. Nah, D. X. Yang, R. Piner, A. Velamakanni, I. Jung, E. Tutuc, S. K. Banerjee, L. Colombo, and R. S. Ruoff, "Large-Area Synthesis of High-Quality and Uniform Graphene Films on Copper Foils," *Science,* vol. 324, pp. 1312-1314, 2009.

[8] P. W. Sutter, J. I. Flege, and E. A. Sutter, "Epitaxial graphene on ruthenium," *Nature Materials,* vol. 7, pp. 406-411, May 2008.

[9] K. S. Kim, Y. Zhao, H. Jang, S. Y. Lee, J. M. Kim, K. S. Kim, J.-H. Ahn, P. Kim, J.-Y. Choi, and B. H. Hong, "Large-scale pattern growth of graphene films for stretchable transparent electrodes," *Nature,* vol. 457, pp. 706-710, 2009.

[10] A. Reina, X. T. Jia, J. Ho, D. Nezich, H. B. Son, V. Bulovic, M. S. Dresselhaus, and J. Kong, "Large Area, Few-Layer Graphene Films on Arbitrary Substrates by Chemical Vapor Deposition," *Nano Letters,* vol. 9, pp. 30-35, Jan 2009.

[11] G. Eda, G. Fanchini, and M. Chhowalla, "Large-area ultrathin films of reduced graphene oxide as a transparent and flexible electronic material," *Nat Nano,* vol. 3, pp. 270-274, 2008.

[12] C. Berger, Z. M. Song, X. B. Li, X. S. Wu, N. Brown, C. Naud, D. Mayou, T. B. Li, J. Hass, A. N. Marchenkov, E. H. Conrad, P. N. First, and W. A. de

Heer, "Electronic confinement and coherence in patterned epitaxial graphene," *Science,* vol. 312, pp. 1191-1196, 2006.

[13] S. Bae, H. Kim, Y. Lee, X. F. Xu, J. S. Park, Y. Zheng, J. Balakrishnan, T. Lei, H. R. Kim, Y. I. Song, Y. J. Kim, K. S. Kim, B. Ozyilmaz, J. H. Ahn, B. H. Hong, and S. Iijima, "Roll-to-roll production of 30-inch graphene films for transparent electrodes," *Nature Nanotechnology,* vol. 5, pp. 574-578, Aug 2010.

[14] M. Y. Han, B. Ozyilmaz, Y. B. Zhang, and P. Kim, "Energy band-gap engineering of graphene nanoribbons," *Physical Review Letters,* vol. 98, 2007.

[15] Y. B. Zhang, T. T. Tang, C. Girit, Z. Hao, M. C. Martin, A. Zettl, M. F. Crommie, Y. R. Shen, and F. Wang, "Direct observation of a widely tunable bandgap in bilayer graphene," *Nature,* vol. 459, pp. 820-823, 2009.

[16] Z. H. Ni, T. Yu, Y. H. Lu, Y. Y. Wang, Y. P. Feng, and Z. X. Shen, "Uniaxial Strain on Graphene: Raman Spectroscopy Study and Band-Gap Opening," *Acs Nano,* vol. 2, pp. 2301-2305, 2008.

[17] K. S. Novoselov, A. K. Geim, S. V. Morozov, D. Jiang, M. I. Katsnelson, I. V. Grigorieva, S. V. Dubonos, and A. A. Firsov, "Two-dimensional gas of massless Dirac fermions in graphene," *Nature,* vol. 438, pp. 197-200, 2005.

[18] S. V. Morozov, K. S. Novoselov, F. Schedin, D. Jiang, A. A. Firsov, and A. K. Geim, "Two-dimensional electron and hole gases at the surface of graphite," *Physical Review B,* vol. 72, 2005.

[19] J. H. Chen, C. Jang, S. D. Xiao, M. Ishigami, and M. S. Fuhrer, "Intrinsic and extrinsic performance limits of graphene devices on SiO2," *Nature Nanotechnology,* vol. 3, pp. 206-209, 2008.

[20] R. R. Nair, P. Blake, A. N. Grigorenko, K. S. Novoselov, T. J. Booth, T. Stauber, N. M. R. Peres, and A. K. Geim, "Fine structure constant defines visual transparency of graphene," *Science,* vol. 320, pp. 1308-1308, 2008.

[21] I. Jung, M. Pelton, R. Piner, D. A. Dikin, S. Stankovich, S. Watcharotone, M. Hausner, and R. S. Ruoff, "Simple approach for high-contrast optical imaging and characterization of graphene-based sheets," *Nano Letters,* vol. 7, pp. 3569-3575, 2007.

[22] W. Z. Bao, F. Miao, Z. Chen, H. Zhang, W. Y. Jang, C. Dames, and C. N. Lau, "Controlled ripple texturing of suspended graphene and ultrathin graphite membranes," *Nature Nanotechnology,* vol. 4, pp. 562-566, 2009.

[23] C. Lee, X. Wei, J. W. Kysar, and J. Hone, "Measurement of the Elastic Properties and Intrinsic Strength of Monolayer Graphene," *Science,* vol. 321, pp. 385-388, 2008.

[24] Q. Lu, and R. Huang, "Effect of edge structures on elastic modulus and fracture of graphene nanoribbons under uniaxial tension," *rXiv:1007.3298v1*

[25] R. Murali, K. Brenner, Y. X. Yang, T. Beck, and J. D. Meindl, "Resistivity of Graphene Nanoribbon Interconnects," *Ieee Electron Device Letters*, vol. 30, pp. 611-613, 2009.

[26] Y. W. Son, M. L. Cohen, and S. G. Louie, "Half-metallic graphene nanoribbons," *Nature*, vol. 444, pp. 347-349, 2006.

[27] Y. W. Son, M. L. Cohen, and S. G. Louie, "Energy gaps in graphene nanoribbons," *Physical Review Letters*, vol. 97, 2006.

[28] Q. M. Yan, B. Huang, J. Yu, F. W. Zheng, J. Zang, J. Wu, B. L. Gu, F. Liu, and W. H. Duan, "Intrinsic current-voltage characteristics of graphene nanoribbon transistors and effect of edge doping," *Nano Letters*, vol. 7, pp. 1469-1473, 2007.

[29] G. C. Liang, N. Neophytou, M. S. Lundstrom, and D. E. Nikonov, "Contact effects in graphene nanoribbon transistors," *Nano Letters*, vol. 8, pp. 1819-1824, 2008.

[30] L. A. Ponomarenko, F. Schedin, M. I. Katsnelson, R. Yang, E. W. Hill, K. S. Novoselov, and A. K. Geim, "Chaotic dirac billiard in graphene quantum dots," *Science*, vol. 320, pp. 356-358, 2008.

[31] P. Blake, P. D. Brimicombe, R. R. Nair, T. J. Booth, D. Jiang, F. Schedin, L. A. Ponomarenko, S. V. Morozov, H. F. Gleeson, E. W. Hill, A. K. Geim, and K. S. Novoselov, "Graphene-based liquid crystal device," *Nano Letters*, vol. 8, pp. 1704-1708, 2008.

[32] Y. Wang, X. H. Chen, Y. L. Zhong, F. R. Zhu, and K. P. Loh, "Large area, continuous, few-layered graphene as anodes in organic photovoltaic devices," *Applied Physics Letters*, vol. 95, 2009.

[33] L. G. De Arco, Y. Zhang, C. W. Schlenker, K. Ryu, M. E. Thompson, and C. W. Zhou, "Continuous, Highly Flexible, and Transparent Graphene Films by Chemical Vapor Deposition for Organic Photovoltaics," *Acs Nano*, vol. 4, pp. 2865-2873, 2010.

[34] J. B. Wu, M. Agrawal, H. A. Becerril, Z. N. Bao, Z. F. Liu, Y. S. Chen, and P. Peumans, "Organic Light-Emitting Diodes on Solution-Processed Graphene Transparent Electrodes," *Acs Nano*, vol. 4, pp. 43-48, 2010.

[35] S. Stankovich, D. A. Dikin, G. H. B. Dommett, K. M. Kohlhaas, E. J. Zimney, E. A. Stach, R. D. Piner, S. T. Nguyen, and R. S. Ruoff, "Graphene-based composite materials," *Nature*, vol. 442, pp. 282-286, 2006.

[36] F. Schedin, A. K. Geim, S. V. Morozov, E. W. Hill, P. Blake, M. I. Katsnelson, and K. S. Novoselov, "Detection of individual gas molecules adsorbed on graphene," *Nat Mater,* vol. 6, pp. 652-655, 2007.

[37] M. D. Stoller, S. Park, Y. Zhu, J. An, and R. S. Ruoff, "Graphene-Based Ultracapacitors," *Nano Letters,* vol. 8, pp. 3498-3502, 2008.

[38] S. Patchkovskii, J. S. Tse, S. N. Yurchenko, L. Zhechkov, T. Heine, and G. Seifert, "Graphene nanostructures as tunable storage media for molecular hydrogen," *Proceedings of the National Academy of Sciences of the United States of America,* vol. 102, pp. 10439-10444, 2005.

[39] A. Fasolino, J. H. Los, and M. I. Katsnelson, "Intrinsic ripples in graphene," *Nat Mater,* vol. 6, pp. 858-861, 2007.

[40] V. B. Shenoy, C. D. Reddy, A. Ramasubramaniam, and Y. W. Zhang, "Edge-Stress-Induced Warping of Graphene Sheets and Nanoribbons," *Physical Review Letters,* vol. 101, pp. 245501-4, 2008.

[41] Q. Lu and R. Huang, "Excess energy and deformation along free edges of graphene nanoribbons," *Physical Review B,* vol. 81, 2010.

[42] Z. P. Xu and M. J. Buehler, "Geometry Controls Conformation of Graphene Sheets: Membranes, Ribbons, and Scrolls," *Acs Nano,* vol. 4, pp. 3869-3876, 2010.

[43] M. Ishigami, J. H. Chen, W. G. Cullen, M. S. Fuhrer, and E. D. Williams, "Atomic structure of graphene on SiO2," *Nano letters,* vol. 7, pp. 1643-1648, 2007.

[44] W. G. Cullen, M. Yamamoto, K. M. Burson, J. H. Chen, C. Jang, L. Li, M. S. Fuhrer, and E. D. Williams, "High-Fidelity Conformation of Graphene to SiO2 Topographic Features," *Physical Review Letters,* vol. 105, Nov 2010.

[45] E. Stolyarova, K. T. Rim, S. Ryu, J. Maultzsch, P. Kim, L. E. Brus, T. F. Heinz, M. S. Hybertsen, and G. W. Flynn, "High-resolution scanning tunneling microscopy imaging of mesoscopic graphene sheets on an insulating surface," *Proc Natl Acad Sci U S A,* vol. 104, pp. 9209-9212, 2007.

[46] U. Stoberl, U. Wurstbauer, W. Wegscheider, D. Weiss, and J. Eroms, "Morphology and flexibility of graphene and few-layer graphene on various substrates," *Applied Physics Letters,* vol. 93, p. 051906, Aug 2008.

[47] F. V. Tikhonenko, D. W. Horsell, R. V. Gorbachev, and A. K. Savchenko, "Weak localization in graphene flakes," *Physical Review Letters,* vol. 100, Feb 2008.

[48] V. Geringer, M. Liebmann, T. Echtermeyer, S. Runte, M. Schmidt, R. Ruckamp, M. C. Lemme, and M. Morgenstern, "Intrinsic and extrinsic corrugation of monolayer graphene deposited on SiO2," *Physical Review Letters,* vol. 102, p. 4, Feb 2009.

[49] C. Lui, L. Liu, K. Mak, G. Flynn, and T. Heinz, "Ultraflat graphene," *Nature,* vol. 462, pp. 339-341, 2009.

[50] A. L. V. de Parga, F. Calleja, B. Borca, J. M. C. G. Passeggi, J. J. Hinarejos, F. Guinea, and R. Miranda, "Periodically Rippled Graphene: Growth and Spatially Resolved Electronic Structure," *Physical Review Letters,* vol. 100, pp. 056807-4, 2008.

[51] I. Pletikosic, M. Kralj, P. Pervan, R. Brako, J. Coraux, A. T. N'Diaye, C. Busse, and T. Michely, "Dirac Cones and Minigaps for Graphene on Ir(111)," *Physical Review Letters,* vol. 102, 2009.

[52] A. B. Preobrajenski, M. L. Ng, A. S. Vinogradov, and N. Martensson, "Controlling graphene corrugation on lattice-mismatched substrates," *Physical Review B,* vol. 78, 2008.

[53] Z. J. Li, Z. G. Cheng, R. Wang, Q. Li, and Y. Fang, "Spontaneous Formation of Nanostructures in Graphene," *Nano Letters,* vol. 9, pp. 3599-3602, 2009.

[54] R. Bacon, "GROWTH, STRUCTURE, AND PROPERTIES OF GRAPHITE WHISKERS," *Journal of Applied Physics,* vol. 31, pp. 283-290, 1960.

[55] L. M. Viculis, J. J. Mack, and R. B. Kaner, "A chemical route to carbon nanoscrolls," *Science,* vol. 299, pp. 1361-1361, 2003.

[56] S. F. Braga, V. R. Coluci, S. B. Legoas, R. Giro, D. S. Galvao, and R. H. Baughman, "Structure and Dynamics of Carbon Nanoscrolls," *Nano Letters,* vol. 4, pp. 881-884, 2004.

[57] X. H. Shi, N. M. Pugno, and H. J. Gao, "Tunable Core Size of Carbon Nanoscrolls," *Journal of Computational and Theoretical Nanoscience,* vol. 7, pp. 517-521, 2010.

[58] V. R. Coluci, S. F. Braga, R. H. Baughman, and D. S. Galvao, "Prediction of the hydrogen storage capacity of carbon nanoscrolls," *Physical Review B,* vol. 75, 2007.

[59] G. Mpourmpakis, E. Tylianakis, and G. E. Froudakis, "Carbon Nanoscrolls: A Promising Material for Hydrogen Storage," *Nano Letters,* vol. 7, pp. 1893-1897, 2007.

[60] X. Shi, N. M. Pugno, Y. Cheng, and H. Gao, "Gigahertz breathing oscillators based on carbon nanoscrolls," *Applied Physics Letters,* vol. 95, pp. 163113-3, 2009.

[61] X. H. Shi, Y. Cheng, N. M. Pugno, and H. J. Gao, "Tunable Water Channels with Carbon Nanoscrolls," *Small,* vol. 6, pp. 739-744, 2010.

[62] X. Xie, L. Ju, X. Feng, Y. Sun, R. Zhou, K. Liu, S. Fan, Q. Li, and K. Jiang, "Controlled Fabrication of High-Quality Carbon Nanoscrolls from Monolayer Graphene," *Nano Letters,* vol. 9, pp. 2565-2570, 2009.

[63] N. Patra, B. Wang, and P. Král, "Nanodroplet Activated and Guided Folding of Graphene Nanostructures," *Nano Letters,* vol. 9, pp. 3766-3771, 2009.

[64] B. V. C. Martins and D. S. Galvao, "Curved graphene nanoribbons: structure and dynamics of carbon nanobelts," *Nanotechnology,* vol. 21, 2010.

[65] S. V. Morozov, K. S. Novoselov, M. I. Katsnelson, F. Schedin, L. A. Ponomarenko, D. Jiang, and A. K. Geim, "Strong Suppression of Weak Localization in Graphene," *Physical Review Letters,* vol. 97, pp. 016801-4, 2006.

[66] A. H. C. Neto, F. Guinea, N. M. R. Peres, K. S. Novoselov, and A. K. Geim, "The electronic properties of graphene," *Reviews of Modern Physics,* vol. 81, pp. 109-54, 2009.

[67] U. Stoberl, U. Wurstbauer, W. Wegscheider, D. Weiss, and J. Eroms, "Morphology and flexibility of graphene and few-layer graphene on various substrates," *Applied Physics Letters,* vol. 93, pp. 051906-3, 2008.

[68] Y. Xia, J. A. Rogers, K. E. Paul, and G. M. Whitesides, "Unconventional Methods for Fabricating and Patterning Nanostructures," *Chemical Reviews,* vol. 99, pp. 1823-1848, 1999.

[69] S. Y. Chou, P. R. Krauss, and P. J. Renstrom, "Imprint Lithography with 25-Nanometer Resolution," *Science,* vol. 272, pp. 85-87, April 5, 1996 1996.

[70] W. M. Choi, J. Song, D.-Y. Khang, H. Jiang, Y. Y. Huang, and J. A. Rogers, "Biaxially Stretchable ¡°Wavy¡± Silicon Nanomembranes," *Nano Letters,* vol. 7, pp. 1655-1663, 2007.

[71] X. Chen and J. W. Hutchinson, "Herringbone Buckling Patterns of Compressed Thin Films on Compliant Substrates," *Journal of Applied Mechanics,* vol. 71, pp. 597-603, 2004.

[72] D. D. D. Ma, C. S. Lee, F. C. K. Au, S. Y. Tong, and S. T. Lee, "Small-diameter silicon nanowire surfaces," *Science,* vol. 299, pp. 1874-1877, 2003.

[73] N. A. Melosh, A. Boukai, F. Diana, B. Gerardot, A. Badolato, P. M. Petroff, and J. R. Heath, "Ultrahigh-density nanowire lattices and circuits," *Science*, vol. 300, pp. 112-115, 2003.

[74] C. T. Black, "Self-aligned self assembly of multi-nanowire silicon field effect transistors," *Applied Physics Letters*, vol. 87, 2005.

[75] T. Tsukamoto and T. Ogino, "Morphology of Graphene on Step-Controlled Sapphire Surfaces," *Applied Physics Express*, vol. 2, 2009.

[76] C. H. Lui, L. Liu, K. F. Mak, G. W. Flynn, and T. F. Heinz, "Ultraflat graphene," *Nature*, vol. 462, pp. 339-341, 2009.

[77] J. H. Chen, M. Ishigami, C. Jang, D. R. Hines, M. S. Fuhrer, and E. D. Williams, "Printed graphene circuits," *Advanced Materials*, vol. 19, pp. 3623-+, 2007.

[78] S. Scharfenberg, D. Z. Rocklin, C. Chialvo, R. L. Weaver, P. M. Goldbart, and N. Mason, "Probing the mechanical properties of graphene using a corrugated elastic substrate," *Applied Physics Letters*, vol. 98, 2011.

[79] L. Y. Jiang, Y. Huang, H. Jiang, G. Ravichandran, H. Gao, K. C. Hwang, and B. Liu, "A cohesive law for carbon nanotube/polymer interfaces based on the van der Waals force," *Journal of the Mechanics and Physics of Solids*, vol. 54, pp. 2436-2452, 2006.

[80] W. B. Lu, J. Wu, J. Song, K. C. Hwang, L. Y. Jiang, and Y. Huang, "A cohesive law for interfaces between multi-wall carbon nanotubes and polymers due to the van der Waals interactions," *Computer Methods in Applied Mechanics and Engineering*, vol. 197, pp. 3261-3267, 2008.

[81] P. J. Feibelman, "Pinning of graphene to Ir(111) by flat Ir dots," *Physical Review B (Condensed Matter and Materials Physics)*, vol. 77, pp. 165419-7, 2008.

[82] D. Toma´nek, W. Zhong, and E. Krastev, "Stability of multishell fullerenes," *Physical Review B*, vol. 48, p. 15461, 1993.

[83] S. J. V. Frankland, V. M. Harik, G. M. Odegard, D. W. Brenner, and T. S. Gates, "The stress-strain behavior of polymer-nanotube composites from molecular dynamics simulation," *Composites Science and Technology*, vol. 63, pp. 1655-1661, 2003.

[84] D. Roy, M. Chhowalla, H. Wang, N. Sano, I. Alexandrou, T. W. Clyne, and G. A. J. Amaratunga, "Characterisation of carbon nano-onions using Raman spectroscopy," *Chemical Physics Letters*, vol. 373, pp. 52-56, 2003.

[85] J. N. Israelachvili, " Intermolecular and Surface Forces," 2nd ed., Academic London, San Diego, 1991.

[86] B. D. Gates, Q. Xu, M. Stewart, D. Ryan, C. G. Willson, and G. M. Whitesides, "New Approaches to Nanofabrication: Molding, Printing, and Other Techniques," *Chemical Reviews,* vol. 105, pp. 1171-1196, 2005.

[87] M. C. McAlpine, R. S. Friedman, and C. M. Lieber, "Nanoimprint Lithography for Hybrid Plastic Electronics," *Nano Letters,* vol. 3, pp. 443-445, 2003.

[88] N. Li, W. Wu, and S. Y. Chou, "Sub-20-nm Alignment in Nanoimprint Lithography Using Moiré Fringe," *Nano Letters,* vol. 6, pp. 2626-2629, 2006.

[89] J. Sabio, C. Seoanez, S. Fratini, F. Guinea, A. H. C. Neto, and F. Sols, "Electrostatic interactions between graphene layers and their environment," *Physical Review B (Condensed Matter and Materials Physics),* vol. 77, pp. 195409-8, 2008.

[90] O. Pierre-Louis, "Adhesion of membranes and filaments on rippled surfaces," *Physical Review E,* vol. 78, 2008.

[91] Y. Kondo and K. Takayanagi, "Synthesis and characterization of helical multi-shell gold nanowires," *Science,* vol. 289, pp. 606-608, 2000.

[92] D. W. Brenner, O. A. Shenderova, J. A. Harrison, S. J. Stuart, B. Ni, and S. B. Sinnott, "A second-generation reactive empirical bond order (REBO) potential energy expression for hydrocarbons," *Journal of Physics: Condensed Matter,* vol. 14, pp. 783-802, 2002.

[93] V. A. Bakaev, W. A. Steele, T. I. Bakaeva, and C. G. Pantano, "Adsorption of CO[sub 2] and Ar on glass surfaces. Computer simulation and experimental study," *The Journal of Chemical Physics,* vol. 111, pp. 9813-9821, 1999.

[94] D. C. Liu and J. Nocedal, "On the limited memory BFGS method for large scale optimization," *Mathematical Programming,* vol. 45, pp. 503-528, 1989.

[95] X. Liang, Z. Fu, and S. Y. Chou, "Graphene transistors fabricated via transfer-printing in device active-areas on large wafer," *Nano Letters,* vol. 7, pp. 3840-3844, 2007.

[96] R. Huang, "Kinetic wrinkling of an elastic film on a viscoelastic substrate," *Journal of the Mechanics and Physics of Solids,* vol. 53, pp. 63-89, 2005.

[97] Z. Y. Huang, W. Hong, and Z. Suo, "Nonlinear analyses of wrinkles in a film bonded to a compliant substrate," *Journal of the Mechanics and Physics of Solids,* vol. 53, pp. 2101-2118, 2005.

[98] S. Cranford, D. Sen, and M. J. Buehler, "Meso-origami: Folding multilayer graphene sheets," *Applied Physics Letters,* vol. 95, 2009.

[99] Z. H. Aitken and R. Huang, "Effects of mismatch strain and substrate surface corrugation on morphology of supported monolayer graphene," *Journal of Applied Physics,* vol. 107, pp. 123531-10, 2010.

[100] S. J. Stuart, A. B. Tutein, and J. A. Harrison, "A reactive potential for hydrocarbons with intermolecular interactions," *The Journal of Chemical Physics,* vol. 112, pp. 6472-6486, 2000.

[101] X. Shi, Y. Cheng, N. M. Pugno, and H. Gao, "A translational nanoactuator based on carbon nanoscrolls on substrates," *Applied Physics Letters,* vol. 96, pp. 517-521, 2010.

[102] R. Langlet, M. Devel, and P. Lambin, "Computation of the static polarizabilities of multi-wall carbon nanotubes and fullerites using a Gaussian regularized point dipole interaction model," *Carbon,* vol. 44, pp. 2883-2895, 2006.

[103] S. Plimpton, "Fast Parallel Algorithms for Short-Range Molecular Dynamics," *Journal of Computational Physics,* vol. 117, pp. 1-19, 1995.

[104] J. Cumings and A. Zettl, "Low-friction nanoscale linear bearing realized from multiwall carbon nanotubes," *Science,* vol. 289, pp. 602-604, 2000.

[105] Q. S. Zheng and Q. Jiang, "Multiwalled carbon nanotubes as gigahertz oscillators," *Physical Review Letters,* vol. 88, 2002.

[106] S. B. Legoas, V. R. Coluci, S. F. Braga, P. Z. Coura, S. O. Dantas, and D. S. Galvao, "Molecular-dynamics simulations of carbon nanotubes as gigahertz oscillators," *Physical Review Letters,* vol. 90, 2003.

[107] J. L. Rivera, C. McCabe, and P. T. Cummings, "Oscillatory behavior of double-walled nanotubes under extension: A simple nanoscale damped spring," *Nano Letters,* vol. 3, pp. 1001-1005, 2003.

[108] Y. Zhao, C. C. Ma, G. H. Chen, and Q. Jiang, "Energy dissipation mechanisms in carbon nanotube oscillators," *Physical Review Letters,* vol. 91, 2003.

[109] O. V. Ershova, Y. E. Lozovik, A. M. Popov, O. N. Bubel, N. A. Poklonskii, and E. F. Kislyakov, "Control of the motion of nanoelectromechanical systems based on carbon nanotubes," *Physics of the Solid State,* vol. 49, pp. 2010-2014, 2007.

[110] V. R. Coluci, V. S. Timoteo, and D. S. Galvao, "Thermophoretically driven carbon nanotube oscillators," *Applied Physics Letters,* vol. 95, Dec 2009.

[111] J. W. Kang, K. O. Song, H. J. Hwang, and Q. Jiang, "Nanotube oscillator based on a short single-walled carbon nanotube bundle," *Nanotechnology,* vol. 17, pp. 2250-2258, 2006.

[112] Y. K. Kim and D. H. Min, "Preparation of scrolled graphene oxides with multi-walled carbon nanotube templates," *Carbon,* vol. 48, pp. 4283-4288, 2010.

[113] V. R. Coluci, S. B. Legoas, M. A. M. de Aguiar, and D. S. Galvao, "Chaotic signature in the motion of coupled carbon nanotube oscillators," *Nanotechnology,* vol. 16, pp. 583-589, 2005.

[114] A. V. Krasheninnikov and F. Banhart, "Engineering of nanostructured carbon materials with electron or ion beams," *Nature Materials,* vol. 6, pp. 723-733, 2007.

[115] A. Kis, G. Csanyi, J. P. Salvetat, T. N. Lee, E. Couteau, A. J. Kulik, W. Benoit, J. Brugger, and L. Forro, "Reinforcement of single-walled carbon nanotube bundles by intertube bridging," *Nature Materials,* vol. 3, pp. 153-157, 2004.

[116] A. J. R. da Silva, A. Fazzio, and A. Antonelli, "Bundling up carbon nanotubes through Wigner defects," *Nano Letters,* vol. 5, pp. 1045-1049, 2005.

[117] W. L. Guo, Y. F. Guo, H. J. Gao, Q. S. Zheng, and W. Y. Zhong, "Energy dissipation in gigahertz oscillators from multiwalled carbon nanotubes," *Physical Review Letters,* vol. 91, 2003.

[118] Z. P. Xu, "Energy dissipation in the double-walled carbon nanotube based mechanical oscillators," *Journal of Computational and Theoretical Nanoscience,* vol. 5, pp. 655-658, 2008.

[119] X. G. Zhao and P. T. Cummings, "Molecular dynamics study of carbon nanotube oscillators revisited," *Journal of Chemical Physics,* vol. 124, 2006.

[120] J. W. Kang, K. O. Song, O. K. Kwon, and H. J. Hwang, "Carbon nanotube oscillator operated by thermal expansion of encapsulated gases," *Nanotechnology,* vol. 16, pp. 2670-2676, 2005.

Publications

Journal Publications

1. **Z. Zhang** and T. Li, "The buckling behavior of carbon nanoscrolls", in preparation (2011).
2. **Z. Zhang** and T. Li, "Determining graphene adhesion via substrate-regulated morphology of graphene", *Journal of Applied Physics*, 110, 083526 (2011).
3. **Z. Zhang** and T. Li, "Ultrafast nano-oscillators based on interlayer-bridged carbon nanoscrolls", *Nanoscale Research Letters*, 6, 470 (2011).
4. T. Li, **Z. Zhang**, B. Michaux, "Competing failure mechanisms of thin metal films on polymer substrates under tension", invited paper, *Theoretical and Applied Mechanics Letters*, 1, 041002 (2011).
5. E. Dechaumphai, **Z. Zhang**, N. P. Siwak, R. Ghodssi and T. Li, "Resonant frequency of gold/polycarbonate hybrid nano resonators fabricated on plastics via nano-transfer printing", *Nanoscale Research Letters*, 6, 90 (2011).
6. **Z. Zhang** and T. Li, "A molecular mechanics study of morphologic interaction between graphene and Si nanowires on a SiO_2 substrate", *Journal of Nanomaterials*, 2011, 374018 (2011).
7. **Z. Zhang** and T. Li, "Carbon nanotube initiated formation of carbon nanoscrolls", *Applied Physics Letters*, 97, 081909 (2010). Also highlighted in the Sept. 6, 2010 issue of the *Virtual Journal of Nanoscale Science and Technology*.
8. **Z. Zhang** and T. Li, "Graphene morphology regulated by nanowires patterned in parallel on a substrate surface", *Journal of Applied Physics*, 107, 103519 (2010). Also highlighted in the Jun. 7, 2010 issue of the *Virtual Journal of Nanoscale Science and Technology*.
9. T. Li and **Z. Zhang**, "Substrate-regulated morphology of graphene", *Journal of Physics D: Applied Physics*, 43, 075303 (2010).
10. T. Li and **Z. Zhang**, "Snap-through instability of graphene on substrates",

Nanoscale Research Letters, 5, 169-173 (2010).

11. **Z. Zhang** and T. Li, "Effects of grain boundary adhesion and grain size on ductility of thin metal films on polymer substrates", *Scripta Materialia*, 59, 862-865 (2008).

Conference Presentations

1. **Z. Zhang** and T. Li, "The buckling behavior of carbon nanoscrolls", *International Conference on Nanoscience and Technology, China 2011 (ChinaNANO 2011)*, Beijing, China (2011).
2. **Z. Zhang** and T. Li, "The deformation behavior of carbon nanoscrolls", *ASME Applied Mechanics and Materials Conference (McMAT2011)*, Chicago, IL (2011).
3. **Z. Zhang** and T. Li, "Carbon nanotube initiated formation of carbon nanoscrolls", *NSF Division of Civil, Mechanical and Manufacturing Innovation Conference 2011*, Atlanta, GA (2011).
4. **Z. Zhang** and T. Li, "Carbon nanotube initiated formation of carbon nanoscrolls", *2010 MRS Fall Meeting*, Boston, MA (2010).
5. **Z. Zhang** and T. Li, "Carbon nanotube initiated formation of carbon nanoscrolls", *2010 ASME International Mechanical Engineering Congress*, Vancouver, BC Canada (2010).
6. **Z. Zhang** and T. Li, "A molecular mechanics study of morphologic interaction between graphene and Si nanowires on a SiO_2 substrate", *2010 ASME International Mechanical Engineering Congress*, Vancouver, BC Canada (2010).
7. **Z. Zhang** and T. Li, "Graphene morphology regulated by nanowires patterned on a substrate surface", *the 16th US National Congress of Theoretical and Applied Mechanics*, State College, PA (2010).
8. **Z. Zhang**, B. Michaux and T. Li, "Origins of large variation in ductility of thin nanocrystalline metallizations on polymer substrates", *the 16th US National Congress of Theoretical and Applied Mechanics*, State College, PA (2010).

9. **Z. Zhang** and T. Li, “A molecular mechanics study of graphene/nanowires interaction”, *Graphene Week 2010: an International Conference on Graphene Science*, College Park, MD (2010).
10. T. Li and **Z. Zhang**, “Graphene morphology modulated by nanowires patterned on a substrate surface”, *International Semiconductor Device Research Symposium*, College Park, MD (2009).
11. **Z. Zhang** and T. Li, “Snap-through instability of graphene morphology on substrates”, *2009 ASME International Mechanical Engineering Congress & Exposition*, Lake Buena Vista, FL (2009).